

Search for Supersymmetry in events with jets and missing energy at the LHC



Chris Lucas

School of Physics
University of Bristol

This dissertation is submitted for the degree of

Doctor of Philosophy

2015

DECLARATION

I, Chris Lucas, declare that the work in this dissertation was carried out in accordance with the requirements of the University's Regulations and Code of Practice for Research Degree Programmes and that it has not been submitted for any other academic award. Except where indicated by specific reference in the text, the work is the candidate's own work, or where the candidate has been the major contributor. This work has been carried out within the context of the University of Bristol CMS group and the CMS SUSY working group, itself a part of the CMS collaboration. Any views expressed in the dissertation are those of the author.

Signed: _____

Date: _____

ACKNOWLEDGEMENTS

As I sit here in my kitchen, after having read my thesis for what feels like the thousandth time, I'm left with the intimidating task of writing these final words - intimidating because there is no possible way that I can portray enough my incredible gratitude to the countless number of people that have helped me get to the point I find myself in today. But let's give it a shot anyway.

Firstly, I would like to thank the many people I have had the pleasure of working with over the past three and half years. In particular those in the RA1 team, notably Darren Burton, Yossof Eshaq, Edward Laird, Bryn Mathias and Zhaoxia Meng, each for the seemingly unending patience and help they've shown me throughout my work, especially in my early days. Of course, it is to Rob Bainbridge that I owe an incredible deal - not only for his constant guidance and supervision throughout our work together, but also for what is quite possibly the longest Skype conversation history since the dawn of the internet. I also extend a great deal of thanks to my supervisor Henning Flaecher for helping me throughout my PhD with continual support and challenging discussions. Also for the seemingly vast number of thesis iterations and corrections, I'm considerably grateful.

My fellow PhD students with whom I've experienced both the highs and lows of the postgraduate experience, and have always been there to bring me back around with a laugh and a beer. Especially Robin Aggleton, Emrys Clement, Sam Harnew, Jeson Jacob, Donal Hill and Daniel Souza - I thank you.

Also I am incredibly grateful to the many friends and house mates that have helped me, likely without even realising the importance of their actions, by providing such a welcome and great relief from the research world. There are far too many of you to name, but I'm sure you know who you are.

Of course, I couldn't go a whole round of thanks without mentioning the big man himself, Allan 'Ken' Lehan. For the far too many evenings spent drinking far too many whiskies and chain-watching far too many episodes of The Wire, I am hugely grateful (despite most of Season 3 still being only a hazy memory). I take back everything I've ever said - you're alright.

Finally, I would like to extend the greatest of thanks to my family, without whom I simply wouldn't be in the position I am, or the person I've become today. There's not a day goes by that I'm not thankful to have such incredible parents who have encouraged and believed in me always, without fail. For your incredible, never-ending love and support I will be perpetually in debt to you.

For my Dad.

I hope this is worth a McDonald's breakfast.

AUTHOR'S CONTRIBUTION

This work was carried out in collaboration with the Imperial College and Bristol University SUSY groups, building on previous publications. Unless stated otherwise, the work presented in this thesis is that of the authors, or at least where the author was a major contributor. Specifically, the author's unique contributions have been many preceding feasibility studies into the interpretation with charm and four-body stop decay scenarios, including the phenomenological studies of these models presented in Section 2.2.4; early trigger studies, particularly regarding the Parked trigger; the studies leading to the isolation and cleaning of residual QCD contributions from semi-leptonic heavy flavour decays (Section 7.4); the implementation and validation of the Single Isolated Track veto (Section 6.4); the general cross-checking of the analysis using the closure test method (Section 7.3.1); the development and implementation of the signal systematic measurement (Section 9.1 and 9.2); and the final SUSY model limit setting (Section 9.3). The author has been the main contributor to the running of all analysis steps, with the exception of the final trigger efficiency measurements.

*The work of basic scientists like Hertz,
Dobson, and Kaplan can only be driven
by curiosity, not purpose.*

*What is the value of a particular curiosity?
There is no way to know in advance.*

*Discovery is curiosity's product; everything else,
including immeasurable economic value, follows.*

*We cannot know the worth of something
we have not yet discovered.*

*The joy is the rainbow,
not the hope of gold at the rainbow's end.*

Unknown author

ABSTRACT

A search for Supersymmetry in the jets and missing energy final state is described using the CMS detector at the LHC, and the full 18.5 fb^{-1} ‘Parked’ dataset of $\sqrt{s} = 8 \text{ TeV}$ proton-proton collisions. This dataset was collected using experimental, low-threshold triggers to increase sensitivity to softly decaying new physics signatures. The search makes use of the kinematic variable, α_T , to reduce contributions from QCD multijet processes by many orders of magnitude, to a level considered negligible. Remaining background sources originate from electroweak decays of heavy bosons and top quarks, and are estimated using a data-driven technique employing dedicated control regions. To maintain sensitivity to a broad range of potential manifestations of Supersymmetry, the analysis categorises events in dimensions of the scalar sum of hadronic energy, the number of jets and the number of jets originating from b quarks. While this analysis aims to remain inclusive to many hadronically decaying SUSY signatures, the work in this thesis exploits the low energy thresholds of the ‘Parked’ triggers and therefore considers models with compressed mass spectra. As no statistically significant excess is observed, results are interpreted within the context of decays of stop particles relevant in the compressed spectra region. Stop decays to charm quarks and via four-body decays to fermions are considered, both with the weakly interacting Lightest SUSY Particle in the final state. Limits are placed on the mass of the stop of up to 275 GeV for the charm decay and up to 250 GeV for the four-body decay.

TABLE OF CONTENTS

Table of contents	xiii
List of figures	xvii
List of tables	xxvii
1 Introduction	1
2 Theoretical Overview	5
2.1 The Standard Model	5
2.1.1 Failings of the Standard Model	7
2.2 Supersymmetry	9
2.2.1 Why SUSY?	10
2.2.2 Experimental Consequences	12
2.2.3 Simplified Model Spectra	12
2.2.4 Mass-degeneracy in the stop sector	13
3 The LHC and the CMS Detector	17
3.1 The Large Hadron Collider	17
3.2 Compact Muon Solenoid	19
3.2.1 Tracker	22
3.2.2 Electromagnetic Calorimeter	22
3.2.3 Hadronic Calorimeter	23
3.2.4 Muon Systems	23
3.2.5 Trigger	24
4 Object Definitions	27
4.1 Jets	27
4.1.1 Identification jets from b quarks	28

4.2	Muons	29
4.3	Photons	29
4.4	Electrons	29
4.5	Energy Sums	31
4.6	Single Isolated Tracks	31
5	Datasets and MonteCarlo samples	33
5.1	Datasets	33
5.2	MonteCarlo Background and Signal samples	34
5.3	Correcting SM sample cross sections	39
5.3.1	H_T^{parton} binned samples	39
5.3.2	H_T sideband normalisation	39
5.4	Predicting event yields for high b-jet multiplicities	41
6	The α_T Analysis	43
6.1	Analysis Overview	43
6.1.1	The α_T kinematic variable	43
6.2	Standard Model Backgrounds	46
6.2.1	Genuine \cancel{E}_T	46
6.2.2	Fake \cancel{E}_T	47
6.3	Signal Triggers	48
6.4	Selection Criteria	52
6.5	Example distributions and cutflow	53
7	Background Estimation	57
7.1	Overview of Electroweak background prediction method	58
7.2	Control regions	60
7.2.1	μ +jets	60
7.2.2	$\mu\mu$ +jets	62
7.2.3	γ +jets	63
7.3	Systematic uncertainties on SM background predictions	64
7.3.1	Closure tests	65
7.3.2	Background systematic uncertainty summary	67
7.4	Eliminating QCD events	71
7.4.1	Multiple jets below threshold	71
7.4.2	Instrumental effects	72

7.4.3	Heavy-flavour jet decays	73
8	Fit model and Results	79
8.1	Likelihood Model	79
8.1.1	Hadronic Signal Region	79
8.1.2	Electroweak Background Contribution	79
8.1.3	Signal Contribution	81
8.1.4	Total Likelihood	82
8.2	Fit Results	82
8.2.1	Fit without Signal region	83
8.2.2	Fit with Signal region	83
8.2.3	Pulls and p-values	86
8.2.4	Summary	104
9	Interpretation	105
9.1	Signal Acceptance	105
9.1.1	Charm decay	105
9.1.2	Four-body decay	108
9.1.3	ISR Corrections to compressed spectra MC signal samples	110
9.2	Systematic Uncertainties on Signal Acceptance	111
9.2.1	Jet Energy scale	111
9.2.2	Initial State Radiation	112
9.2.3	B tag scale factors	112
9.2.4	PDF	113
9.2.5	H_T/\cancel{E}_T cleaning cut	114
9.2.6	Dead ECAL Filter	114
9.2.7	Generator Level Partons	115
9.2.8	Luminosity Measurement	115
9.2.9	Summary	116
9.3	Limits on models of Supersymmetry	117
9.3.1	Overview of limit setting procedure	117
9.3.2	Limits	118
10	Conclusion	123
Appendix A	Signal Model Systematics Plots	125

LIST OF FIGURES

2.1	Quantum self-corrections to the Higgs mass from a fermionic top quark loop.	8
2.2	The strengths of the gauge coupling parameters, α_{1-3}^{-1} , as a function of the energy scale Q . Dashed lines show the form of the couplings under a SM-only assumption, whereas the coloured lines show their form with the inclusion of the MSSM [27].	10
2.3	Quantum self-corrections to the Higgs mass from a bosonic stop loop.	11
2.4	The most relevant decays of the \tilde{t} in the different Δm regions of the $m_{\tilde{t}}$ vs. $m_{\tilde{\chi}^0}$ mass plane.	13
2.5	Feynman diagrams of the two SMS models considered.	14
2.6	Distributions of the generator level quarks produced in the two-body (left) and four-body (right) decays, prior to any event selection.	14
2.7	Current limits on direct stop production from the CMS (2.7a)[45] and ATLAS (2.7b)[46] experiments as a function of the $m_{\tilde{t}}$ vs. $m_{\tilde{\chi}^0}$ mass plane. Charm decay limits are shown in yellow in 2.7a and red in 2.7b. The four-body decay mode is shown in dark-blue and red in 2.7a and purple in 2.7b.	16
3.1	Schematic diagram of the CERN accelerator complex, showing the various accelerators and storage rings, ultimately feeding the Large Hadron Collider [48].	18
3.2	Schematic diagram of the Large Hadron Collider, indicating the positions of the four collision points and their corresponding detector experiments [49].	18
3.3	The peak instantaneous luminosity for each day throughout 2012 (a), and the integrated luminosity delivered to and recorded at CMS (b) [50].	19

3.4	The average in-time pileup distribution as seen by the CMS detector throughout Run I [50].	20
3.5	Diagram of the Compact Muon Solenoid [52].	21
3.6	Cross section of the CMS detector in the y - z plane, showing the three muon systems (DT, RPC and CSC) as well as other interior sub-detector systems [53].	24
3.7	Schematic overview of the Level-1 hardware trigger system of CMS. η coverage is shown in red text and the data-flow indicated by arrow direction [54].	25
4.1	The Combined Secondary Vertex b tagging algorithm discriminator distribution (left) and the b tagging efficiency (right) as measured in both data and simulation. MC scale factors are shown in the lower plot of 4.1b [64].	28
5.1	Generator level H_T^{parton} distributions from the inclusive DY + jets and the H_T^{parton} binned Z($\nu\nu$) + jets samples, both before and after cross section corrections.	40
6.1	The correlation between \mathbb{H}_T and ΔH_T for MC samples of QCD, $Z \rightarrow \nu\bar{\nu}$ and an example mass point of the charm decay signal model ($m_{\tilde{t}} = 250$ GeV, $m_{\tilde{\chi}^0} = 240$ GeV). Contours of constant α_T are shown in black. Each axis is normalised according to the event H_T . Events are required to have $n_{jet} \geq 4$	45
6.2	The correlation between H_T and \mathbb{H}_T for different α_T values, with the assumption of $\Delta H_T = 0$	46
6.3	Differential (left) and cumulative (right) efficiency turn-on curves for the signal triggers, for the three lowest H_T bins and $2 \leq n_{jet} \leq 3$	50
6.4	Differential (left) and cumulative (right) efficiency turn-on curves for the signal triggers, for the three lowest H_T bins and $n_{jet} \geq 4$	51
6.5	The breakdown of the total electroweak background into component processes as a function of n_{jet} and n_b , for $H_T > 200$ GeV.	53
6.6	Kinematic distributions of all relevant simulated MC samples following the full hadronic signal selection. The sum of the individual sample contributions is shown in green. Plots are for an inclusive selection of $H_T > 200$ GeV, $n_{jet} \geq 2, n_b \geq 0$	54

7.1	Comparison of data with MC for the μ +jets control selection. The plots show an inclusive selection, $H_T > 200$ GeV, $n_{\text{jet}} \geq 2, n_b \geq 0$	61
7.2	Comparison of data with MC for the $\mu\mu$ +jets control selection. The plots show an inclusive selection, $H_T > 200$ GeV, $n_{\text{jet}} \geq 2, n_b \geq 0$	63
7.3	Efficiency turn-on curves for the photon trigger, based on the γ +jets selection, for $H_T > 375$ GeV, with $2 \leq n_{\text{jet}} \leq 3$ (Left) and $n_{\text{jet}} \geq 4$ (Right).	64
7.4	Comparison of data with MC for the γ +jets control selection. The plot shows an inclusive selection, $H_T > 200$ GeV, $n_{\text{jet}} \geq 2, n_b \geq 0$	64
7.5	The results of the eight core closure tests (open symbols), shown over the systematic uncertainty bands for each of the five H_T regions (shaded grey), for the two jet multiplicity regions (a) $2 \leq n_{\text{jet}} \leq 3$ and (b) $n_{\text{jet}} \geq 4$	66
7.6	The results of the eight core closure tests (open symbols), shown over the systematic uncertainty bands for each of the five H_T regions (shaded grey), for $2 \leq n_{\text{jet}} \leq 3$. Included are zeroeth order (left column, blue) and first order (right column, red) fits to each individual closure test.	68
7.7	The results of the eight core closure tests (open symbols), shown over the systematic uncertainty bands for each of the five H_T regions (shaded grey), for $n_{\text{jet}} \geq 4$. Included are zeroeth order (left column, blue) and first order (right column, red) fits to each individual closure test.	69
7.8	The $\mathbb{H}_T/\mathbb{E}_T$ distribution of MC events following the hadronic selection criteria, minus the nominal $\mathbb{H}_T/\mathbb{E}_T$ requirement. The MC yields are stacked, with the QCD contribution shown in cyan. The plot is for a fully inclusive selection of $n_b \geq 0, n_{\text{jet}} \geq 2$ and $H_T > 200$ GeV.	71
7.9	Distribution of jets in (η, ϕ) -space that are responsible for the $\Delta\phi_{\min}^*$ value of an event, with (a, b) and without (c, d) the “Dead ECAL filter” requirement applied as part of the signal region selection.	73
7.10	Data (black points) against the EWK background prediction (stacked, yellow and purple) as a function of $\Delta\phi_{\min}^*$. The expected yield from QCD MC (cyan) is stacked on top of the EWK prediction, but not included in the ratio plot. The plot represents the QCD control study region, with $n_b \geq 0, n_{\text{jet}} \geq 2, H_T > 775$ GeV and $\alpha_T > 0.507$	74

7.11 The α_T distribution for events with no $\Delta\phi_{min}^*$ requirement (red circles) and with the $\Delta\phi_{min}^* > 0.3$ requirement (blue circles) as determined from QCD multijet simulation (left column) or data (right column) and the exclusive $n_{jet} = 3$ (top row) or $n_{jet} = 4$ (bottom row). Note that negligible QCD contamination is seen in the $n_{jet} = 2$ category and consequently is not shown here. The QCD control study region requirements have been applied, $H_T > 775$ GeV and $\alpha_T > 0.507$, with $n_b \geq 0$	75
7.12 Observations in data compared to the EWK background prediction as a function of the \cancel{E}_T variable. An inclusive selection is made in the QCD study region, $H_T > 775$ GeV, $\alpha_T > 0.507$, $n_{jet} \geq 2$ and $n_b \geq 0$. Plots are shown for both the QCD-enriched $\Delta\phi_{min}^* < 0.3$ and QCD-cleaned $\Delta\phi_{min}^* > 0.3$ regions. Yields from QCD MC (cyan) are shown stacked on the total EWK background prediction, but not included in the ratio.	76
7.13 An event display of a typical heavy flavour QCD event, with a jet decaying semi-leptonically with high- p_T neutrinos and therefore considerable generator-level \cancel{E}_T	77
8.1 Pulls for each analysis bin shown as a 1D distribution (Figure 8.1a) and as a function of the H_T bin and analysis category (n_{jet} , n_b) (Figure 8.1b). P-values for every analysis bin shown as a 1D distribution (Figure 8.1c) and for each analysis category, for an inclusive H_T range (Figure 8.1d).	86
8.2 Observations in data for the signal and control regions of the analysis, compared to the result of the full likelihood model simultaneous fit, when the hadronic data observations are not considered. The plots shown are for the $2 \leq n_{jet} \leq 3$, $n_b = 0$ analysis category.	88
8.3 Observations in data for the signal and control regions of the analysis, compared to the result of the full likelihood model simultaneous fit, when the hadronic data observations are not considered. The plots shown are for the $2 \leq n_{jet} \leq 3$, $n_b = 1$ analysis category.	89
8.4 Observations in data for the signal and control regions of the analysis, compared to the result of the full likelihood model simultaneous fit, when the hadronic data observations are not considered. The plots shown are for the $2 \leq n_{jet} \leq 3$, $n_b = 2$ analysis category.	90

8.5	Observations in data for the signal and control regions of the analysis, compared to the result of the full likelihood model simultaneous fit, when the hadronic data observations are not considered. The plots shown are for the $n_{\text{jet}} \geq 4, n_b = 0$ analysis category.	91
8.6	Observations in data for the signal and control regions of the analysis, compared to the result of the full likelihood model simultaneous fit, when the hadronic data observations are not considered. The plots shown are for the $n_{\text{jet}} \geq 4, n_b = 1$ analysis category.	92
8.7	Observations in data for the signal and control regions of the analysis, compared to the result of the full likelihood model simultaneous fit, when the hadronic data observations are not considered. The plots shown are for the $n_{\text{jet}} \geq 4, n_b = 2$ analysis category.	93
8.8	Observations in data for the signal and control regions of the analysis, compared to the result of the full likelihood model simultaneous fit, when the hadronic data observations are not considered. The plots shown are for the $n_{\text{jet}} \geq 4, n_b = 3$ analysis category.	94
8.9	Observations in data for the signal and control regions of the analysis, compared to the result of the full likelihood model simultaneous fit, when the hadronic data observations are not considered. The plots shown are for the $n_{\text{jet}} \geq 4, n_b \geq 4$ analysis category.	95
8.10	Observations in data for the signal and control regions of the analysis, compared to the result of the full likelihood model simultaneous fit. The plots shown are for the $2 \leq n_{\text{jet}} \leq 3, n_b = 0$ analysis category. . . .	96
8.11	Observations in data for the signal and control regions of the analysis, compared to the result of the full likelihood model simultaneous fit. The plots shown are for the $2 \leq n_{\text{jet}} \leq 3, n_b = 1$ analysis category. . . .	97
8.12	Observations in data for the signal and control regions of the analysis, compared to the result of the full likelihood model simultaneous fit. The plots shown are for the $2 \leq n_{\text{jet}} \leq 3, n_b = 2$ analysis category. . . .	98
8.13	Observations in data for the signal and control regions of the analysis, compared to the result of the full likelihood model simultaneous fit. The plots shown are for the $n_{\text{jet}} \geq 4, n_b = 0$ analysis category.	99
8.14	Observations in data for the signal and control regions of the analysis, compared to the result of the full likelihood model simultaneous fit. The plots shown are for the $n_{\text{jet}} \geq 4, n_b = 1$ analysis category.	100

8.15 Observations in data for the signal and control regions of the analysis, compared to the result of the full likelihood model simultaneous fit. The plots shown are for the $n_{\text{jet}} \geq 4, n_b = 2$ analysis category.	101
8.16 Observations in data for the signal and control regions of the analysis, compared to the result of the full likelihood model simultaneous fit. The plots shown are for the $n_{\text{jet}} \geq 4, n_b = 3$ analysis category.	102
8.17 Observations in data for the signal and control regions of the analysis, compared to the result of the full likelihood model simultaneous fit. The plots shown are for the $n_{\text{jet}} \geq 4, n_b \geq 4$ analysis category.	103
9.1 Signal efficiency times acceptance of the $\text{pp} \rightarrow \tilde{t}\tilde{t}^* \rightarrow c\tilde{\chi}^0 \bar{c}\tilde{\chi}^0$ simplified model, for the hadronic selection (left) and the $\mu+\text{jets}$ selection (right), shown for the four most sensitive analysis categories with an inclusive selection on H_T	107
9.2 Signal efficiency times acceptance of the $\text{pp} \rightarrow \tilde{t}\tilde{t}^* \rightarrow bff'\tilde{\chi}^0 bff'\tilde{\chi}^0$ simplified model, for the hadronic selection (left) and the $\mu+\text{jets}$ selection (right), shown for the four most sensitive analysis categories with an inclusive selection on H_T	109
9.3 Data to MC comparisons for an enriched $Z \rightarrow l\bar{l}$ selection, with the vectorial sum of lepton p_T 's (left) and of the recoil jets (right) [85]. . .	110
9.4 Example distributions of the test statistic, q_μ for Signal+Background (orange) and Background-only (blue) scenarios. The observed value of q_μ is shown in black, with orange and blue quantiles representing CL_{s+b} and CL_b respectively.	118
9.5 The expected limit (red dashed line) with central band (thick red) and $\pm 1\sigma$ and $\pm 2\sigma$ uncertainty bands (thin red), and the observed limit (thick black) for the charm decay model. The limit is calculated with an inclusive $H_T > 200$ GeV selection, and the analysis categories ($n_b = 0, 2 \leq n_{\text{jet}} \leq 3$), ($n_b = 1, 2 \leq n_{\text{jet}} \leq 3$), ($n_b = 0, n_{\text{jet}} \geq 4$), ($n_b = 1, n_{\text{jet}} \geq 4$).	120

A.6 The acceptance of the DeadECAL cut as a function of the charm decay model mass plane. Each plot represents one of the four most sensitive analysis categories (n_b , n_{jet}), with the inclusive requirement $H_T > 200$ GeV.	130
A.7 The total systematic uncertainty as a function of the charm decay model plane, where all individual systematic contributions are summed in quadrature. Each plot represents one of the four most sensitive analysis categories (n_b , n_{jet}), with the inclusive requirement $H_T > 200$ GeV.	131
A.8 The relative change in acceptance times signal efficiency for the four-body decay model for downwards (left) and upwards (middle) fluctuations of all jet energies by the uncertainty of the jet energy scale, and the derived systematic values (right). The plots represent a fully inclusive selection - $n_{jet} \geq 2$, $n_b \geq 0$ and $H_T > 200$ GeV.	132
A.9 The relative change in acceptance times signal efficiency for the four-body decay model for downwards (left) and upwards (middle) fluctuations of the global event weight equal to the magnitude of the ISR corrections, and the derived systematic values (right). Each set of plots corresponds to one of the four most sensitive analysis categories (n_b , n_{jet}), with the inclusive requirement $H_T > 200$ GeV.	133
A.10 The relative change in acceptance times signal efficiency for the four-body decay model for downwards (left) and upwards (middle) fluctuations of global event weight according to the uncertainties of the Btag scale factors, and the derived systematic values (right). Each set of plots corresponds to one of the four most sensitive analysis categories (n_b , n_{jet}), with the inclusive requirement $H_T > 200$ GeV.	134
A.11 The acceptance of the $\mathcal{H}_T/\mathcal{E}_T$ cut as a function of the four-body decay model mass plane. Each plot represents one of the four most sensitive analysis categories (n_b , n_{jet}), with the inclusive requirement $H_T > 200$ GeV.	135
A.12 The acceptance of the DeadECAL cut as a function of the four-body decay model mass plane. Each plot represents one of the four most sensitive analysis categories (n_b , n_{jet}), with the inclusive requirement $H_T > 200$ GeV.	136

A.13 The total systematic uncertainty as a function of the four-body decay model mass plane, where all individual systematic contributions are summed in quadrature. Each plot represents one of the four most sensitive analysis categories (n_b , n_{jet}), with the inclusive requirement $H_T > 200$ GeV.	137
---	-----

LIST OF TABLES

2.1	The fermionic particle content of the Standard Model [8].	6
2.2	The bosonic particle content of the Standard Model [8].	7
2.3	The particle content of the Minimally Supersymmetric Standard Model. Note that there are now two Higgs doublets present.	9
4.1	Criteria for the “loose” jet identification working point.	28
4.2	Muon identification (Tight working point).	29
4.3	Photon identification (Tight working point).	30
4.4	Electron identification (Loose working point).	30
4.5	\cancel{E}_T filters employed in the analysis, as recommended by the MET <i>POG</i> . .	32
4.6	Single Isolated Track identification.	32
5.1	8 TeV Datasets with the integrated luminosity for each.	33
5.2	MC samples for Standard Model processes with their NNLO cross sections and equivalent integrated luminosity.	36
5.3	MC samples for Simplified Model Spectra.	38
5.4	The process-specific sideband corrections applied to MC sample, with the selection used and its corresponding purity.	40
6.1	H_T bin lower bounds used for each n_{jet} and n_b category.	44
6.2	Signal triggers, the L1 seed triggers and their efficiencies measured for per H_T and n_{jet} category.	48
6.3	Jet E_T and α_T thresholds per H_T bin.	52
6.4	The cutflow of the hadronic selection in data. The subscript ‘fail’ indicates an object which did not meet all ID requirements, and so is not considered as a ‘common object’. The event selection follows an inclusive selection in data of $H_T > 375$ GeV, $n_{\text{jet}} \geq 2$ and $n_b \geq 0$	55

7.1	The control regions used to produce SM background predictions for each analysis category (n_b , n_{jet})	59
7.2	Muon trigger efficiencies (%) for the $\mu+jets$ selection listed by H_T bin and n_{jet} category.	61
7.3	Muon trigger efficiencies (%) for the $\mu\mu+jets$ selection listed by H_T bin and n_{jet} category.	62
7.4	Results of zeroeth (i.e. constant) and first order (i.e. linear) fits for five sets of closure tests, performed in the $2 \leq n_{jet} \leq 3$ category.	67
7.5	Results of zeroeth (i.e. constant) and first order (i.e. linear) fits for five sets of closure tests, performed in the $n_{jet} \geq 4$ category. An additional test marked with a † is listed, as described in the text.	70
7.6	Results of zeroeth (i.e. constant) and first order (i.e. linear) fits for the three sets of closure tests probing the accuracy of jet multiplicity modelling in MC, for each control region.	70
7.7	Summary of the magnitude of systematic uncertainties (%) on the EWK background prediction, derived from the eight core closure tests, for each n_{jet} category and H_T region.	70
8.1	Summary of likelihood nuisance parameters.	82
8.2	Summary of the “a-priori” fit. ‘SM’ entries represent the prediction of the full SM background, obtained from the fit procedure.	84
8.3	Summary of the “a-posteriori” fit. ‘SM’ entries represent the prediction of the full SM background, obtained from the fit procedure.	85
9.1	Cutflow table for two mass points ($m_{\tilde{t}} = 250$ GeV, $m_{\tilde{\chi}^0} = 240$ GeV and $m_{\tilde{t}} = 250$ GeV, $m_{\tilde{\chi}^0} = 170$ GeV) of the charm decay signal model. The selection represents the hadronic signal region for the $H_T > 375$ GeV region.	106
9.2	Cutflow table for two mass points ($m_{\tilde{t}} = 250$ GeV, $m_{\tilde{\chi}^0} = 240$ GeV and $m_{\tilde{t}} = 250$ GeV, $m_{\tilde{\chi}^0} = 170$ GeV) of the four-body decay signal model. The selection represents the hadronic signal region for the $H_T > 375$ GeV region.	108
9.3	Correction factors for MADGRAPH based signal samples to account for MC over-prediction of ISR.	111
9.4	Systematic factors for MADGRAPH based signal samples to determine ISR modelling related systematics.	112

9.5	Efficiencies of the $\cancel{H}_T/\cancel{E}_T$ requirement cut for the $\mu+\text{jets}$ selection in data ϵ_{data} and MC ϵ_{MC} , as well as the ratio of both. Efficiencies are shown for the two n_{jet} categories and the four lowest H_T bins, with an inclusive requirements are made of n_b	114
9.6	Efficiencies of the dead ECAL filter for the $\mu+\text{jets}$ selection in data ϵ_{data} and MC ϵ_{MC} , as well as the ratio of both. Efficiencies are shown for the two n_{jet} categories and the four lowest H_T bins, with an inclusive requirements are made of n_b	115
9.7	Relative change in efficiency times acceptance for the 2-parton and 3-parton scans in the signal region, with an inclusive selection on n_b and $H_T > 200$ GeV. The scan points are $m_{\tilde{t}} = 200$ GeV and $m_{\tilde{\chi}^0} = (120, 190)$ GeV in the charm decay model.	116
9.8	Representative ranges for each contribution to the total systematic uncertainty on the signal efficiency times acceptance for each relevant event category for the charm decay model interpretation.	116
9.9	Representative ranges for each contribution to the total systematic uncertainty on the signal efficiency times acceptance for each relevant event category for the four-body decay model interpretation.	117

CHAPTER 1

INTRODUCTION

Our instinctive method of understanding is reductive - the idea of an inventor attempting to make sense of the things around them is that of toasters, clock radios, or even gearboxes broken down into their smallest constituent parts to better understand what they're made of and, ultimately, what's happening inside of them. This simple idea translates perfectly to explain the work Particle Physicists undertake with not simple everyday objects, but the Universe.

Since the fields inception, physicists have questioned the Universe around us, and what it's made of. From the early research of scientists such as Ernest Rutherford and Niels Bohr, the basic building blocks of the universe have been searched for. For Particle Physicists, this is the ultimate goal - a complete understanding of the nature of the Universe at its most fundamental level. If a description can be written of these fundamental building blocks of nature and how they interact, then ultimately we can understand the Universe from the bottom up.

Currently, our best attempt of such a description comes from the intersection of two fields: Quantum Mechanics, the study of microscopic objects, and Relativity, the study of very fast objects. The combination of these two very different worlds gave birth to the field of Relativistic Quantum Mechanics, and ultimately, the Standard Model (SM).

First proposed in the 1960's, the Standard Model attempts to describe the properties of the fundamental constituents of matter, and outline their interactions through three of the four fundamental forces of nature, as described in Chapter 2. By withstanding substantial scrutiny from countless experiments since its inception, the Standard Model has proven itself to be an exceptional triumph of modern physics.

Despite its continued accuracy, however, the Standard Model fails to account for

significant observations, for example the absent description of gravity and the ‘other’ 96% of the Universe - the so-called ‘Dark Sector’. In addition the Standard Model fails to unify the fundamental forces at some higher mass scale, or predict the masses of particles, such as the newly discovered Higgs boson. Given how successfully it describes what it can, the SM is widely considered as a smaller component of some greater, all-encompassing theory. This belief has led many to use this distinct theory as a building block on which extensions can be introduced to create Beyond the Standard Model (BSM) theories - the goal being to fill the gaps in knowledge left by the SM.

Of the plethora of BSM theories, one particularly well motivated extension is Supersymmetry (SUSY). The supersymmetric extension to the Standard Model introduces supersymmetric particles (or ‘sparticles’) differing from their SM partners by half a unit of spin - described in greater detail in Chapter 2. The addition of sparticles fixes many of the Standard Model’s problems, most notably that of the divergent Higgs Mass, the Unification of the fundamental gauge couplings and, crucially, provides a feasible candidate particle for the elusive Dark Matter observed in abundance in the Universe.

Particle physics as a field has developed largely via a cat and mouse game, played out between theorists and experimentalists. While theoretical physicists have developed new theories and proposed new particles, experimentalists have raced to build greater and more advanced experiments with which to discover them. Today, thanks to the incredible work of thousands of physicists and engineers, we are able to test such BSM theories with the Large Hadron Collider (LHC) in Geneva, Switzerland.

The LHC, described in Chapter 3, is a 27 km circumference proton synchrotron, capable of colliding protons at centre-of-mass energies far exceeding any previous experiment. Using the LHC, it is possible to reproduce the conditions observed a short time after the Big Bang, where the incredibly high energies present were able to produce countless particles that wouldn’t be visible in today’s universe. If such exotic particles are created in the proton-proton collisions performed at the LHC, it is the goal of detector experiments such as the Compact Muon Solenoid (CMS) to find them.

The CMS detector, also described in Chapter 3, is comprised of multiple sub-detector systems, each designed specifically to make precise measurements of the characteristics of the different particles created in the fierce collisions. The detector is built such that it provides almost complete hermetic coverage to detect particles travelling in all directions from the point of interaction. Energy deposits throughout the detector subsystems are used to form physics objects, as summarised in Chapter 4,

themselves allowing the events to be categorised by the physics processes present.

A key technique for searches for SUSY is the study of global momentum imbalances, which allows for the presence of weakly interacting particles to be inferred. If sparticles were to be produced at the LHC they would likely decay immediately to many well-understood SM particles, and finally the weakly interacting ‘Lightest Supersymmetric Particle’ (LSP) - the theory’s Dark Matter candidate. Of the many different possible supersymmetric decays, hadronic channels offer the largest branching fractions, although can present some of the most difficult experimental challenges. Hadronic searches are of interest given their relatively simple and quick ability to provide sensitivity to early discovery at hadronic colliders such as the LHC.

The work described in this thesis consists of such a search for SUSY particles decaying to quarks and missing-energy. The analysis makes use of the full ‘Parked’ data sample collected throughout 2012, where experimental triggers collected events with lower energy thresholds than the standard data stream. These lowered thresholds greatly improve analysis sensitivity to soft physics processes, such as those expected from SUSY scenarios with nearly degenerate mass hierarchies. The data samples and corresponding MonteCarlo simulated samples used in this analysis are detailed in Chapter 5.

The biggest obstacle to searching for hadronic signatures of new physics, is dealing with the overwhelming hadronic backgrounds from Quantum Chromodynamics (QCD). In this analysis a powerful kinematic variable, α_T , is used to differentiate between such QCD and potential signal events. The analysis backgrounds, selection and the α_T variable are described in detail in Chapter 6. The remaining SM sources of background are estimated using a data-driven transfer technique from dedicated control regions, orthogonal to the search region, as outlined in Chapter 7. The results of the transfer technique are included as part of a simultaneous likelihood model fit to the signal and all control regions to determine final background counts as described in Chapter 8.

Given the vast number of potential manifestations of SUSY, sparticles may decay in many different ways if produced. Accordingly, Chapter 8 also gives the results of this analysis, categorising events in dimensions of three different event-level variables: the total sum of visible transverse hadronic energy, the number of jets and the number of b-tagged jets. Specific analysis categories are used to produce targeted interpretations of different potential final states, thereby maintaining a broad sensitivity to SUSY production, however it may present itself in nature. As motivated by Dark Matter

observations, the interpretations presented in this thesis represent two different decay channels of the produced \tilde{t} sparticle in the so-called ‘compressed’ region, where the mass of the \tilde{t} is near-degenerate with that of the LSP. Accordingly, limits on the mass of the \tilde{t} and the LSP are produced. These interpretations and discussions of the related efficiencies and systematics are presented in Chapter 9, before final conclusions are made in Chapter 10.

Natural units ($\hbar = c = 1$) are used throughout this work.

CHAPTER 2

THEORETICAL OVERVIEW

The Standard Model (SM), proposed in the 1960's, has long been the most prominent and successful description of fundamental particles and their interactions at the energies currently experimentally accessible. Its power has been proven with the theoretical prediction of particles such as the charm and top quarks, and the W and Z bosons, prior to their experimental observation. Furthermore, precision electroweak measurements have shown impressive levels of agreement with SM predictions [1].

However, despite its great success, the theory is known to be valid only for low energies, and is missing significant details of both experimentally observed and theoretically predicted physical phenomena. As such, extensions to the SM have been extensively studied, assuming the SM to be the low-energy regime of some greater theory. One such strongly theoretically motivated extension to the SM is Supersymmetry (SUSY).

This chapter first outlines the SM model, including its particle content and basic mechanisms, before describing its shortcomings - the theoretical motivation for Beyond the Standard Model (BSM) theories. SUSY will then be introduced, before describing its simplest incarnations, along with a discussion of the specific models and frameworks used for interpretation within this analysis.

2.1 The Standard Model

The Standard Model is a renormalisable Quantum Field Theory (QFT) describing fundamental matter particles and their interactions via the strong, weak and electromagnetic forces. It was collaboratively developed throughout the 1960's [2–6], with its current Lagrangian based formalism being finalised in the mid-1970's [7].

Requiring local gauge invariance of the SM Lagrangian, \mathcal{L}_{SM} , under transformations generated by continuous symmetry groups, the structure and interactions of the SM can be formed. Noether's theorem relates the symmetries of a physical system with conserved quantities, and accordingly interactions in the SM include such quantities. The $SU(3)$ group describes strong force interactions with colour charge, and $SU(2)$ and $U(1)$ to describe electroweak interactions with weak isospin and hypercharge respectively.

Matter particles, summarised in Table 2.1, are described by spin 1/2 fermions divided into the six quarks and six leptons. The quarks are arranged into three generations: the up(u) and down(d), the charm(c) and strange(s), and the top(t) and bottom(b), each couplet carrying individual electric charges of +2/3 and -1/2 respectively. The quarks also carry colour charge, where combinations of quarks form colour-neutral composite hadron particles which are observed in nature.

The leptons are similarly arranged into three generations, constructed from $SU(2)$ doublets of weak isospin, $(\nu_L, l)_L$, of left-handed chiral states, and singlets, l_R , of right-handed chiral states, where l represents either the electron (e), muon (μ) or tau (τ). Each carries a -1 electrical charge and ν_L are their corresponding electrically neutral neutrinos.

Table 2.1 The fermionic particle content of the Standard Model [8].

Name	Type	Spin	Charge (e)	Mass
Electron (e)	Lepton	1/2	-1	0.511 MeV
Electron Neutrino (μ_e)	Lepton	1/2	0	< 2 eV
Muon (μ)	Lepton	1/2	-1	105.658 MeV
Muon Neutrino (ν_μ)	Lepton	1/2	0	< 0.19 MeV
Tau (τ)	Lepton	1/2	-1	1.776 GeV
Tau Neutrino (ν_τ)	Lepton	1/2	0	< 18.2 MeV
Up (u)	Quark	1/2	+2/3	$2.3^{+0.7}_{-0.5}$ MeV
Down (d)	Quark	1/2	-1/3	$4.8^{+0.5}_{-0.3}$ MeV
Charm (c)	Quark	1/2	+2/3	1.28 ± 0.03 GeV
Strange (s)	Quark	1/2	-1/3	95.0 ± 5.0 MeV
Top (t)	Quark	1/2	+2/3	173.21 ± 0.87 GeV
Bottom (b)	Quark	1/2	-1/3	4.66 ± 0.03 GeV

Interactions between the fermions are mediated by spin-1 bosons, summarised in Table 2.2. The strong force, $SU(3)$, is represented by eight electrically neutral, massless gluons (g), each carrying a colour charge. The electroweak force, $SU(2) \times U(1)$, is mediated by the electrically neutral, massless photon (γ), the massive, neutral Z^0 ,

Table 2.2 The bosonic particle content of the Standard Model [8].

Name	Force Carried	Spin	Charge (e)	Mass
W Boson (W)	Weak	1	± 1	80.385 ± 0.02 GeV
Z Boson (Z)	Weak	1	0	91.188 ± 0.002 GeV
Gluon (g)	Strong	1/2	0	-
Photon (γ)	Electromagnetism	0	0	-
Higgs Boson (H)	-	0	0	125.7 ± 0.4 GeV

and the massive, electrically charged W^\pm bosons.

Following the enforcement of local gauge invariance after an $SU(2) \times U(1)$ transformation, the bosonic mediator of the $U(1)$ symmetry, the γ , remains massless as expected. However so do the W^\pm and Z^0 , in disagreement with their experimentally observed masses. To remedy this, the $SU(2) \times U(1)$ symmetry undergoes Electroweak Symmetry Breaking (EWSB) via the Higgs Mechanism [9–11], leading to the Higgs boson, H^0 , a massive, electrically neutral, spin-0 scalar particle, thereby completing the formalism of the Standard Model.

2.1.1 Failings of the Standard Model

While the Standard Model has provided many accurate predictions and descriptions which have been extensively experimentally verified [12], the theory is considered incomplete due to gaps in its description of the Universe.

The SM provides a QFT description of how the strong, weak and electromagnetic forces work on a quantum level, however it fails to include any description of the final fundamental force, gravity. A quantum description of gravity has long been sought after by particle theorists, in particular to provide an explanation for its relative weakness at the Electroweak scale with respect to the other fundamental forces.

Following the Big Bang it is believed matter and anti-matter were created in equal amounts, however given that we are in a matter dominated universe there must exist some physical process by which an asymmetry came to be between the two types of matter - the so-called ‘Baryogenesis’ process. This requires the violation of the Charge-Parity (CP) symmetry, however the amount of CP violation described by the Standard Model does not appear to be significant enough to achieve this [13, 14].

In the SM, following the local gauge invariance requirement of the electroweak sector, $SU(2) \times U(1)$, the $SU(2)$ doublets contain massless neutrino particles. However, experimental observations of neutrino oscillation between their various flavours

indicate them to have finite mass [15, 16], and therefore mix between different mass eigenstates. This is only described by extending the Standard Model to include neutrino mixing, defined by the PMNS matrix [17].

Furthermore, and of particular relevance to the work in this thesis, are the Hierarchy Problem and the existence of Dark Matter.

The Hierarchy Problem

Particles couple to the Higgs field according to the Yukawa couplings, λ_f , proportional to the mass of the particle. For fermions, the Lagrangian interaction term is

$$\mathcal{L}_{\text{Yukawa}} = -\lambda_f \bar{\Psi} H \Psi, \quad (2.1)$$

where Ψ is a spin-1/2 Dirac field, and H the Higgs field. Higgs mass corrections due to beyond tree-level interactions with fermion fields (shown in Figure 2.1) can be shown to result in

$$\Delta m_H^2 \propto -|\lambda_f|^2 \Lambda_{\text{cut}}^2, \quad (2.2)$$

where Λ_{cut} is the cut-off energy scale, up to which the SM is valid, typically taken to be the Planck scale. This therefore leads to a quadratically divergent correction to m_H . Such corrections cause significant tension between the theoretically allowed value of m_H and the experimentally measured value, $m_H \simeq 125$ GeV [18], requiring significant ‘fine-tuning’ to bring the two into agreement. This is known as the Hierarchy Problem.

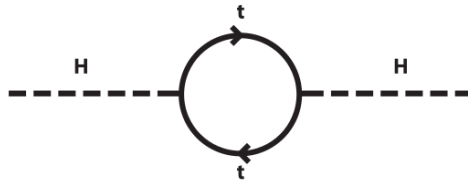


Fig. 2.1 Quantum self-corrections to the Higgs mass from a fermionic top quark loop.

Dark Matter

Significant amounts of Dark Matter (DM) have been indirectly observed through the study of galaxy rotation curves and gravitational lensing techniques [19]. It is estimated that Dark Matter represents 26.8% of the energy content of Universe, with

normal Baryonic matter representing only 4.9% [20]. For such a large relative abundance to be present DM must be massive and weakly interacting. No candidate particle exists in the SM to describe such matter.

2.2 Supersymmetry

At its core, Supersymmetry (SUSY) is a new space-time symmetry between fermions and bosons [21–26]. An operator of SUSY acting on a fermion (boson) state acts to change the spin by a 1/2, producing a super-partner boson (fermion) state, maintaining electric charge, colour charge and weak isospin. A theory invariant under such transformations is said to be supersymmetric.

As a consequence of this new symmetry, SUSY introduces a rich phenomenology of new particles ('sparticles'). The simplest model of SUSY is the Minimally Supersymmetric Standard Model (MSSM) [27] - a so-called 'complete' model, containing more than 100 free-parameters representing sparticle masses, phases and mixing angles [28]. Within the MSSM, the SU(2) doublets and singlets, $(\nu_L, l)_L$ and l_R , have super-partners $(\tilde{\nu}_L, \tilde{l})_L$ and \tilde{l}_R . Similarly for SU(3), $(q, q')_L$ and q_R , have super-partners $(\tilde{q}_L, \tilde{q}')_L$ and \tilde{q}'_R . The spin-1 SM gauge bosons have spin-1/2 gaugino partners, the gluino, winos and bino, \tilde{g} , \tilde{W}^\pm , \tilde{W}^0 , \tilde{B}^0 . The Higgs sector is extended to include two Higgs-doublets giving five mass-eigenstates, h^0 , H^0 , A^0 and H^\pm . Finally, the gauginos and the neutral higgsinos mix to give the neutralinos, $\tilde{\chi}_{i=1-4}^0$, and the winos and charged higgsinos mix to give the charginos, $\tilde{\chi}_{i=1-2}^\pm$.

Table 2.3 The particle content of the Minimally Supersymmetric Standard Model. Note that there are now two Higgs doublets present.

Sparticle	Partner	Spin	Charge (e)
$\tilde{\chi}_0^0, \tilde{\chi}_1^0, \tilde{\chi}_2^0, \tilde{\chi}_3^0$	γ, Z, H^0, h^0	1/2	0
$\tilde{\chi}_0^\pm, \tilde{\chi}_1^\pm$	W^\pm, H^\pm	1/2	± 1
$\tilde{e}_L, \tilde{e}_R, \tilde{\nu}_e, \tilde{\mu}_L, \tilde{\mu}_R, \tilde{\nu}_\mu, \tilde{\nu}_\tau$	$e, \nu_e, \mu, \nu_\mu, \nu_\tau$	1	$\pm 1, 0$
$\tilde{\tau}_L, \tilde{\tau}_R$	τ	1	± 1
$\tilde{u}_L, \tilde{u}_R, \tilde{d}_L, \tilde{d}_R, \tilde{s}_L, \tilde{s}_R, \tilde{c}_L, \tilde{c}_R$	u, d, s, c	1	$\pm 1/3, \pm 2/3$
\tilde{b}_L, \tilde{b}_R	b	1	$\pm 1/3, \pm 2/3$
\tilde{t}_L, \tilde{t}_R	t	1	$\pm 1/3, \pm 2/3$
\tilde{g}	g	1/2	0

Given the lack of experimental evidence for SUSY, sparticles must have higher masses than their SM partners, implying that Supersymmetry is not an exact symmetry and must be broken by some mechanism [29, 30].

2.2.1 Why SUSY?

The supersymmetric extension to the SM provides solutions to many of the original theory's shortcomings.

Unification of the Gauge Couplings

Within a Grand Unified Theory (GUT) it is desirable for the running constants related to the gauge couplings to unify at some higher energy scale. While not possible in the SM, with the introduction of a supersymmetric extension, such as the MSSM, the strength parameters are indeed able at some higher energy scale, as shown in Figure 2.2.

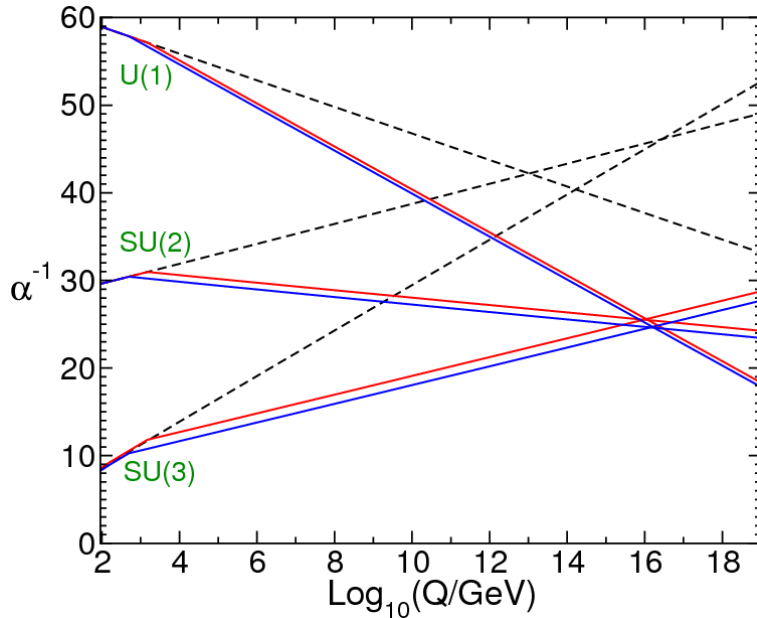


Fig. 2.2 The strengths of the gauge coupling parameters, α_{1-3}^{-1} , as a function of the energy scale Q . Dashed lines show the form of the couplings under a SM-only assumption, whereas the coloured lines show their form with the inclusion of the MSSM [27].

Hierarchy Problem

While in the SM the Higgs gains corrections to its mass from fermion-loop induced self-interactions, the presence of bosonic super-partners to these fermions in a SUSY model provides additional diagrams (Figure 2.3). These contribute oppositely signed terms,

$$\Delta m_H^2 \propto +\lambda_S \Lambda_{\text{cut}}^2, \quad (2.3)$$

where λ_S is the bosonic super-partner's Yukawa coupling. The introduction of these super-partners, and therefore their additional corrective terms, provides an elegant solution to the hierarchy problem. Quadratic divergences to m_H are effectively cancelled by sparticle loop contributions, with only a logarithmic divergence remaining, arising due to the necessity of breaking SUSY.



Fig. 2.3 Quantum self-corrections to the Higgs mass from a bosonic stop loop.

Dark Matter

In many supersymmetric theories, a new conserved quantum number R_P is introduced in order to conserve lepton and baryon number [31], defined as

$$R_P = (-1)^{3B+L+2s} \left(\begin{array}{c} = +1 \text{ for SM particles} \\ = -1 \text{ for SUSY particles} \end{array} \right), \quad (2.4)$$

where B is Baryon number, L is Lepton number and s is spin. SM particles have $R_P = +1$, whereas SUSY particles have $R_P = -1$. R_P is a multiplicative quantum number, therefore sparticles can only be pair-produced. The subsequent sparticle decay will then consist of a cascade-type decay, with each sparticle decaying to a final state containing a lighter, kinematically accessible sparticle and a SM particle. This process will continue until the lightest supersymmetric particle (LSP) is reached, which is therefore stable. Within R-Parity conserving models in which the $\tilde{\chi}^0$ is the LSP, this particle is able to provide a stable, weakly interacting dark matter candidate [32].

2.2.2 Experimental Consequences

In order for SUSY to provide an adequate solution to the hierarchy problem, sparticle masses are required to be around the TeV scale [29, 30, 33]. This fact, coupled with strong experimental bounds on constrained models and the discovery of the Higgs in a mass-region compatible with the MSSM, have led interest towards ‘Natural’ SUSY models. Such models assume the first and second generation squarks to be very heavy, while the third generation be around 1 TeV in order to solve the hierarchy problem without significant fine-tuning [34, 35].

2.2.3 Simplified Model Spectra

While ‘complete’ supersymmetric models offer a full description of all aspects of a given theory (e.g. mass spectra and mixing angles), the large number of free parameters becomes unmanageable for interpretations of experimental observations. Even in models such as the Constrained-MSSM (CMSSM) with 5 free parameters [36, 37], the interpretation phase-space remains vast.

In an effort to make interpretations of experimental data simpler for experimentalists, while remaining universally of use to theorists, Simplified Model Spectra (SMS) were developed [38, 39]. SMS consist of simplified decay scenarios which can later be reinterpreted within the context of complete models. Typically SMS consist of either squark or gluino pair-production, with a subsequent decay to a given final state with a 100% branching fraction. A crucial consequence of these models is to effectively move experimental searches away from ‘model-specific’ interpretations and towards more ‘signature-specific’ interpretations [40].

SMS generally contain only two free parameters, normally the mass of a produced mother particle, m_{mother} , and the mass of the LSP, m_{LSP} . Therefore interpretations can be made over a simple 2-dimensional parameter space, making for trivial experimental comparisons.

SMS prove to be an excellent tool for the interpretation of results within the bounds of naturalness as many SMS consider third generation squark production, allowing for direct limits to be placed on the dominant decays of stop and sbottom squarks.

2.2.4 Mass-degeneracy in the stop sector

SUSY models with particle mass hierarchies spanning a small mass range are said to be ‘compressed’. When considered in terms of a simplified model scenario, this implies the pair-produced mother sparticle is close in mass to that of the LSP. The smaller the mass difference, Δm ($= m_{mother} - m_{LSP}$), the greater the experimental challenge, as visible decay products become softer and typically fall out of analysis acceptance.

Figure 2.4 shows the dominant decay processes of the \tilde{t} . Across most of mass plane decay channels are dominated by $\tilde{t} \rightarrow t\tilde{\chi}^0$ and $\tilde{t} \rightarrow bW\tilde{\chi}^0$, with the latter decaying via an intermediate $\tilde{\chi}^\pm$. However, when $\Delta m < m_W$ the W-boson is no longer kinematically accessible and goes off-shell. Consequently these two decay channels are no longer relevant and \tilde{t} decay branching fractions become dominated by the two-body decay $\tilde{t} \rightarrow c\tilde{\chi}^0$, and the four-body decay $\tilde{t} \rightarrow bff'\tilde{\chi}^0$ ($f = \ell, q$) [41]. In this region, these two decay channels can provide a dark-matter relic density consistent with cosmological observations (e.g. from WMAP [42]), where annihilation cross sections are mediated by co-annihilation with the light stop proposed by naturalness [43, 44].

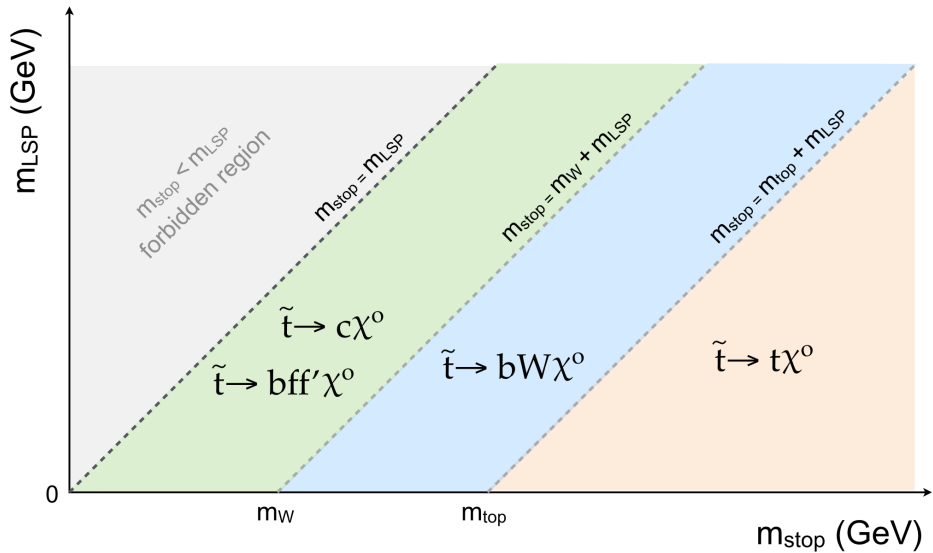


Fig. 2.4 The most relevant decays of the \tilde{t} in the different Δm regions of the $m_{\tilde{t}}$ vs. $m_{\tilde{\chi}^0}$ mass plane.

The interpretation of the analysis results will therefore focus on the two \tilde{t} decays relevant in this highly-compressed region of SUSY phase space, namely the two-body charm decay ($pp \rightarrow \tilde{t}\tilde{t}^* \rightarrow c\tilde{\chi}^0\bar{c}\tilde{\chi}^0$) and the four-body decay ($pp \rightarrow \tilde{t}\tilde{t}^* \rightarrow bff'\tilde{\chi}^0 bff'\tilde{\chi}^0$). The main diagram for each is shown in Figure 2.5.

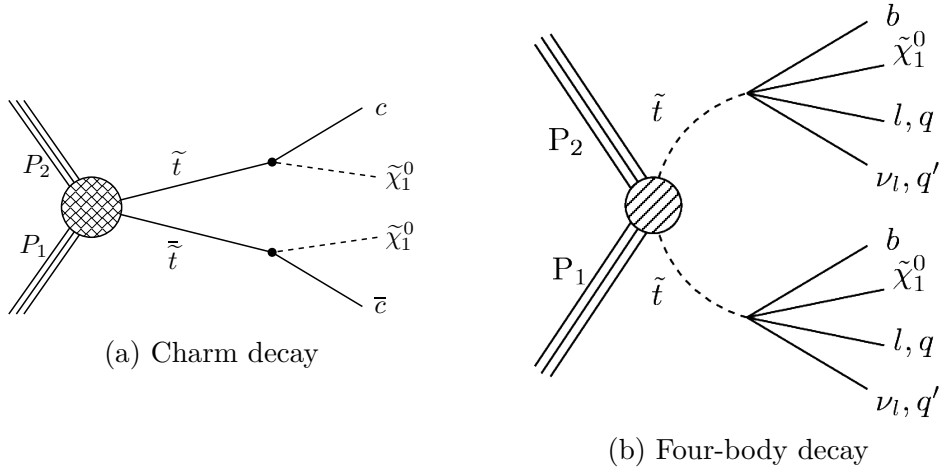


Fig. 2.5 Feynman diagrams of the two SMS models considered.

Phenomenology

In the compressed region, characterised by small values of Δm , decay products of the \tilde{t} pair have very low momenta given the small amounts of energy release in the decay following the production of the $\tilde{\chi}^0$. For example, Figure 2.6a shows the transverse momentum of the generator level charm quark originating from the decay of the \tilde{t} getting smaller with decreasing values of Δm . Figure 2.6b shows the same observation for the p_T of the b quark present from the decay of the \tilde{t} in the four-body decay.

The low amounts of available energy in the small Δm region present considerable experimental challenges, and as such this region in the past has typically not been

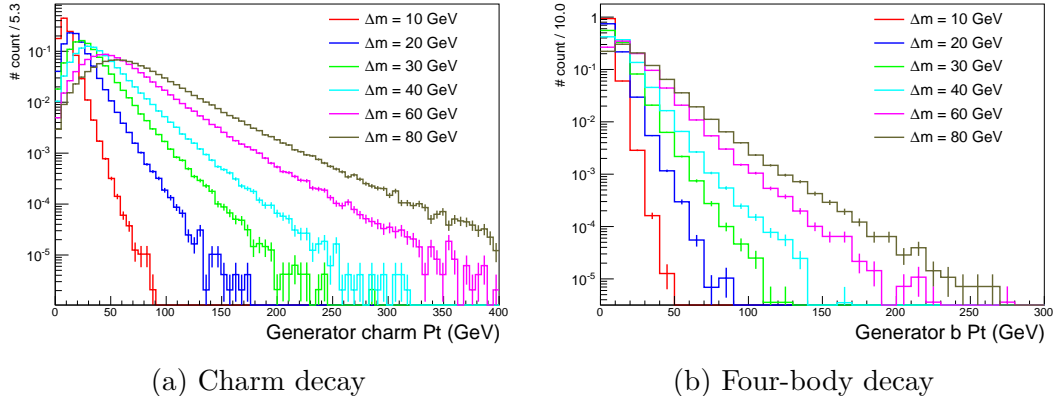


Fig. 2.6 Distributions of the generator level quarks produced in the two-body (left) and four-body (right) decays, prior to any event selection.

considered for interpretations. The acceptance of such models in this region is heavily reliant on initial state particles radiated from the incoming partons, thereby boosting the decaying stops. This feature of compressed models and its importance to analysis sensitivity is discussed later in Chapter 9.

Current Experimental Limits

Given the current lack of experimental observation, limits for direct \tilde{t} production are shown in Figure 2.7. Figure 2.7a shows the observed limits from the CMS experiment across the stop mass plane. Most notably, the limit for the charm decay is shown in yellow in the $\Delta m < 80$ GeV region. Stop masses are excluded up to 250 GeV, with sensitivity only around $\Delta m \approx 0$ GeV. Two limits for the four-body decay are also shown in blue and red, with the strongest reach excluding up to around 300 GeV, but again limited to certain regions of Δm . Stop decay limits from the ATLAS experiment are shown in Figure 2.7b, with interpretations for both the charm (red) and four-body (purple) decay modes shown in the relevant $\Delta m < 80$ GeV region. Stop mass exclusion for the charm decay is slightly stronger than the CMS result, reaching up to around 275 GeV, while maintaining sensitivity across the Δm range. The limit for the four-body decay is constructed from two different analyses, with the 0-lepton analysis having a similar stop mass sensitivity, but again only at the smallest values of Δm . Conversely, the 1-lepton analysis gains sensitivity at higher Δm regions. It should be noted from these results that no single analysis maintains a good $m_{\tilde{t}}$ reach across the Δm range relevant for these two models.

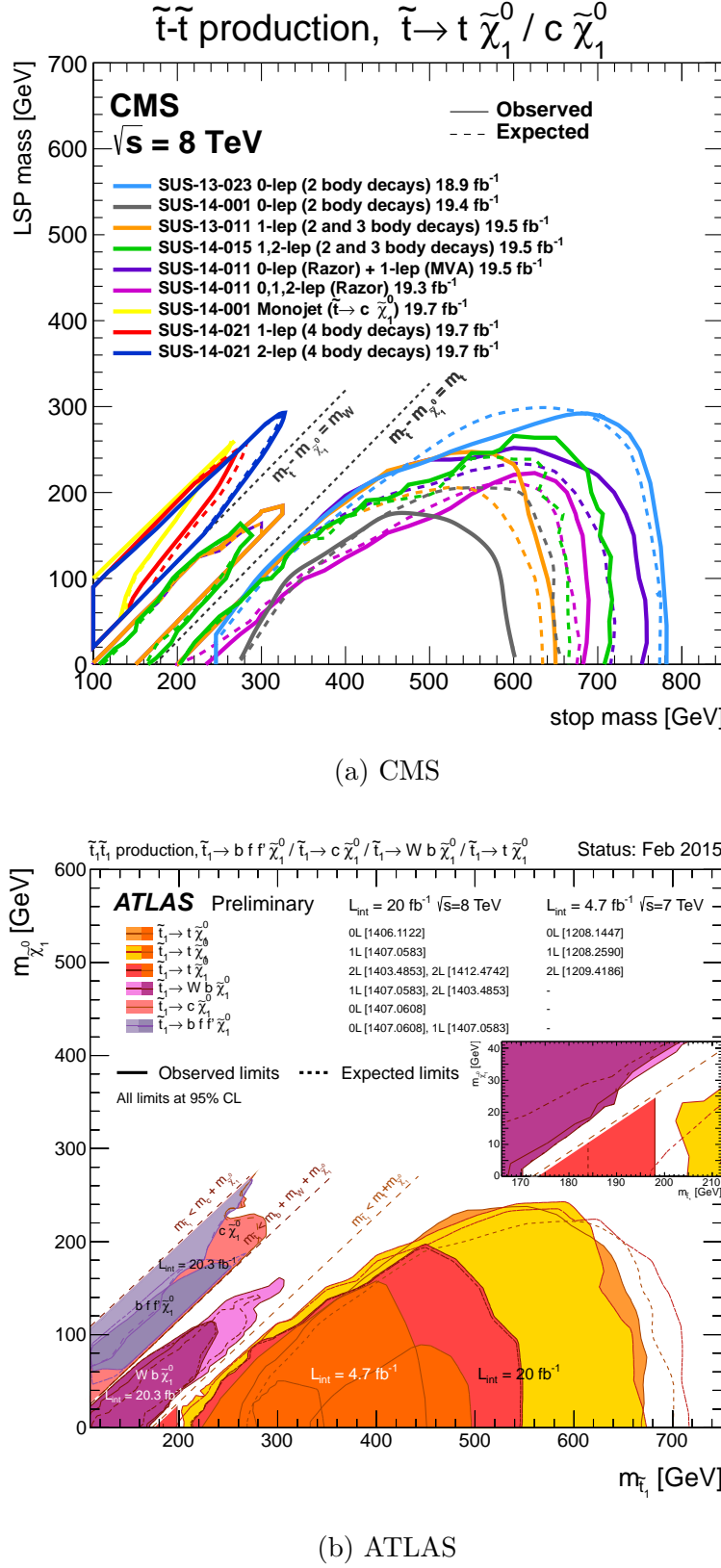


Fig. 2.7 Current limits on direct stop production from the CMS (2.7a)[45] and ATLAS (2.7b)[46] experiments as a function of the $m_{\tilde{t}}$ vs. $m_{\tilde{\chi}_1^0}$ mass plane. Charm decay limits are shown in yellow in 2.7a and red in 2.7b. The four-body decay mode is shown in dark-blue and red in 2.7a and purple in 2.7b.

CHAPTER 3

THE LHC AND THE CMS DETECTOR

3.1 The Large Hadron Collider

The Large Hadron Collider (LHC) is a 27 km circumference proton-proton synchrotron with maximum design centre of mass energy $\sqrt{s} = 14$ TeV, described in detail elsewhere [47]. It is the highest energy component of the CERN accelerator complex, shown in Figure 3.1. The LHC accelerates counter-rotating beams of protons using 400 MHz radio frequency (RF) cavities, focusses the beam using multiple quadrupole and higher order magnets, and maintains the beam trajectory using super-conducting, niobium-titanium dipole magnets, capable of producing an 8.4 T magnetic field. Such a high magnetic field is achieved by cooling the magnets to 1.9 K using super-fluid helium and applying a 11.85 kA electric current.

The beams, consisting of approximately up to 1380 bunches of $\mathcal{O}(10^{11})$ protons, are brought into collision at four points around the LHC ring within specialised detector systems, as shown in Figure 3.2. During the first run of the LHC, ‘Run I’, bunches were spaced in 50 ns intervals, giving a bunch crossing rate of 20 MHz. Collisions proceed for a number of hours, while collision rates are maintained by scanning the transverse beam positions, until such a time when proton numbers are depleted and the beam recycled so that the fill process can be repeated.

The rate of collisions at each interaction point is described by the instantaneous luminosity, given by the equation:

$$L_{inst.} = \frac{f_{orbit} n_B N_p^2}{A_{eff}}, \quad (3.1)$$

where f_{orbit} is the orbital frequency of bunches in the LHC, n_B is the number of

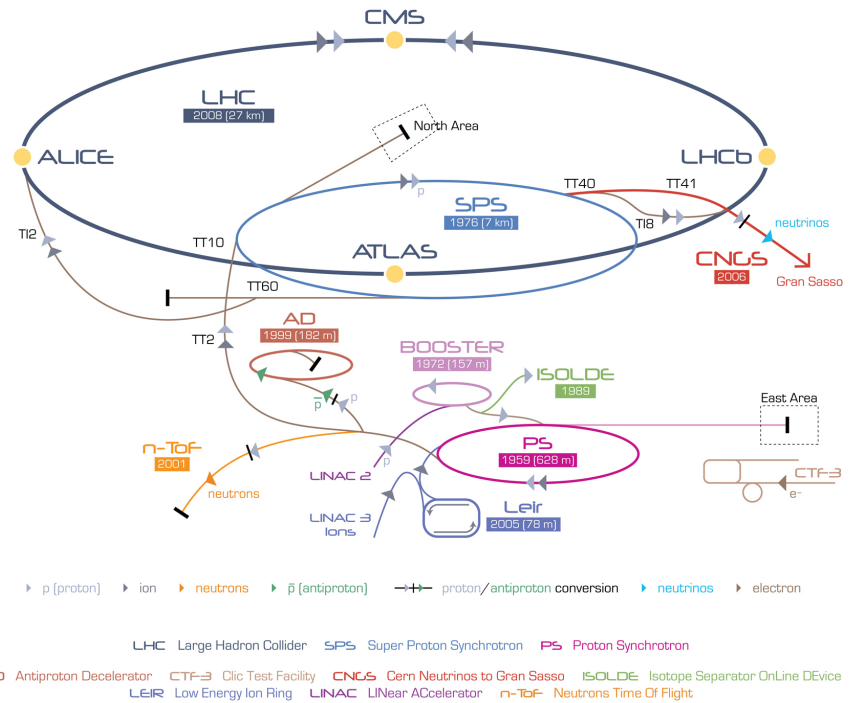


Fig. 3.1 Schematic diagram of the CERN accelerator complex, showing the various accelerators and storage rings, ultimately feeding the Large Hadron Collider [48].

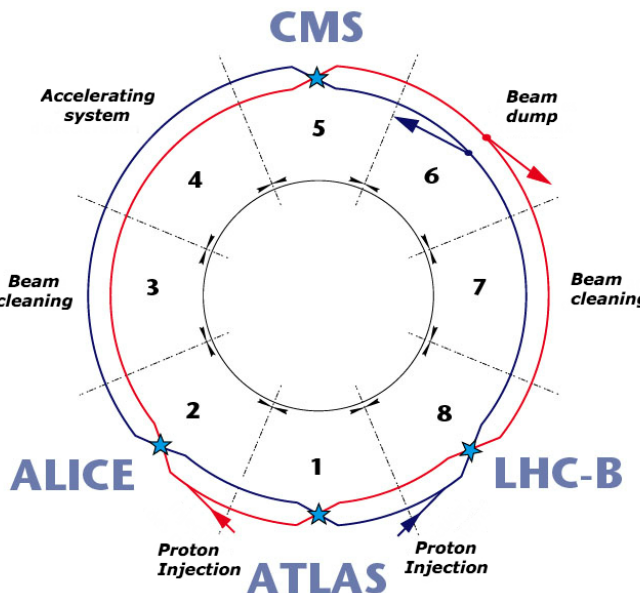


Fig. 3.2 Schematic diagram of the Large Hadron Collider, indicating the positions of the four collision points and their corresponding detector experiments [49].

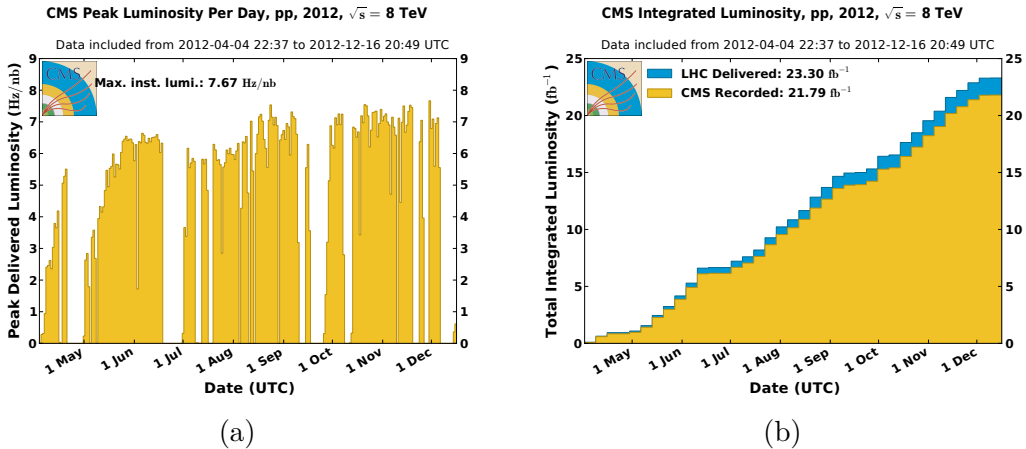


Fig. 3.3 The peak instantaneous luminosity for each day throughout 2012 (a), and the integrated luminosity delivered to and recorded at CMS (b) [50].

bunches in the machine, N_p is the number of protons per bunch, and A_{eff} is the effective overlap area between colliding bunches. The peak $L_{inst.}$ per day for CMS is shown in Figure 3.3a and the integral over time is shown in Figure 3.3, both for the full run period through 2012.

Simultaneous interactions happening at the time of each bunch crossing are referred to as in-time pile up (PU), as opposed to overlapping particle decays from previous bunch crossings called out-of-time pile up (PU). Both phenomena cause significant experimental challenges for detector readout and event reconstruction. The average Pileup distribution for Run I is shown in Figure 3.4.

3.2 Compact Muon Solenoid

The Compact Muon Solenoid (CMS), shown in Figure 3.5, is a hermetic detector system optimised for the study of high- p_T objects and their decays [51]. It is designed to make accurate measurements of the positions and momenta of physics objects such as electrons, muons, taus, photons and jets. Owing to an almost complete 4π solid angle coverage, CMS is capable of also making accurate measurements of global momentum imbalances due to the presence of weakly interacting particles.

The cylindrical detector is 28 m in length, 15 m in diameter and has a mass of around 14,000 tonnes. The z-axis is taken to be the longitudinal dimension along the beamline, the x-axis the perpendicular direction pointing towards the centre of the LHC ring, and the y-axis pointing skywards, perpendicular to these forming a right-

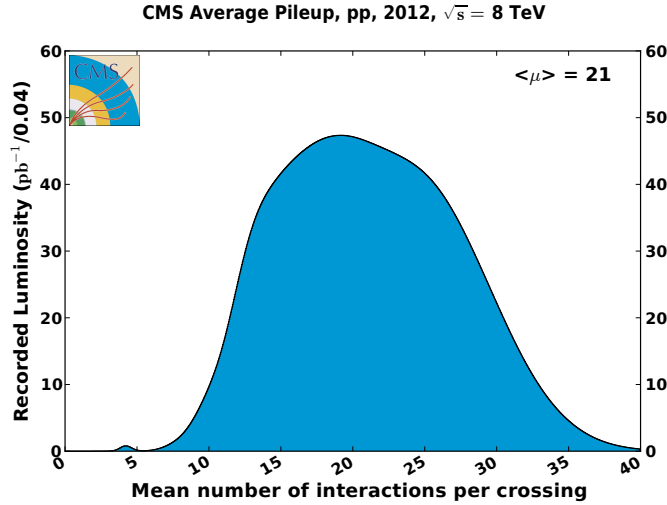


Fig. 3.4 The average in-time pileup distribution as seen by the CMS detector throughout Run I [50].

handed co-ordinate system. The transverse plane is taken to be the plane of the x and y axes.

Directions relative to the CMS detector are described with the variables ϕ , the angular direction in the transverse plane with range $[-\pi, \pi]$, and ‘pseudo-rapidity’, η , describing an angle with respect to the z-axis, defined as:

$$\eta = -\ln \tan \left(\frac{\theta}{2} \right), \quad (3.2)$$

where θ is the polar angle between the particle trajectory and the beam pipe in the y-z plane. Differences in these two variables, namely $\Delta\phi$ and $\Delta\eta$, are invariant under Lorentz boosts along the beamline in the massless limit, and so can be used to construct an angular separation between particles:

$$\Delta R = \sqrt{(\Delta\eta)^2 + (\Delta\phi)^2}. \quad (3.3)$$

CMS is arranged in a layered configuration of sub-detectors, structured as a cylindrical barrel, completed by two end-caps. The barrel contains a super-conducting solenoid magnet capable of producing a 3.8 T magnetic field. Operated at 4.5 K, with a 18.5 kA current, the longitudinal field produced bends the trajectories of charged particles allowing for precise charge and momenta measurements.

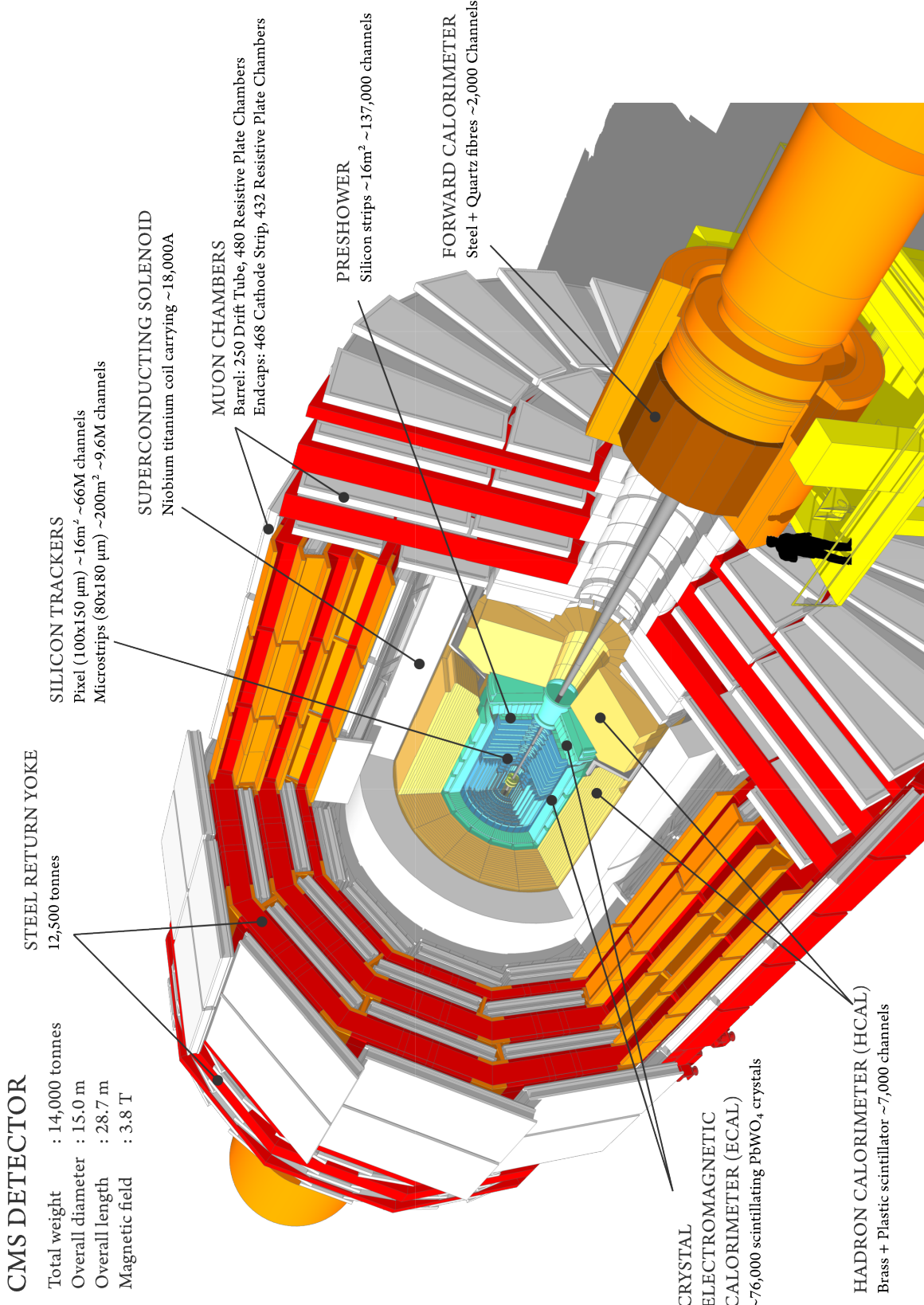


Fig. 3.5 Diagram of the Compact Muon Solenoid [52].

The following sections describe each of the detector subsystems in more detail.

3.2.1 Tracker

The silicon tracker system consists of pixel-based inner and microstrip-based outer detectors.

The pixel detector consists of three layers of silicon pixel sensors situated as close as 4 cm from the beamline, capable of producing 2D hit information of charged particles for use in vertex finding with a spatial resolution of $\sim 10\text{-}20 \mu\text{m}$. The barrel section is accompanied by two end-cap pixel detector disks. Each sensor contains a 52 x 80 grid of individual $100 \mu\text{m} \times 150 \mu\text{m}$ pixels, mounted to a lightweight mechanical substrate along with front-end readout electronics.

A further 10 layers of silicon microstrip detectors are used to accurately reconstruct the track path of charged particles. The sensors collectively cover an area of over 200 m^2 , are of p-in-n type, and range from $320 \mu\text{m}$ to $500 \mu\text{m}$ in thickness and pixel pitch ranging between $80 \mu\text{m}$ and $205 \mu\text{m}$, depending on distance from the beamline. The track path can be used to determine both the charge and momentum of charged particles, the latter with a $\Delta p_T/p_T$ resolution of $\sim 1\text{-}2\%$ for a 100 GeV particle.

All silicon detectors situated close to the interaction point receive high-doses of radiation, eventually ageing due to the damage inflicted. Consequently, radiation hard sensor and front-end electronics materials and designs have been selected to mitigate the effects of aging due to radiation damage.

3.2.2 Electromagnetic Calorimeter

The Electromagnetic Calorimeter (ECAL) system provides accurate measurements of energy deposits and the identification of electromagnetically interacting particles, and can also produce spatial measurements when used in conjunction with data from the tracker system. The detector consists of scintillating lead-tungstate (PbWO_4) crystals, each of dimension $0.017 \times 0.017 (\Delta\eta \times \Delta\phi)$ and 23 cm in length, corresponding to approximately 26 radiation lengths and providing a Molière radius of 2.2 cm. In both the barrel and the end-cap regions, individual crystals are clustered into super-towers, to match with towers in the trigger system (the calorimeter trigger system is described later in Section 3.2.5).

Scintillation light produced in each crystal is collected by either avalanche photodiodes in the barrel or vacuum photo-triodes in the endcap. The detectors are required

to be both radiation hard and capable of operating within the strong magnetic field environment of CMS.

The ECAL system is measured as having a $\Delta E/E$ resolution for a 100 GeV particle of $\sim 0.5\%$, exceeding its technical design requirements.

3.2.3 Hadronic Calorimeter

The Hadronic Calorimeter (HCAL) system measures the energy of hadronic showers originating from single-quarks and gluons (i.e. jets). It is constructed from layers of alternating brass absorber and plastic scintillator, of which there are 17 in the barrel and 19 in the endcaps. The latter are spatially divided into towers measuring 0.087×0.087 in the barrel and end-caps. Hadronic particle showers deposit energy as scintillation light in the plastic layers, which is transmitted via wavelength shifting fibres to be measured in hybrid photo-diodes. The energy resolution of the HCAL system is calculated with respect to π -meson energy reconstruction, and is measured to be $\sim 90\%/\sqrt{E}$ GeV $^{-0.5}$ in the barrel, and $\sim 100\%/\sqrt{E}$ GeV $^{-0.5}$ in the endcap.

3.2.4 Muon Systems

The muon system provides identification and precision measurements of muon position and momenta. Energy deposits in the muon systems can be combined with corresponding information from the tracker to improve momentum resolution significantly. The system is designed to have a momentum resolution, $\Delta p_T/p_T$, of $\sim 10\%$ on its own, and $\sim 2\%$ when combined with tracker information, both measured for muons with $p_T < 100$ GeV.

Muons are detected in the outer layers of CMS, with the muon system comprised of three different gaseous detector technologies each with different pseudo-rapidity coverage, as shown in Figure 3.6. The central barrel region, $|\eta| < 1.2$, is equipped with Drift Tube (DT) detectors - a traditional detector technology, optimised for low-occupancy measurements. Cathode Strip Chambers (CSC) cover the forward region, $0.9 < |\eta| < 2.4$, and dual-layered Resistive Plate Chambers (RPC) cover $|\eta| < 2.1$ - both CSC and RPC detectors being optimised for operation in the presence of both high magnetic field and neutron background environments.

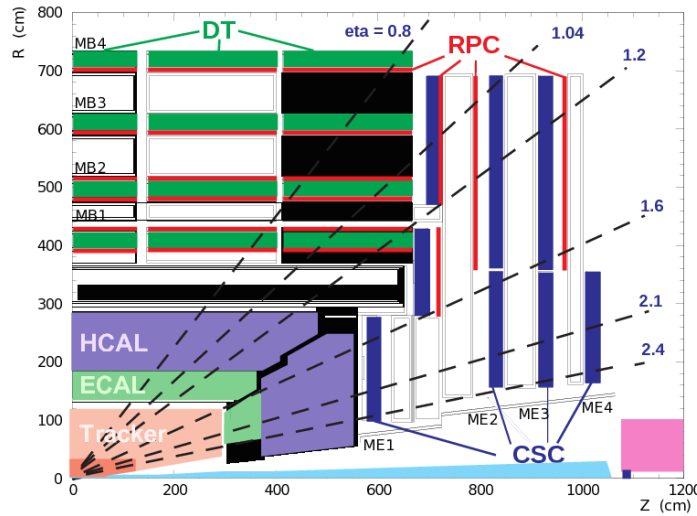


Fig. 3.6 Cross section of the CMS detector in the y - z plane, showing the three muon systems (DT, RPC and CSC) as well as other interior sub-detector systems [53].

3.2.5 Trigger

Events of interest are selected using a dedicated triggering system [54], divided into two distinct stages: the hardware-based Level-1 Trigger (L1) and the software-based High-Level Trigger (HLT).

Level-1 Trigger

The L1 system consists of a staged, modular design of custom built hardware electronics subsystems, as shown in Figure 3.7. The L1 trigger reconstructs energy deposits in the calorimeter and muon systems into coarse ‘trigger-primitive’ physics objects. Regional information is gathered by separate modules before being combined in the Global Calorimeter Trigger (GCT) and Global Muon Trigger (GMT) systems, where physics objects are sorted according to energy. Finally, event objects are passed on to the Global Trigger (GT) where a ‘Level-1 Accept’ (L1A) signal is issued or not, dependent on the event meeting one of up to 128 simple object threshold and multiplicity based requirements.

The L1 system is required to run at 40 MHz, equal to the maximal bunch-crossing rate within CMS, with a L1A decision required within a latency of $3\ \mu\text{s}$. The maximum available output bandwidth of the L1 system is 100 kHz, but typically is maintained at a lower value to allow for stochastic fluctuations in rate.

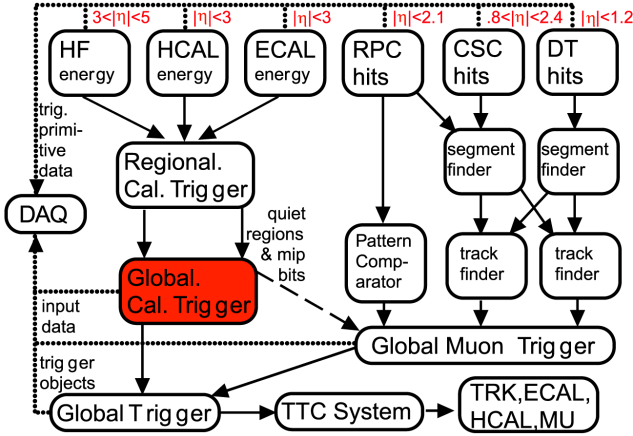


Fig. 3.7 Schematic overview of the Level-1 hardware trigger system of CMS. η coverage is shown in red text and the data-flow indicated by arrow direction [54].

High-level Trigger

Following a L1A signal, candidate events are optically transmitted to the HLT system, consisting of a large computer farm of server PCs. Due to the increase in available processing time of up to 50 ms, events can be reconstructed in greater detail allowing for a closer emulation of offline reconstruction techniques. Complex analyst-designed trigger rules are used, which can employ more sophisticated event-level variables such as α_T (described in detail later in Chapter 6).

The HLT reduces the event rate further by around two orders of magnitude, producing an output event rate of up to 1 kHz. Events passing the HLT are transmitted to the Grid computing system [55] for full offline reconstruction.

CHAPTER 4

OBJECT DEFINITIONS

Physics objects are observed as energy deposits in the various detector subsystems throughout CMS. Specific definitions for the different objects used in this analysis are provided by the Physics Object Groups (*POG*'s) and are described in the following sections.

4.1 Jets

Jets are produced through the hadronisation and showering of a single quark or gluon through the calorimeter systems. Energy deposits are clustered using the anti- k_T algorithm [56] with an $R = 0.5$ cone size parameter. Jets are reconstructed from calorimeter information and are widely known as ‘Calojets’. While many analyses use ‘Particle Flow’ (PF) techniques to reconstruct ‘PFJets’ - jets constructed using information from combinations of multiple sub-detector systems - this analysis continues to use ‘Calojets’ for compatibility with our well studied, Calojet-based signal triggers. Table 4.1 summarises the ID requirements used in this analysis, which correspond to the “Loose” working point [57]. Raw energy measurements that form jets have the following sequential corrections [58, 59] applied:

- L1** To remove energy originating from PU events, therefore removing any dependence on luminosity across a dataset [60, 61].
- L2** To ensure a uniform energy response in η across the calorimeter [62].
- L3** To ensure a uniform response according to the p_T of the deposit [62].
- L2L3** Final, additional corrections to bring data and MC into agreement.

Table 4.1 Criteria for the “loose” jet identification working point.

Requirement	Description
$f_{HPD} < 0.98$	Fractional contribution from the “hottest” Hybrid Photo Diode.
$f_{EM} > 0.01$	Minimum electromagnetic fractional component.
$N_{\text{hits}}^{90} \geq 2$	Number of HCAL channels containing at least 90% of total energy.

4.1.1 Identification jets from b quarks

Jets originating from b quarks can be identified using information from the vertex detector due to their increased lifetime with respect to gluons, light flavour quarks (u, d, s) or charm quarks. B tagging algorithms are designed to determine the probability that a jet originates from a b quark, given, amongst other properties, the track displacement from the primary vertex (PV). Each algorithm calculates a value used to discriminate between a jet originating from a b quark or other sources.

The Combined Secondary Vertex (CSV) algorithm [63] is used in this analysis. The distribution of discriminator values is shown in Figure 4.1a. The “Medium” working point corresponds to a discriminator threshold of > 0.679 , and is used in this analysis. This working point corresponds to a mistag rate for gluons/light-quarks of 1%, and a p_T dependent efficiency in the range of 60-70%, as shown in Figure 4.1b. Also shown in Figure 4.1b are the MC scale factors, SF_b , defined as the ratio of the CSV b tagging algorithm efficiency in data and MC, to be applied to MC samples.

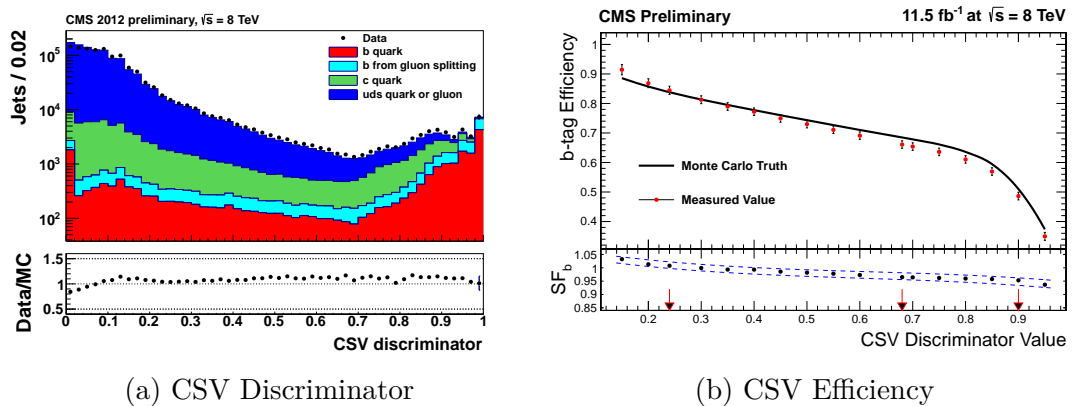


Fig. 4.1 The Combined Secondary Vertex b tagging algorithm discriminator distribution (left) and the b tagging efficiency (right) as measured in both data and simulation. MC scale factors are shown in the lower plot of 4.1b [64].

4.2 Muons

Muons are identified from energy deposits predominantly in the muon systems and the tracker using the muon *POG*'s Tight working point definition [65], as summarised in Table 4.2. This definition is used in both the muon selection in the μ +jets and $\mu\mu$ +jets control regions, and the muon veto in the hadronic signal region.

Table 4.2 Muon identification (Tight working point).

Variable	Requirement	Description
Global Muon	True	Muon object is reconstructed from both hits in the muon systems and matched hits in the silicon tracker
PFMuon	True	Muon object reconstructed with multiple subsystems using Particle Flow techniques
$\chi^2/ndof$ of fit	< 10	Goodness of fit of the global muon track fit. Suppresses hadronic punch-through and muons decaying in flight.
Muon chamber hits	> 0	At least 1 hit in a muon chamber. Suppresses hadronic punch-through and muons decaying in flight.
Muon station hits	> 1	Muon hits in at least 2 muon stations. Suppresses punch-through and accidental track-to-segment matches. Also makes consistent with trigger muon requirements.
Transverse impact d_{xy}	< 0.2 mm	Tracker track is close to Primary Vertex in the x-y plane. Helps suppress cosmic ray muons and muons from decays in flight.
Longitudinal distance d_z	< 0.5 mm	Tracker track is close to Primary Vertex in z-direction. Suppresses muons from cosmic rays, decays in flight and PU.
Pixel hits	> 0	At least 1 pixel hit. Suppresses muons from decays in flight.
Track layer hits	> 5	Guarantees good p_T measurement.
PF Isolation (PU corrected)	< 0.12	Particle Flow based isolation, based on a cone size of $\Delta R < 0.4$, with “ $\Delta\beta$ ” PU corrections applied.

4.3 Photons

Photon definitions are made relative to their position in the ECAL, either in the barrel or the endcap, as summarised in Table 4.3. This Tight working point ID is defined by the *POG* group [66] and used for both the photon selection in the γ +jets control region and as a veto in the hadronic signal region.

4.4 Electrons

The Electron *POG*'s Loose working point ID [67] is used in this analysis to veto electrons from all areas of the analysis. This cut based identification is defined separately for the barrel and endcap regions of the detector, uses information from the calorimeter systems as well as the tracker, and is summarised in Table 4.4. The final two

Table 4.3 Photon identification (Tight working point).

Categories	Barrel	Endcap	Description
Single Tower H/E	< 0.05	< 0.05	Ratio of energy deposited in the HCAL towers within $\Delta R < 0.15$ of the ECAL supercluster, and the ECAL supercluster itself.
$\sigma_{in\eta}$	< 0.11	< 0.31	The cluster shape covariance of the ECAL supercluster in the η dimension.
PF charged hadron isolation	< 0.70	< 0.50	PF-based isolation requirements to ensure no hadronic or electromagnetic activity with a cone defined by $\Delta R < 0.3$. The isolation is corrected for PU effects.
PF neutral hadron isolation	$< 0.4 + 0.04 \times p_T^\gamma$	$< 1.5 + 0.04 \times p_T^\gamma$	
PF photon isolation	$< 0.5 + 0.005 \times p_T^\gamma$	$< 1.0 + 0.005 \times p_T^\gamma$	

Table 4.4 Electron identification (Loose working point).

Categories	Barrel	Endcap	Description
$\Delta\eta_{In}$	< 0.007	< 0.009	The difference between the track and ECAL supercluster in the η dimension.
$\Delta\phi_{In}$	< 0.15	< 0.10	The difference between the track and ECAL supercluster in the ϕ dimension.
$\sigma_{in\eta}$	< 0.01	< 0.03	The cluster shape covariance of the ECAL supercluster in the η dimension.
H/E	< 0.12	< 0.10	Ratio of energy deposited in the HCAL towers within $\Delta R < 0.15$ of the ECAL supercluster and the ECAL supercluster itself.
d0 (vtx)	< 0.02	< 0.02	The transverse distance of the track from the PV.
dZ (vtx)	< 0.2	< 0.20	The longitudinal distance of the track from the PV.
$ (1/E_{ECAL} - 1/p_{trk}) $	< 0.05	< 0.05	Comparison of the ECAL supercluster energy and the track p_T , to suppress low p_T fakes.
PF relative isolation	< 0.15	< 0.15	PF based isolation calculated from particle activity within a cone of $\Delta R < 0.3$.
Vertex fit probability	10^{-6}	10^{-6}	Probability of fit to potential conversion tracks.
Missing hits	≤ 1	≤ 1	Number of missing tracker hits due to possible conversion.

requirements are specifically for the rejection of electrons originating from photons converted into e^-e^+ pairs.

4.5 Energy Sums

Physics objects are combined in the form of kinematic variables known as energy sums. The definitions of the energy sum variables are:

$$\begin{aligned} E_T &= \sum_i |\vec{p}_T|, \\ \cancel{E}_T &= -\left| \sum_i \vec{p}_T \right|, \\ H_T &= \sum_i^{\text{jets}} |\vec{p}_T|, \\ \cancel{H}_T &= -\sum_i^{\text{jets}} \vec{p}_T, \\ \cancel{H}_T &= -\left| \sum_i^{\text{jets}} \vec{p}_T \right|; \end{aligned} \quad (4.1)$$

namely the total transverse energy, total missing transverse energy ('MET'), total transverse hadronic energy, total missing transverse hadronic energy vector and total missing transverse hadronic energy ('MHT'). These are calculated on the fly in the analysis using identified objects, with the exception of \cancel{E}_T which is constructed from PF candidates and subject to type-I corrections (jets used for \cancel{E}_T calculation are subject to prescribed Jet Energy Corrections themselves). A full set of \cancel{E}_T filters are defined by the MET *POG* as summarised in Table 4.5. The filters account for various physics and detector effects which can give un-physical or spurious \cancel{E}_T signals.

The \cancel{E}_T variable only appears in the analysis in the calculation of the transverse mass of the lepton system in the $\mu+\text{jets}$ control region (Section 7.2.1) and in the $\cancel{H}_T/\cancel{E}_T$ variable (Section 7.4.1) as an independent estimator of the event's missing energy.

4.6 Single Isolated Tracks

Single Isolated Tracks are used to identify hadronically decaying τ leptons and leptonically decaying W bosons where the corresponding lepton has failed the identification

Table 4.5 \cancel{E}_T filters employed in the analysis, as recommended by the MET POG.

Filter Name	Description
Beam Halo CSC ID	Beam interactions with residual gases in the beam pipe or with mechanical apertures, causing secondary particle production. Events are vetoed if an event contains a positive beam halo ID from the CSC detectors.
HBHE Noise	Noise originating from instrumentation issues with the HCAL’s Hybrid Photo Diodes (HPDs) or the Readout Boxes (RBXs). Events are vetoed if they contain isolated clusters of noisy cells in either the barrel or endcap.
Tracking Failure	Significant energy deposits in the calorimeter systems with no corresponding tracks due to tracker algorithm failure. Events are vetoed if the summed p_T of all tracks in the event is equal to less than 10% of the H_T .
HCAL Laser Misfire	Calibration lasers being accidentally fired through the HCAL during bunch crossings (as opposed to abort gaps). Events are removed that contain such accidental laser firings.
DeadECAL Cell TP	Dead or damaged ECAL crystals which cannot read out energy deposits correctly. Trigger primitives are checked to determine how much energy was lost, and events are appropriately masked.

criteria for whatever reason. Summarised in Table 4.6, the selection is based on PF candidates. This ID is used as a veto in all selections, with the selected ‘tag’ lepton ignored in the μ +jets and $\mu\mu$ +jets control selections. The ID definition is taken from [68].

Table 4.6 Single Isolated Track identification.

Variable	Requirement	Description
Charge	$\neq 0$	Candidate is charged.
Track p_T	$> 10 \text{ GeV}$	Track transverse momentum.
$\Delta z(\text{track}, \text{PV})$	$< 0.05 \text{ cm}$	Longitudinal distance of track from primary vertex.
Relative Track Isolation	< 0.1	Isolation relative to other PF candidate tracks in cone of $\Delta R < 0.3$.

CHAPTER 5

DATASETS AND MONTECARLO SAMPLES

5.1 Datasets

The datasets used in this analysis are listed in Table 5.1, each containing events from a specific trigger of interest. The primary signal samples are named ‘HTMHTParked’, spanning over the 2012 run periods B, C and D, with a total combined integrated luminosity of 18.49 fb^{-1} . Control samples used for predictions of SM backgrounds include ‘JetHT’, ‘SingleMu’ and ‘SinglePhoton’, covering run periods A, B, C and D, with combined integrated luminosities of 18.48 fb^{-1} , 19.13 fb^{-1} and 19.12 fb^{-1} , respectively.

Table 5.1 8 TeV Datasets with the integrated luminosity for each.

Dataset	Luminosity (fb^{-1})
/HTMHTParked/Run2012B-22Jan2013-v1/AOD	4.41
/HTMHTParked/Run2012C-22Jan2013-v1/AOD	6.80
/HTMHTParked/Run2012D-22Jan2013-v1/AOD	7.29
Total	18.49
/JetHT/Run2012B-22Jan2013-v1/AOD	4.39
/JetHT/Run2012C-22Jan2013-v1/AOD	6.80
/JetHT/Run2012D-22Jan2013-v1/AOD	7.29
Total	18.48
/SingleMu/Run2012A-22Jan2013-v1/AOD	0.69
/SingleMu/Run2012B-22Jan2013-v1/AOD	4.40
/SingleMu/Run2012C-22Jan2013-v1/AOD	6.77
/SingleMu/Run2012D-22Jan2013-v1/AOD	7.27
Total	19.13
/Photon/Run2012A-22Jan2013-v1/AOD	0.68
/SinglePhoton/Run2012B-22Jan2013-v1/AOD	4.40
/SinglePhoton/Run2012C-22Jan2013-v1/AOD	6.77
/SinglePhotonParked/Run2012D-22Jan2013-v1/AOD	7.27
Total	19.12

5.2 MonteCarlo Background and Signal samples

The full set of simulated MonteCarlo (MC) samples used in this analysis are listed in Table 5.2 along with the number of events, next-to-next-to-leading order (NNLO) cross section and an effective integrated luminosity for each. These samples contain simulated events of relevant sources of SM backgrounds, specifically $t\bar{t}$, photon, W boson and Z boson production, each with associated jets, as well as dedicated samples of QCD production.

The Parton Density Function (PDF) of colliding protons are modelled according to the CTEQ6L1 distribution [69], the matrix-element level hard-scatter performed by MADGRAPH5 [70], POWHEG1 [71] or PYTHIA6 [72], with outgoing partons showered in PYTHIA6. The produced generator level particles are then input into a full detector simulation in GEANT4 [73], and detector hits ‘digitized’ in order to simulate the response of detector electronics. Prior to digitization, a number of ‘MinimumBias’ events are overlayed in order to reproduce LHC run conditions. Event-level weights are applied to each simulated sample such that both the PU and equivalent integrated luminosity are matched to a given data sample.

Additional corrections are made to simulated event samples in order to correct the efficiency of b tagging algorithms to match that observed in data. Corrections are determined as a function of jet-flavour (light/c/b), defined as:

$$SF_{light,c,b} = \frac{\epsilon_{light,c,b}^{data}(p_T, \eta)}{\epsilon_{light,c,b}^{MC}(p_T, \eta)}, \quad (5.1)$$

where $\epsilon_{light,c,b}^{data}$ and $\epsilon_{light,c,b}^{MC}$ represent p_T and η dependent b tagging efficiencies measured in data and MC respectively. These are calculated and provided centrally by the BTAG POG [74].

Table 5.2 MC samples for Standard Model processes with their NNLO cross sections and equivalent integrated luminosity.

Sample	N _{event}	Cross section (pb)	Corrected Cross section (pb)	Luminosity (fb ⁻¹)
/N_jetStolNu_TuneZ2star_8TeV-madgraph-tarball/Summer12_DR53X-PU_S10_START53_V7A-v1/ADDSIM	57661905	37509.0	34133.2	1.5
/N_jetStolNu_HF-15_0106200_8TeV-madgraph/Summer12_DR53X-PU_S10_START53_V7C-v1/ADDSIM	21414209	253.8	234.53	84.4
/N_jetStolNu_HF-20_0106200_8TeV-madgraph/Summer12_DR53X-PU_S10_START53_V7C-v1/ADDSIM	9895771	116.5	103.94	84.9
/N_jetStolNu_HF-25_0106200_8TeV-madgraph_v2/Summer12_DR53X-PU_S10_START53_V7A-v1/ADDSIM	4924990	57.6	51.34	85.5
/N_jetStolNu_HF-30_0106200_8TeV-madgraph_v2/Summer12_DR53X-PU_S10_START53_V7A-v1/ADDSIM	5141023	48.4	42.41	106.2
/N_jetStolNu_HF-40_0106200_8TeV-madgraph_v2/Summer12_DR53X-PU_S10_START53_V7A-v1/ADDSIM	4923847	30.8	26.36	159.9
/Z_jetStolNu_50_HF_100_TuneZ2star_8TeV-madgraph_(ext)/Summer12_DR53X-PU_S10_START53_V7A-v1/ADDSIM	23743998	452.8	405.21	52.4
/Z_jetStolNu_100_HF_200_TuneZ2star_8TeV-madgraph_(ext)/Summer12_DR53X-PU_S10_START53_V7A-v1/ADDSIM	9876059	190.4	173.76	51.9
/Z_jetStolNu_200_HF_400_TuneZ2star_8TeV-madgraph_(ext)/Summer12_DR53X-PU_S10_START53_V7A-v1/ADDSIM	9649619	45.1	42.41	214.0
/Z_jetStolNu_400_HF_800_TuneZ2star_8TeV-madgraph_(ext)/Summer12_DR53X-PU_S10_START53_V7A-v1/ADDSIM	5079710	6.26	5.81	811.5
/TT_C10_TuneZ2star_8TeV-powheg_tauola/Summer12_DR53X-PU_S10_START53_V7A-v1/(v2)/ADDSIM	27094723	234.0	271.44	115.8
/TT_C10_TuneZ2star_8TeV-powheg_tauola/Summer12_DR53X-PU_S10_START53_V7A-v1/(v2)/ADDSIM	210160	0.172	0.172	1221.9
/TTWJJets_8TeV-madgraph_v2/Summer12_DR53X-PU_S10_START53_V7A-v1/ADDSIM	182327	0.2149	0.2149	848.4
/TTWJJets_8TeV-madgraph/Summer12_DR53X-PU_S10_START53_V7A-v1/ADDSIM	3710227	56.4	56.4	65.8
/T_t-channel_TuneZ2star_8TeV-powheg_tauola/Summer12_DR53X-PU_S10_START53_V7A-v1/ADDSIM	1935072	30.7	30.7	63.0
/T_s-channel_TuneZ2star_8TeV-powheg_tauola/Summer12_DR53X-PU_S10_START53_V7A-v1/ADDSIM	243961	3.79	3.79	64.4
/Tbar_s-channel_TuneZ2star_8TeV-powheg_tauola/Summer12_DR53X-PU_S10_START53_V7A-v1/ADDSIM	139874	1.76	1.76	79.5
/T_tW-channel_Dr_TuneZ2star_8TeV-powheg_tauola/Summer12_DR53X-PU_S10_START53_V7A-v1/ADDSIM	497658	11.1	11.1	44.8
/Tbar_tW-channel_Dr_TuneZ2star_8TeV-powheg_tauola/Summer12_DR53X-PU_S10_START53_V7A-v1/ADDSIM	493460	11.1	11.1	44.5
/D3Vjets_Toll_M-10_010600filter_8TeV-madgraph/Summer12_DR53X-PU_S10_START53_V7A-v1/ADDSIM	7116223	13124.1	12025.4	0.5
/D3Vjets_Toll_M-50_010600filter_8TeV-madgraph/Summer12_DR53X-PU_S10_START53_V7A-v1/ADDSIM	30171503	3503.7	3288.45	8.6
/D3Vjets_Toll_HF-200_010600_TuneZ2star_8TeV-madgraph-tarball/Summer12_DR53X-PU_S10_START53_V7A-v1/ADDSIM	6892777	24.3	22.24	283.7
/D3Vjets_Toll_HF-400_010600_TuneZ2star_8TeV-madgraph-tarball/Summer12_DR53X-PU_S10_START53_V7A-v1/ADDSIM	2695789	3.36	3.11	802.3
/GJets_HF-200To100_8TeV-madgraph/Summer12_DR53X-PU_S10_START53_V7A-v1/ADDSIM	57891147	1140.8	1060.9	50.7
/GJets_HF-400To100_8TeV-madgraph/Summer12_DR53X-PU_S10_START53_V7A-v1/ADDSIM	945962	124.7	115.97	75.9
/W_W_TuneZ2star_8TeV-powheg_tauola/Summer12_DR53X-PU_S10_START53_V7A-v1/ADDSIM	9884831	57.1	57.1	173.2
/WZ_TuneZ2star_8TeV_pythia6_tauola/Summer12_DR53X-PU_S10_START53_V7A-v1/ADDSIM	9841248	12.6	12.6	781.1
/ZZ_TuneZ2star_8TeV_pythia6_tauola/Summer12_DR53X-PU_S10_START53_V7A-v1/ADDSIM	9751908	8.26	8.26	1180.6
/QCD_Pt-50to80_Pt-300to470_TuneZ2star_8TeV_pythia6/Summer12_DR53X-PU_S10_START53_V7A-v1/ADDSIM	5950860	8148778 (LO)	8148778 (LO)	0.001
/QCD_Pt-600to800_Pt-470to600_TuneZ2star_8TeV_pythia6/Summer12_DR53X-PU_S10_START53_V7A-v2	5962864	1033680 (LO)	1033680 (LO)	0.0006
/QCD_Pt-800to1000_TuneZ2star_8TeV_pythia6/Summer12_DR53X-PU_S10_START53_V7A-v3	598532	156293 (LO)	156293 (LO)	0.038
/QCD_Pt-120to170_TuneZ2star_8TeV_pythia6/Summer12_DR53X-PU_S10_START53_V7A-v3	20155180	34138 (LO)	34138 (LO)	0.590
/QCD_Pt-170to230_TuneZ2star_8TeV_pythia6/Summer12_DR53X-PU_S10_START53_V7A-v1 (v2)	23588100	1759.5 (LO)	1759.5 (LO)	13.4
/QCD_Pt-300to470_TuneZ2star_8TeV_pythia6/Summer12_DR53X-PU_S10_START53_V7A-v1 (v2)	3978848	113.9 (LO)	113.9 (LO)	34.9
/QCD_Pt-470to600_TuneZ2star_8TeV_pythia6/Summer12_DR53X-PU_S10_START53_V7A-v2	3964864	27.0 (LO)	27.0 (LO)	146.8
/QCD_Pt-600to800_TuneZ2star_8TeV_pythia6/Summer12_DR53X-PU_S10_START53_V7A-v2	3854563	3.55 (LO)	3.55 (LO)	1085.8
/QCD_Pt-800to1000_TuneZ2star_8TeV_pythia6/Summer12_DR53X-PU_S10_START53_V7A-v2	1964088	0.738 (LO)	0.738 (LO)	2661.4
/QCD_Pt-1400to1800_TuneZ2star_8TeV_pythia6/Summer12_DR53X-PU_S10_START53_V7A-v1	1988062	0.0335 (LO)	0.0335 (LO)	59345.4
/QCD_Pt-1800_TuneZ2star_8TeV_pythia6/Summer12_DR53X-PU_S10_START53_V7A-v1	977586	0.00183 (LO)	0.00183 (LO)	534200
/QCD_HF-250To600_TuneZ2star_8TeV-madgraph_pythia6/Summer12_DR53X-PU_S10_START53_V7A-v1/ADDSIM	50081518	1.036E7 (LO)	1.036E7 (LO)	0.005
/QCD_HF-500To1000_TuneZ2star_8TeV-madgraph_pythia6/Summer12_DR53X-PU_S10_START53_V7A-v1/ADDSIM	27602078	276000 (LO)	276000 (LO)	0.1
/QCD_HF-1000To1400_TuneZ2star_8TeV-madgraph_pythia6/Summer12_DR53X-PU_S10_START53_V7A-v1/ADDSIM	27613225	8426 (LO)	8426 (LO)	3.3
/QCD_HF-1400To1800_TuneZ2star_8TeV-madgraph_pythia6/Summer12_DR53X-PU_S10_START53_V7A-v1/ADDSIM	12018415	204 (LO)	204 (LO)	58.9

Interpretations are made using signal MC samples, each representing a scan in the phase space of a specific SMS model. These samples are listed in Table 5.3. Each sample is generated at the parton level using **MADGRAPH5** and then decayed using **PYTHIA6**. Diagrams for up to two additional partons are simulated in the initial generation step to ensure good modelling of initial state radiation (ISR), however supplementary samples were produced with up to three additional partons to allow for systematic studies into the effect on analysis acceptance, as detailed in Chapter 9.

Signal MC samples use the **FASTSIM** detector simulation framework [75] in order to simulate detector and electronics responses. In comparison to the **FULLSIM** method used for all other MC backgrounds, **FASTSIM** aims to greatly reduce the processing time required to generate samples by avoiding the CPU-intensive full detector simulation of the **GEANT** framework, instead employing detector response parametrisations tuned using **FULLSIM** samples.

Table 5.3 MC samples for Simplified Model Spectra.

Model	Sample	Description
Charm decay	/SMS-MadGraph_2J_T2cc_NoFilter_msStop=100to250_mlSP=20to230_V9_FSM-v1/AODSIM	Original scan
Charm decay	/SMS-T2cc_NoFilter_msStop=175to250_mlSP=95to240_8TeV-Pythia6Z_star/Summer12-START53_V9_FSM-v1/AODSIM	Original scan
Charm decay	/SMS-T2cc_2J_msStop=250to350_mlSP=195to6340_Tune22star_8TeV-madgraph-tauola/Summer12-START53_V19_FSM-v2/AODSIM	Scan extension
Charm decay	/SMS-SmeV_PythiaZ_T2cc_3jets_msStop=200_mlSP=120_Summer12-START52_19_FSM-v1/AODSIM	3-parton sample
Charm decay	/SMS-SmeV_PythiaZ_T2cc_3jets_msStop=200_mlSP=190_Summer12-START52_19_FSM-v1/AODSIM	3-parton sample
Four-body decay	/SMS-T2Dgenerator@Stop_2J_msStop=100to150_mlSP=20to140_Tune22star_8TeV-madgraph-tauola/Summer12-START53_V19_FSM-v1/AODSIM	Original scan
Four-body decay	/SMS-T2Dgenerator@Stop_2J_msStop=175to225_mlSP=95to215_Tune22star_8TeV-madgraph-tauola/Summer12-START53_V19_FSM-v1/AODSIM	Original scan
Four-body decay	/SMS-T2Dgenerator@Stop_2J_msStop=250to300_mlSP=170to280_Tune22star_8TeV-madgraph-tauola/Summer12-START53_V19_FSM-v1/AODSIM	Original scan
Four-body decay	/SMS-T2Dgenerator@Stop_2J_msStop=325to375_mlSP=245to365_Tune22star_8TeV-madgraph-tauola/Summer12-START53_V19_FSM-v1/AODSIM	Original scan
Four-body decay	/SMS-T2Dgenerator@Stop_2J_msStop=400_mlSP=320to390_Tune22star_8TeV-madgraph-tauola/Summer12-START53_V19_FSM-v1/AODSIM	Original scan

5.3 Correcting SM sample cross sections

5.3.1 H_T^{parton} binned samples

Given the computing resources required to produce MC samples, statistics can be greatly increased by only simulating events within some kinematic range. This analysis therefore makes use of MC samples binned according to parton-level H_T (H_T^{parton} - the scalar sum of transverse energies of the quarks and gluons involved in the hard scatter process). The binned samples correspond to the processes $W + \text{jets}$, $Z(\nu\nu) + \text{jets}$ and $DY + \text{jets}$. Leading order (LO) cross-sections are provided with these samples, which are translated into next-to-next-to-leading order (NNLO) cross-sections using scaling-factors (k-factors) derived from corresponding inclusive sample cross-sections (where $k = \sigma_{NNLO}/\sigma_{LO}$). However, recent CMS studies [76] have shown that the provided LO cross-sections for H_T^{parton} binned samples can be incorrect by up to 10%. To ensure H_T^{parton} binned samples are fully consistent with their corresponding inclusive samples, the following procedure is used:

1. Calculate the σ_{NNLO} for each H_T^{parton} binned sample using k-factors derived from inclusive samples. In the case of $Z(\nu\nu) + \text{jets}$ where no such inclusive sample exists, k-factors are taken from the $DY + \text{jets}$ sample.
2. Compare the distribution of H_T^{parton} between the binned and inclusive samples. Again, $Z(\nu\nu) + \text{jets}$ binned is compared to $DY + \text{jets}$ inclusive.
3. Derive corrections to σ_{NNLO} for each H_T^{parton} sample such that the ratio between the H_T^{parton} distributions is 1.0, or in the case of $Z(\nu\nu) + \text{jets}$ vs. $DY + \text{jets}$, the ratio of the PDG measured cross-sections, 0.505 [8].

Example H_T^{parton} distributions before and after this procedure are shown in Figure 5.1, where steps are clearly visible in the ratio prior to the corrections, and then removed following corrections.

5.3.2 H_T sideband normalisation

As mentioned in Section 5.3, absolute MC normalisation is not well modelled in the high- \cancel{E}_T region of phase-space in which many SUSY analyses search. As such, data and MC are seen to disagree when using standard MC samples and cross-sections.

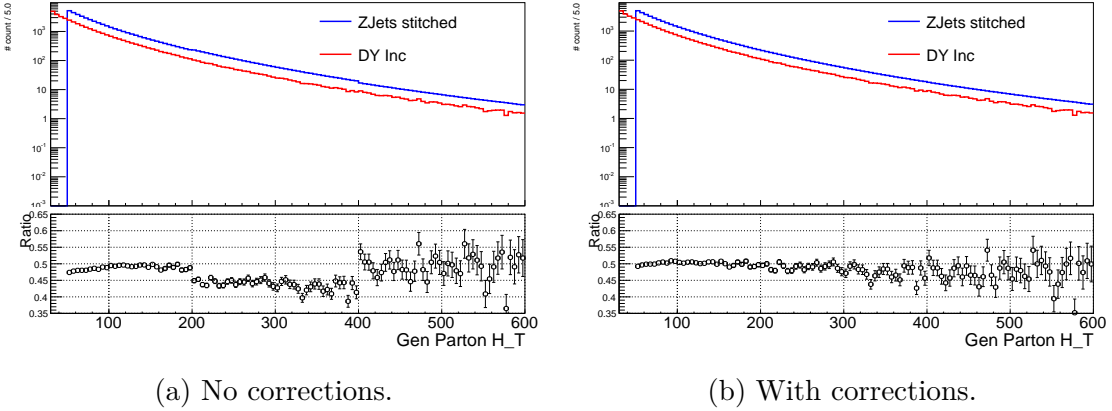


Fig. 5.1 Generator level H_T^{parton} distributions from the inclusive DY + jets and the H_T^{parton} binned Z($\nu\nu$) + jets samples, both before and after cross section corrections.

While data and MC comparisons are not explicitly used in this analysis, ratios of MC yields are, and so cross-section correction factors for the main MC samples must be derived. Corrections are taken as the data to MC ratio in the $150 \leq H_T < 200$ GeV sideband region. For the three main EWK backgrounds, $W + \text{jets}$, $Z(\nu\nu) + \text{jets}$ and $t\bar{t} + \text{jets}$, a particular combination of control region selection (control regions described later in Chapter 7), jet and b-tagged jet multiplicity, is used to ensure a pure selection of a given process. The selections and their purities are listed in Table 5.4. Also listed are the derived correction factors to be applied to MC, indicating the level of disagreement present between data and MC observed in the sideband region.

Table 5.4 The process-specific sideband corrections applied to MC sample, with the selection used and its corresponding purity.

Process	Selection	Purity	Correction factor
W + jets	$\mu + \text{jets}, 2 \leq n_{\text{jet}} \leq 3, n_b = 0$	0.91	0.93 ± 0.01
Z($\rightarrow \mu\mu$) + jets	$\mu\mu + \text{jets}, 2 \leq n_{\text{jet}} \leq 3, n_b = 0$	0.98	0.94 ± 0.04
t\bar{t}	$\mu + \text{jets}, n_{\text{jet}} \geq 2, n_b \geq 2$	0.87	1.21 ± 0.05

The validity of this procedure is ultimately tested using a suite of closure tests (discussed in Section 7.3.1).

5.4 Predicting event yields for high b-jet multiplicities

Yields taken from the MC samples listed in Table 5.2 are used as input to the SM background prediction techniques described later in Chapter 7. Given the relatively low number of b tagged jets present in such electroweak background processes, events containing high b-jet multiplicities (n_b) are often dominated by mistagged light quarks. Consequently, high- n_b yields often suffer from a lack of precision due to large statistical uncertainties. In order to reduce the statistical uncertainties associated with such events, a method has been developed which considers individual quark-flavour tagging efficiencies and the underlying quark flavour distribution (both measured directly from simulation) to determine high- n_b event yields with a greater precision. This method is employed in this analysis, and while it will not be outlined here, it is described in detail elsewhere [77].

CHAPTER 6

THE α_T ANALYSIS

6.1 Analysis Overview

Analyses searching in the jets and \cancel{E}_T final state encounter significant backgrounds from SM sources of both genuine and fake \cancel{E}_T . Genuine \cancel{E}_T originates from $t\bar{t}$, W and Z boson production, with one or more neutrinos in the final state. In this analysis background predictions are made for these processes using extrapolations into the signal region from independent, process-specific control samples, as described in Chapter 7. Fake \cancel{E}_T predominantly originates from mismeasurement of QCD multijet (MJ) production, which is the dominant process in the hadronic environment and phase space considered in this analysis due to its very large cross section. Small inconsistencies in the handling of such large backgrounds or rare detector effects can therefore have a significant impact on an analysis. This background is reduced to an entirely negligible level using the dimensionless kinematic variable α_T .

In this analysis, following the generic signal selection criteria (described in Section 6.4), events are binned in exclusive categories of H_T , and the multiplicity of jets and b-tagged jets, n_{jet} and n_b , as summarised in Table 6.1. Such binning allows for targeted interpretations across the vast array of possible simplified model final states, while reducing background yields to a minimum.

The main analysis search region is described in the remainder of this chapter.

6.1.1 The α_T kinematic variable

Attempting to accurately measure the QCD contribution to the total background is particularly challenging given the hadronic environment of the LHC and the lack of precise measurements and calculations of the large multijet cross sections involved.

Table 6.1 H_T bin lower bounds used for each n_{jet} and n_b category.

(n_{jet}, n_b)	H_T bins (GeV)										
(2-3,0)	200	275	325	375	475	575	675	775	875	975	>1075
(2-3,1)	200	275	325	375	475	575	675	775	875	975	>1075
(2-3,2)	200	275	325	375	475	575	675	775	>875		
(\geq 4,0)	200	275	325	375	475	575	675	775	875	975	>1075
(\geq 4,1)	200	275	325	375	475	575	675	775	875	975	>1075
(\geq 4,2)	200	275	325	375	475	575	675	775	>875		
(\geq 4,3)	200	275	325	375	475	575	675	775	>875		
(\geq 4, \geq 4)	200	275	325	>375							

As an alternative approach, the goal of this analysis is to reduce QCD down to entirely negligible levels with respect to background processes with genuine \cancel{E}_T , achieved through the use of the dimensionless kinematic variable, α_T . The di-jet variable α was first proposed by Randall et al. in 2008 [78], and later translated into the transverse plane for use with LHC analyses [79, 80]. α_T is defined for di-jets as:

$$\alpha_T = \frac{\sqrt{E_T^{j_2}/E_T^{j_1}}}{\sqrt{2(1 - \cos(\Delta\phi))}}, \quad (6.1)$$

where $E_T^{j_1}$ and $E_T^{j_2}$ are the reconstructed transverse energies of the first and second p_T -ordered jets respectively, and $\Delta\phi$ is the separation between the two jets in the ϕ plane.

A perfectly measured di-jet event containing back to back jets in ϕ of equal energy will have an α_T value of 0.5, whereas events with \cancel{E}_T originating from jet energy mismeasurements will have values of $\alpha_T < 0.5$. Only events containing sources of genuine \cancel{E}_T , whether from SM or BSM sources, can have values of $\alpha_T > 0.5$.

The α_T variable can be generalised to any higher jet multiplicity by reducing an n -jet system to two pseudo-jets. Each pseudo-jet is constructed from any number of jets. All possible combinations are considered with the goal of finding the configuration for which the difference in H_T between each pseudo-jet, ΔH_T , is minimised. α_T then takes the form:

$$\alpha_T = \frac{1}{2} \times \frac{H_T - \Delta H_T}{\sqrt{H_T^2 - \cancel{H}_T^2}} = \frac{1}{2} \times \frac{1 - \frac{\Delta H_T}{H_T}}{\sqrt{1 - \left(\frac{\cancel{H}_T}{H_T}\right)^2}}. \quad (6.2)$$

The α_T variable leads to a correlation between the two variables of \cancel{H}_T and ΔH_T ,

as demonstrated in Figure 6.1 by the black contours of constant α_T . As QCD events (Figure 6.1a) contain no genuine source of missing energy they exhibit a correlation between the two variables \cancel{H}_T and ΔH_T . They sit at low \cancel{H}_T , where missing energy arises predominantly due to jet mismeasurement, thereby largely having $\alpha_T < 0.5$. Invisible decays of the Z-boson (Figure 6.1b) sit at higher values of \cancel{H}_T due to the presence of neutrinos in the final state, allowing them to achieve α_T values greater than 0.5. Finally a SUSY decay (Figure 6.1c), with genuine missing transverse energy provided by the neutralino, breaks any correlation between \cancel{H}_T and ΔH_T , sitting also

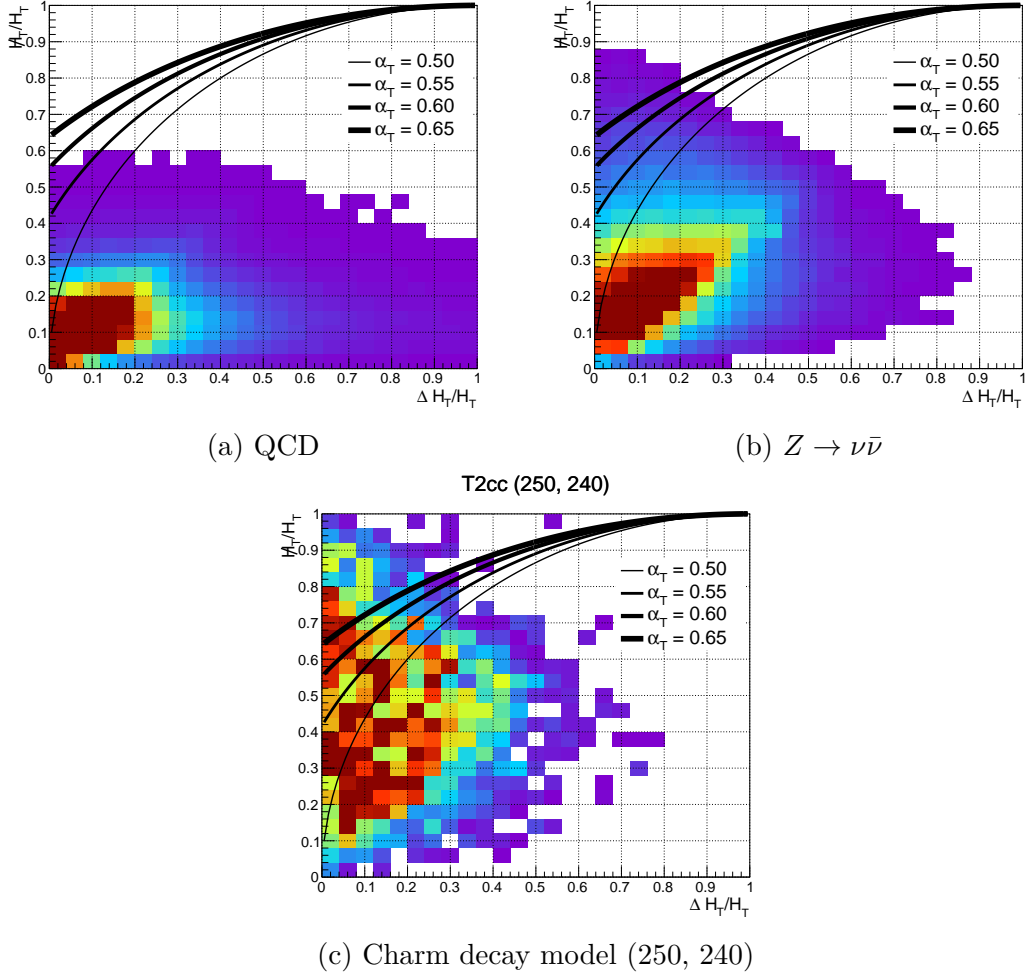


Fig. 6.1 The correlation between \cancel{H}_T and ΔH_T for MC samples of QCD, $Z \rightarrow \nu\bar{\nu}$ and an example mass point of the charm decay signal model ($m_{\tilde{t}} = 250$ GeV, $m_{\tilde{\chi}^0} = 240$ GeV). Contours of constant α_T are shown in black. Each axis is normalised according to the event H_T . Events are required to have $n_{\text{jet}} \geq 4$.

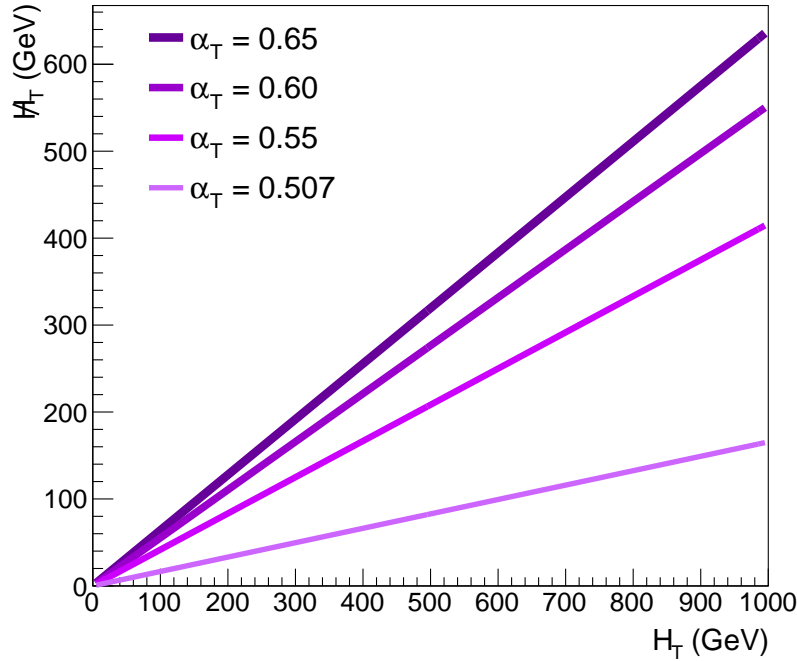


Fig. 6.2 The correlation between H_T and \cancel{H}_T for different α_T values, with the assumption of $\Delta H_T = 0$.

at higher values of α_T .

Through the requirement of α_T in a given region of H_T , a certain missing energy threshold is implied. Figure 6.2 shows this relationship for the assumption of $\Delta H_T = 0$ - an assumption which yields the minimum \cancel{H}_T values. Given this correlation, the implicit missing energy threshold can be maintained across the H_T range by lowering the α_T thresholds in the high H_T region.

6.2 Standard Model Backgrounds

6.2.1 Genuine \cancel{E}_T

The dominant Electroweak (EWK) source of genuine missing energy comes from Z-boson production where the Z decays to neutrinos, $Z \rightarrow \nu\bar{\nu}$, with associated jets. This source of background is considered irreducible.

Events containing leptonic decays of W bosons, $W \rightarrow \ell\nu$, originating either from direct W production, or via the decay of a top quark from $t\bar{t}$ production, are sources of genuine missing energy due to the presence of a weakly interacting neutrino which

evades detection. Such events are vetoed in the signal region due to the presence of a lepton. However, if the lepton is not detected, leptonic W decays can pass the signal selection, forming a significant SM background.

Leptons can be ‘lost’ for a variety different reasons, but ultimately for failing the lepton ID criteria. There are numerous potential causes, the most prevalent being soft-leptons below the ID’s p_T threshold or non-isolated leptons which pass the ID quality cuts but fail the isolation requirement.

Following the hadronic selection requirements (outlined in Section 6.4), any remaining contributions from SM EWK backgrounds are estimated using a fully data-driven transfer factor technique, described in detail in Section 7.1.

6.2.2 Fake \cancel{E}_T

As mentioned previously, the dominant source of background for analyses searching for a multijet final state is from QCD. A fully-measured QCD event would consist of multiple jets balancing each other in all planes. However, in order to enter the signal region an event must contain missing energy, \cancel{H}_T (equivalent to \cancel{E}_T in all-hadronic events).

The most common way for a balanced multijet (MJ) event to gain \cancel{H}_T occurs if one or more of the jets are mismeasured, such that their vectorial sum leads to non-zero \cancel{H}_T . This can occur due to detector issues, or due to stochastic fluctuations within the inherent jet-resolution of the detector. The former is protected against by the \cancel{E}_T filters summarised in Table 4.5 and using a further filter to remove events affected by non-functioning or damaged regions of the ECAL system, where events are vetoed if they contain significant energy deposits within a given distance from a known problematic region. The latter is dealt with using a cut on the α_T variable where events with fake missing energy signatures give values < 0.5 .

QCD MJ events can also appear to contain non-zero missing energy due to the threshold requirements of jets. If an event contains one or more jets below the analysis threshold, then the event is measured as imbalanced and containing \cancel{H}_T . Events such as these are largely removed with the α_T requirement, however in addition a requirement is made on the ratio $\cancel{H}_T/\cancel{E}_T$.

Details of residual QCD cleaning cuts are given later in Section 7.4.

6.3 Signal Triggers

Events are collected at the HLT using a dedicated suite of signal triggers. For an event to pass the trigger requirements, it must exceed both a H_T and an α_T threshold. Trigger rate can be maintained by varying the threshold on each of these independent requirements, as shown in Table 6.2. Each H_T bin in the analysis is seeded by a specific signal trigger, with a 25 GeV offset between online H_T threshold used in the trigger itself and offline H_T threshold used to define the H_T bin (with the exception of the 200 GeV bin, for which the two thresholds are equal).

Exclusively for this analysis, the additional ‘Parked’ trigger `HT200_AlphaT0p57` is included, seeding the new $H_T > 200$ GeV bin. Such a low threshold allows sensitivity to be maintained for softer physics signatures, such as those expected from compressed spectra SUSY decays studied in this work.

Trigger efficiencies are measured using an unbiased single-muon reference trigger, `HLT_IsoMu24_eta2p1`, via a muon tag and probe method where a single-muon is selected and then subsequently ignored from the analysis when calculating event level variables such as H_T , \mathcal{H}_T and α_T . Efficiencies are measured for each H_T bin and for each n_{jet} category, as summarised in Table 6.2. Example trigger ‘turn-on’ curves are shown for the 3 lowest H_T bins in figures 6.3 and 6.4. The curves are shown both differentially and cumulatively, to show the efficiency for events of a given α_T value and above an α_T threshold respectively. For the bins with $H_T > 375$ GeV, the triggers are measured as fully efficient. Inefficiencies in the low H_T bins are understood as being due to the relatively high threshold L1 seed trigger used for this region, in order to maintain low rates in the high PU environment encountered throughout Run I. Lower efficiencies are also observed in the $n_{\text{jet}} \geq 4$ category due to the presence of softer jets, as an increased number of jets must equate to the same total H_T requirement of a

Table 6.2 Signal triggers, the L1 seed triggers and their efficiencies measured for per H_T and n_{jet} category.

Offline H_T region (GeV)	Offline α_T threshold	L1 seed (<code>L1_?</code>) (highest thresholds)	Trigger (<code>HLT_?</code>)	Efficiency (%)	
				$2 \leq n_{\text{jet}} \leq 3$	$n_{\text{jet}} \geq 4$
$200 < H_T < 275$	0.65	<code>DoubleJetC64</code>	<code>HT200_AlphaT0p57</code>	$81.8^{+0.4}_{-0.4}$	$78.9^{+0.3}_{-0.4}$
$275 < H_T < 325$	0.60	<code>DoubleJetC64</code>	<code>HT200_AlphaT0p57</code>	$95.2^{+0.3}_{-0.4}$	$90.0^{+1.2}_{-1.3}$
$325 < H_T < 375$	0.55	<code>DoubleJetC64 OR HTT175</code>	<code>HT300_AlphaT0p53</code>	$97.9^{+0.3}_{-0.3}$	$95.6^{+0.9}_{-1.0}$
$375 < H_T < 475$	0.55	<code>DoubleJetC64 OR HTT175</code>	<code>HT350_AlphaT0p52</code>	$99.2^{+0.2}_{-0.2}$	$98.7^{+0.5}_{-0.7}$
$H_T > 475$	0.55	<code>DoubleJetC64 OR HTT175</code>	<code>HT400_AlphaT0p51</code>	$99.8^{+0.1}_{-0.3}$	$99.6^{+0.3}_{-0.7}$

given bin. A small number of events are found at values of α_T lower than the trigger threshold leading to spikes in the differential turn-on curves at low α_T values, and an efficiency pedestal in the cumulative turn-on curves. Such events originate from the difference between the online and offline calculations of the α_T variable, where some approximations are made online to reduce latency in the trigger.

All triggers were present throughout Run I, however the `HLT_HT200_AlphaT0p57` trigger was used as part of the ‘Parked’ data stream which was reconstructed at a later date, following the active data-taking period. During data-taking triggers may have ‘prescale’ factors applied to them such that only every n triggered events are actually recorded. Crucially however, the full suite of signal triggers remained without a prescale for the entirety of the 8 TeV data-taking.

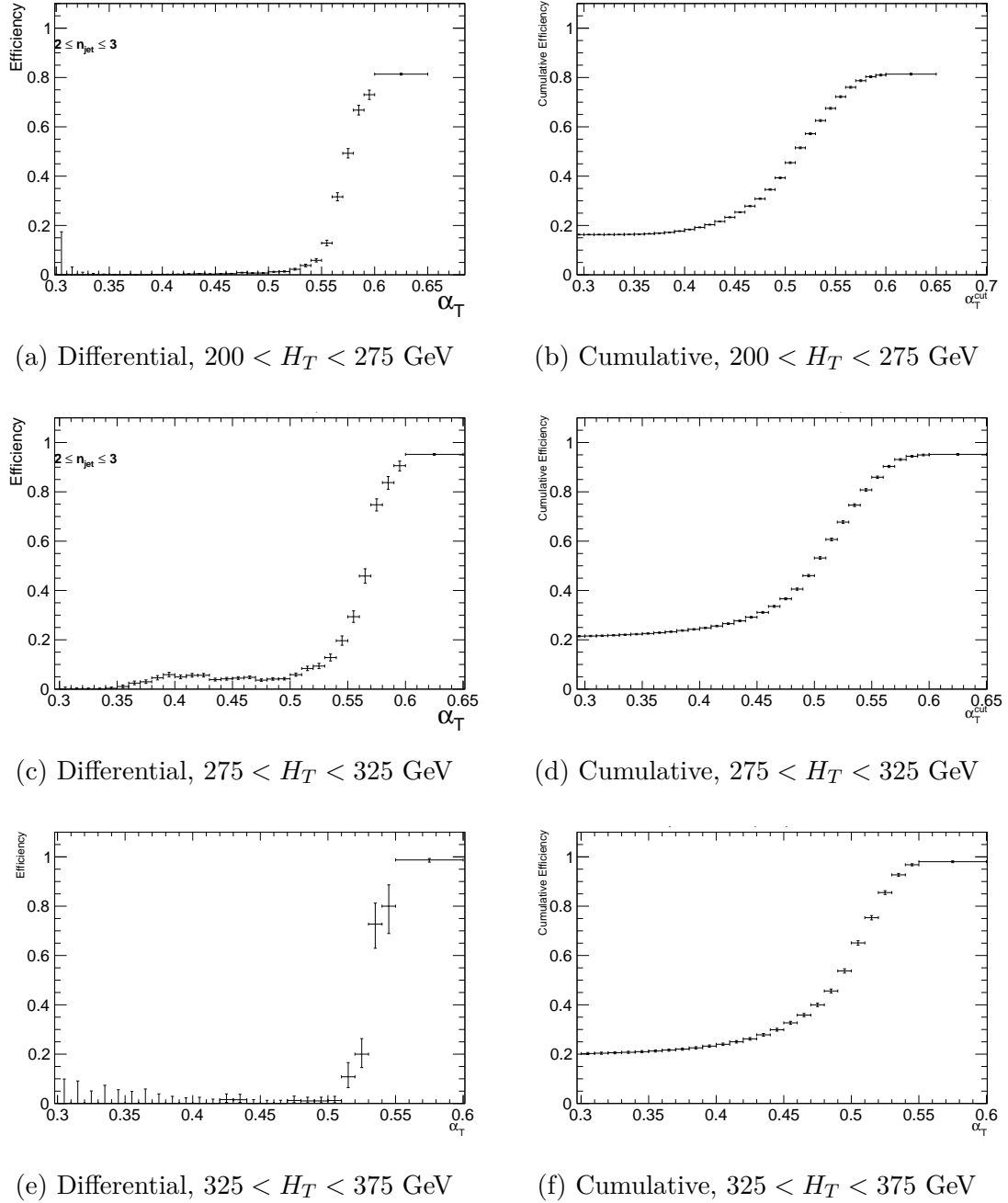


Fig. 6.3 Differential (left) and cumulative (right) efficiency turn-on curves for the signal triggers, for the three lowest H_T bins and $2 \leq n_{\text{jet}} \leq 3$.

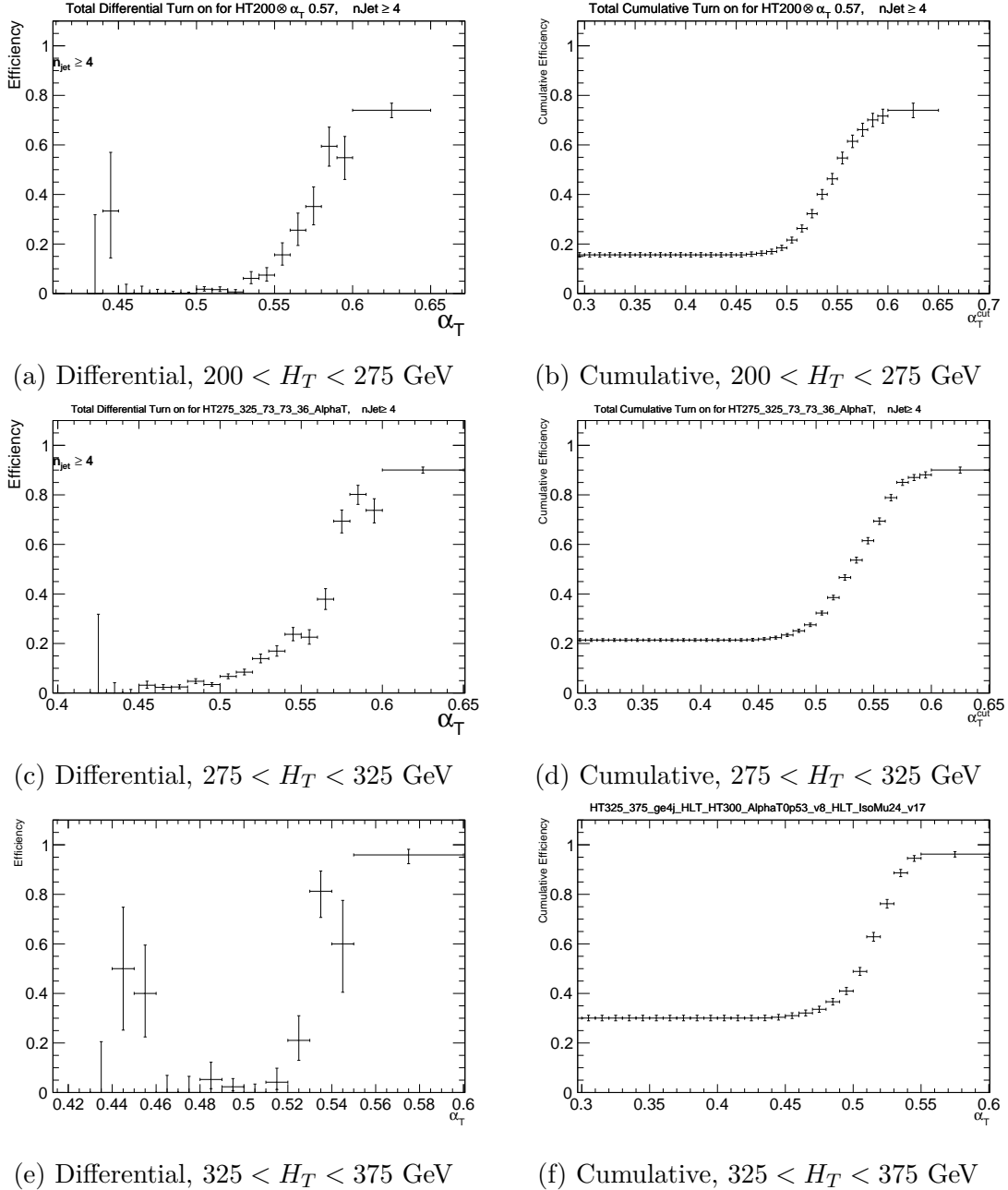


Fig. 6.4 Differential (left) and cumulative (right) efficiency turn-on curves for the signal triggers, for the three lowest H_T bins and $n_{jet} \geq 4$.

6.4 Selection Criteria

Event selection requirements for the signal region are chosen with an aim to maintain sensitivity to hadronically decaying sparticle production, while rejecting as many QCD-type processes as possible. To do so, requirements are made on:

Jets Events are required to contain at least two jets, and have $H_T > 200$ GeV, to ensure the presence of significant hadronic activity. They are categorised by H_T , with jet p_T requirements on the two leading and the remaining additional jets separately. The jet p_T thresholds vary as a function of the H_T bin of the event, as shown in Table 6.3, in order to maintain a similar kinematic phase space throughout the H_T range. Additionally, the leading jet is required to be in the barrel region of the calorimeter, $\eta_{lead-jet} < 2.5$.

Leptons Any events containing leptons are vetoed to ensure only hadronic events are considered, thereby suppressing events with genuine \cancel{E}_T from leptonic decays to neutrinos such as $W \rightarrow \ell\nu$. Furthermore, events are vetoed that contain a jet within $\Delta R < 0.5$ of a muon which fails the ID criteria.

Photons Events containing photons are vetoed, for similar reasons as the leptonic vetoes, in order to maintain a purely hadronic environment.

Single Isolated Tracks Events containing a Single Isolated Track (SIT) are vetoed from the signal region. This tracker based veto is particularly useful for vetoing additional events that contain leptons which have failed our lepton ID requirements entirely and are therefore not considered by the leptonic vetoes. Additionally, the veto also removes background contributions from single-pronged hadronic decays of τ leptons.

Table 6.3 Jet E_T and α_T thresholds per H_T bin.

	H_T bin			
	200–275	275–325	325–375	>375
Lead jet p_T (GeV)	73.3	73.3	86.7	100.0
Second jet p_T (GeV)	73.3	73.3	86.7	100.0
All other jets p_T (GeV)	36.7	36.7	43.3	50.0
α_T	0.65	0.60	0.55	0.55

Event The topology of the event is required to pass a threshold of at least $\alpha_T > 0.55$, a requirement which itself varies as a function of the H_T category being considered, chosen such that the signal triggers are in the efficiency plateau, as summarised in Table 6.3. While no absolute \cancel{E}_T requirement is made, the cut on α_T imposes an implied threshold, maintaining the analysis' sensitivity to very low regions of \cancel{E}_T as shown by Figure 6.2. Furthermore, events are required to have $\cancel{H}_T/\cancel{E}_T < 1.25$ and $\Delta\phi_{min}^* > 0.3$ (defined later in Chapter 7).

A breakdown of the EWK background composition is shown in Figure 6.5, split into the main categories of $Z \rightarrow \nu\bar{\nu}$, $W + \text{jets}$, $t\bar{t}$ and all remaining residual backgrounds, such as single top quark, diboson and Drell-Yann processes.

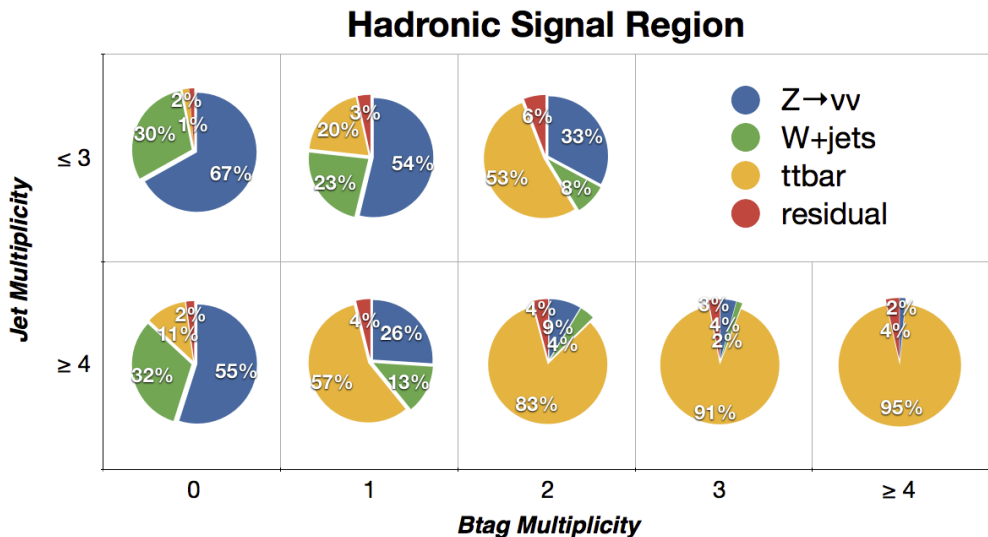


Fig. 6.5 The breakdown of the total electroweak background into component processes as a function of n_{jet} and n_b , for $H_T > 200$ GeV.

6.5 Example distributions and cutflow

Example distributions of α_T , H_T , \cancel{H}_T and jet p_T are shown in Figure 6.6 for simulated SM processes, following the full hadronic selection criteria, with an inclusive selection on H_T , n_{jet} and n_b . Even with this inclusive selection, $Z \rightarrow \nu\bar{\nu}$ is shown to be the biggest contribution to the total SM background, with the ‘lost-lepton’ sources of $W + \text{jets}$ and $t\bar{t}$ following. It is interesting to also note that $Z \rightarrow \nu\bar{\nu}$ and $W + \text{jets}$ have the

hardest \mathcal{H}_T spectra, while $t\bar{t}$ is softer. This is attributed to the greater probability of producing back to back neutrinos, with their missing momenta contributions cancelling to give lower \mathcal{H}_T values.

Example cutflow yields are shown in Table 6.4 for data in the $H_T > 375$ GeV region, employing the full hadronic selection criteria, with an inclusive selection on n_{jet} and n_b . The cuts relate to those described in this chapter, specifically in Section 6.4. The requirement on α_T is shown to reject many orders of magnitude of events, as well as other ‘cleaning’ cuts such as the deadECAL filter and $\mathcal{H}_T/\mathcal{E}_T$.

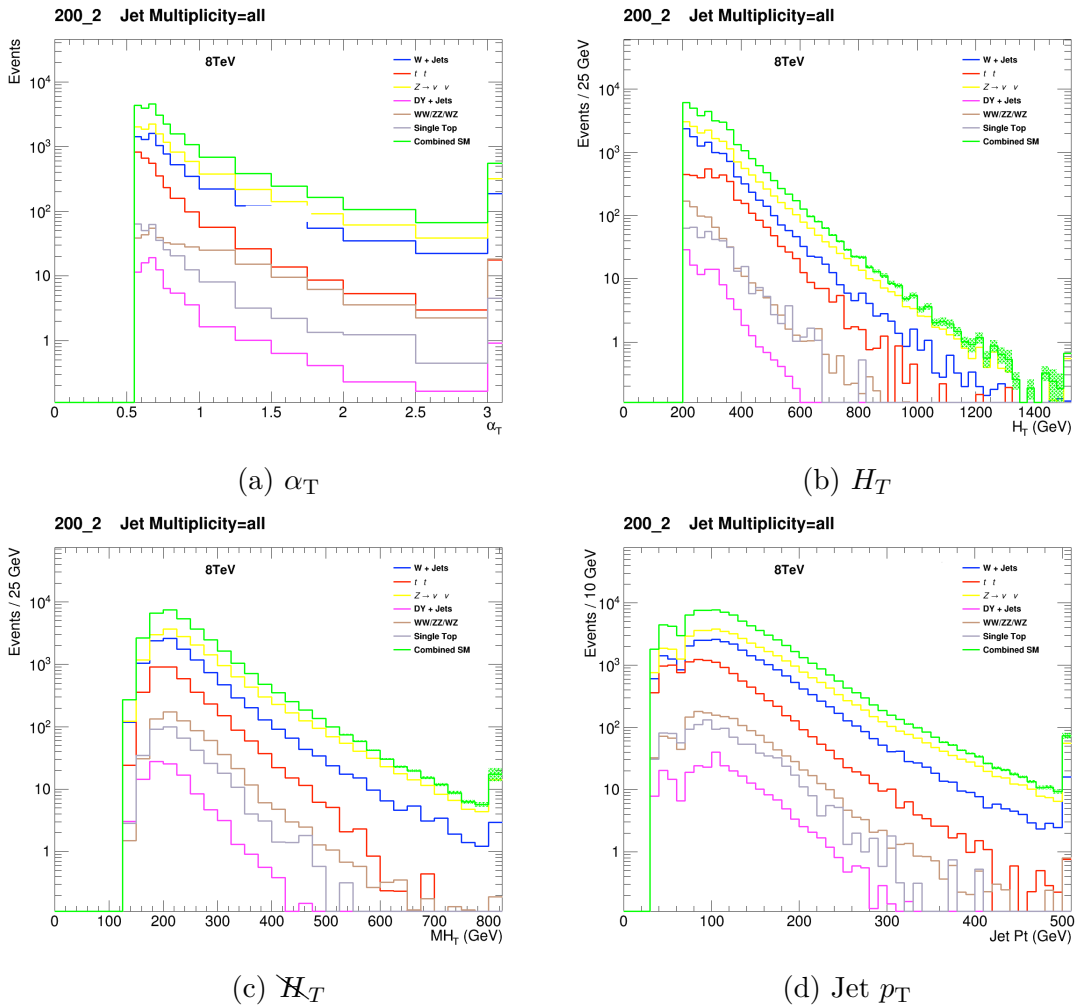


Fig. 6.6 Kinematic distributions of all relevant simulated MC samples following the full hadronic signal selection. The sum of the individual sample contributions is shown in green. Plots are for an inclusive selection of $H_T > 200$ GeV, $n_{jet} \geq 2$, $n_b \geq 0$.

Table 6.4 The cutflow of the hadronic selection in data. The subscript ‘fail’ indicates an object which did not meet all ID requirements, and so is not considered as a ‘common object’. The event selection follows an inclusive selection in data of $H_T > 375$ GeV, $n_{\text{jet}} \geq 2$ and $n_b \geq 0$.

Cut Name	Eff (%)	N
Signal Trigger Accept	100.00	12843698.00
Good Event JSON Filter	95.32	12242217.00
$n_{\text{jet}} \geq 2$	98.93	12110634.00
MET Filters	98.68	11951541.00
Vertex Noise Filter	99.92	11941983.00
DeadECAL Filter	25.59	3056360.00
$n_e = 0$	98.62	3014305.00
$n_\gamma = 0$	97.82	2948741.00
$n_\mu = 0$	98.77	2912517.00
Leading jet $p_T > 100$ GeV	98.20	2860068.00
Leading jet $\eta < 2.5$	97.29	2782463.00
Sub-Leading jet $p_T > 100$ GeV	84.24	2343910.00
$n_{j,\text{fail}} = 0$	83.45	1955899.00
$\Delta R(\mu_{\text{fail}}^i, \text{jet}^j) < 0.5$	98.87	1933858.00
$n_{SIT} = 0$	84.27	1629716.00
$H_T > 375$ GeV	93.45	1522986.00
$\alpha_T > 0.55$	0.55	8305.00
$\cancel{H}_T/\cancel{E}_T < 1.25$	66.82	5549.00
$\Delta\phi_{\min}^* > 0.3$	90.83	5040.00

CHAPTER 7

BACKGROUND ESTIMATION

Predictions of EWK SM backgrounds are made using independent control regions designed to mimic a specific background process observed in the signal region. These regions are orthogonal to the signal region due to the selection of leptons or photons - particles which are subsequently ignored such that the selection kinematics of each event is kept similar to the corresponding process. For each region, Transfer Factors (TF) are constructed from yields in MC in order to extract a prediction in the signal region for a given process. The total EWK prediction is comprised of a prediction of lost-lepton backgrounds originating predominantly from $t\bar{t} + \text{jets}$ and $W + \text{jets}$ processes, and a prediction of $Z(\nu\nu) + \text{jets}$, with the latter being treated differently according to n_b . This process is described in detail in Section 7.1. The validity of this procedure is extensively tested using a suite of Closure Tests, probing multiple characteristics of the prediction technique while allowing for H_T -dependent systematic errors to be derived on the prediction.

Predictions made using this technique are considered as “primitive” predictions and are used only in analysis development and the derivation of background systematics. In order to determine final background counts for interpretation and limit-setting, a fit is made across all signal and control regions, using the likelihood model as described later in Chapter 8. The derived transfer factors and individual yields enter as terms in the likelihood, where all related systematics, potential correlations and signal contamination are accounted for.

Residual contamination from QCD processes are removed through additional cleaning cuts. Studies performed in a QCD enriched sideband region in α_T lead to the definition of these cuts, as described in Section 7.4, ensuring no significant QCD background remains.

7.1 Overview of Electroweak background prediction method

A transfer factor is constructed from MC samples as the ratio of the yield in the signal region, $N_{MC}^{signal}(H_T, n_{jet}, n_b)$, and the yield of a given control region, $N_{MC}^{control}(H_T, n_{jet}, n_b)$, as a function of the analysis binning, H_T , n_{jet} and n_b , defined as:

$$TF = \frac{N_{MC}^{signal}(H_T, n_{jet}, n_b)}{N_{MC}^{control}(H_T, n_{jet}, n_b)}. \quad (7.1)$$

For a given H_T , n_{jet} and n_b bin, the TF is used to extrapolate a yield in data from the control region, $N_{data}^{control}(H_T, n_{jet}, n_b)$, to give a prediction in the signal region $N_{pred}^{signal}(H_T, n_{jet}, n_b)$, using:

$$N_{pred}^{signal}(H_T, n_{jet}, n_b) = N_{data}^{control}(H_T, n_{jet}, n_b) \times TF. \quad (7.2)$$

The control regions are statistically independent and each used for predicting specific background processes.

MC yields, following the application of all MC correction factors described in Chapter 5, are defined by process from the following samples: W + jets (N_W), $t\bar{t}$ + jets ($N_{t\bar{t}}$), DY + jets (N_{DY}), γ + jets (N_γ), single top + jets (N_{top}), WW + jets, WZ + jets and ZZ + jets ($N_{di\text{-boson}}$), and $Z \rightarrow \nu\bar{\nu}$ + jets ($N_{Z \rightarrow \nu\bar{\nu}}$).

The denominator of each transfer factor is constructed using the sum of *all* MC sample yields, for a given control region and analysis category:

$$N_{MC}^{control}(H_T, n_{jet}, n_b) = N_W + N_{t\bar{t}} + N_{DY} + N_\gamma + N_{top} + N_{di\text{-boson}} + N_{Z \rightarrow \nu\bar{\nu}}. \quad (7.3)$$

The numerator is constructed according to the b tag multiplicity being considered. Table 7.1 summarises the control regions used to determine a background prediction as a function of each analysis category. For $n_b \leq 1$, the μ +jets control region is used to predict the lost-lepton background, e.g. $t\bar{t}$ + jets and W + jets. All MC samples are therefore used with the exception of $Z \rightarrow \nu\bar{\nu}$ + jets:

$$N_{MC}^{signal}(H_T, n_{jet}, n_b \leq 1) = N_W + N_{t\bar{t}} + N_{DY} + N_\gamma + N_{top} + N_{di\text{-boson}}. \quad (7.4)$$

In this n_b region the $Z \rightarrow \nu\bar{\nu}$ + jets component of the background is predicted with

the $\mu\mu+\text{jets}$ and $\gamma+\text{jets}$ control regions, using only the $Z \rightarrow \nu\bar{\nu}$ MC yields:

$$N_{MC}^{signal}(H_T, n_{jet}, n_b \leq 1) = N_{Z \rightarrow \nu\bar{\nu}}. \quad (7.5)$$

For $n_b \geq 2$, the $\mu+\text{jets}$ region is used to produce a prediction for all SM processes, including $Z \rightarrow \nu\bar{\nu}$, and therefore the numerator of the TF is defined as:

$$N_{MC}^{signal}(H_T, n_{jet}, n_b \geq 2) = N_W + N_{t\bar{t}} + N_{DY} + N_\gamma + N_{top} + N_{di\text{-boson}} + N_{Z \rightarrow \nu\bar{\nu}}. \quad (7.6)$$

The $\mu\mu+\text{jets}$ and $\gamma+\text{jets}$ control regions are not used beyond the $n_b \leq 1$ categories due to the statistical limitations of such regions at high b tag multiplicities.

It should be noted that although two separate control regions are used to estimate the $Z \rightarrow \nu\bar{\nu}$ background contribution, the result of each is considered by the global likelihood fit to produce the final background prediction (described in Section 8.1).

Table 7.1 The control regions used to produce SM background predictions for each analysis category (n_b , n_{jet}).

n_{jet}	n_b	Control regions
2–3	0	$\mu+\text{jets}$, $\mu\mu+\text{jets}$, $\gamma+\text{jets}$
2–3	1	$\mu+\text{jets}$, $\mu\mu+\text{jets}$, $\gamma+\text{jets}$
2–3	2	$\mu+\text{jets}$
≥ 4	0	$\mu+\text{jets}$, $\mu\mu+\text{jets}$, $\gamma+\text{jets}$
≥ 4	1	$\mu+\text{jets}$, $\mu\mu+\text{jets}$, $\gamma+\text{jets}$
≥ 4	2	$\mu+\text{jets}$
≥ 4	3	$\mu+\text{jets}$
≥ 4	≥ 4	$\mu+\text{jets}$

By employing a technique that uses a ratio of MC yields, direct dependence on MC modelling is greatly reduced. Sources of error inherent to MC samples, such as mismodelling effects, will approximately cancel in the ratio. These errors can potentially include kinematic mismodelling, which could affect analysis acceptance, and mismodelling of instrumental effects, which could affect object reconstruction efficiencies. However, any remaining systematics such as these and others are probed using dedicated Closure Tests (CT), described in detail in Section 7.3.1.

7.2 Control regions

Control region definitions are designed such that they are as kinematically similar as possible to the signal region, with the exception of a selected ‘tag’ muon or photon. The ‘tagged’ particle is then subsequently ignored for the calculation of all analysis variables, such as H_T , \cancel{E}_T , α_T etc. Other differences include mass-window and minor kinematic cuts, aimed at enriching the control regions in certain processes. Due to the selection of the tagged lepton or photon, the control regions are orthogonal to the signal region and therefore minimise any possible signal contamination. However, a full treatment of the signal-contamination and region cross-correlation is taken into account in the background fit and final limit-setting.

The following sections will describe the control regions in more detail, including their targeted background estimations, selection cuts specific to each and their trigger details.

7.2.1 $\mu+\text{jets}$

The $\mu+\text{jets}$ control region is constructed by selecting a single muon with associated jets. This region is used to predict backgrounds from processes such as $W + \text{jets}$ and $t\bar{t} + \text{jets}$. This covers not only the leptonic decays of such productions, where the lepton is not identified for whatever reason, but also the hadronic decays of tau leptons [from high- p_T W bosons]. The event selection therefore is optimised to select W bosons decaying to a muon and a neutrino in the phase-space of the signal.

Triggers

Events are collected using the `HLT_IsoMu24_eta2p1` trigger, which was in place throughout the 8 TeV data-taking period. The efficiency of this trigger was measured by the muon *POG* in bins of the muon p_T and η , as summarised in Table 7.2. Statistical uncertainties are at the per-mille level, and systematics are taken to be 1 %.

Selection Criteria

A single tight isolated muon is selected, with $p_T > 30$ GeV and $|\eta| < 2.1$. The transverse mass of the W , reconstructed by the μ and the \cancel{E}_T (originating from the ν_μ), is required to be in a loose window around the W mass, $30 < M(\mu, \cancel{E}_T) < 125$ GeV. Events are vetoed if $\Delta R(\mu, \text{jet}_i) < 0.5$, for all jets i in the event. To keep the selection

Table 7.2 Muon trigger efficiencies (%) for the μ +jets selection listed by H_T bin and n_{jet} category.

n_{jet}	HT bin low edge (GeV)											
	150	200	275	325	375	475	575	675	775	875	975	1075
2-3	87.2	87.5	87.8	87.9	88.1	88.2	88.4	88.5	88.6	88.8	88.7	88.4
≥ 4	88.1	88.1	88.2	88.4	88.6	88.8	88.9	89.0	89.1	89.0	89.0	89.6

as close to the signal region as possible, other cuts such as the single isolated track veto and H_T/\cancel{E}_T cuts are also applied.

Specifically for the μ +jets (and $\mu\mu$ +jets) control regions, no α_T requirement is made in order to increase the statistics and therefore the predictive power of the regions. This is possible as other requirements, in particular the requirement of a single muon and a specific invariant mass window, greatly reduce any potential contamination from QCD MJ events. The viability of this is specifically tested by dedicated closure tests described later in Section 7.3.1.

Example distributions of μp_T and μ -corrected \cancel{E}_T for this selection are shown in Figure 7.1.

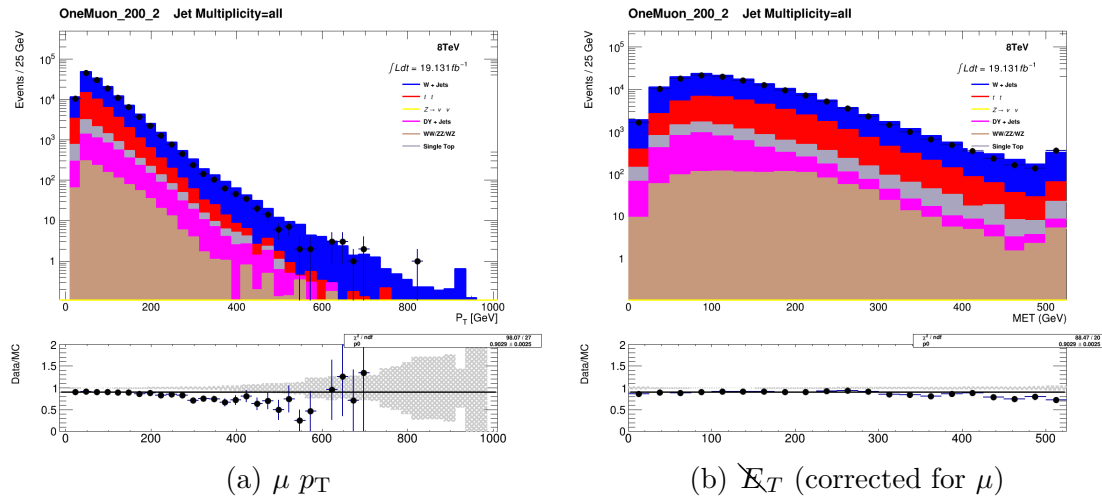


Fig. 7.1 Comparison of data with MC for the μ +jets control selection. The plots show an inclusive selection, $H_T > 200$ GeV, $n_{\text{jet}} \geq 2, n_b \geq 0$.

7.2.2 $\mu\mu+jets$

The $\mu\mu+jets$ region is constructed to predict background contributions from $Z \rightarrow \nu\bar{\nu}$ decays, mimicking this decay via the kinematically similar $Z \rightarrow \mu\mu + jets$ process where both muons are subsequently ignored. The region is used to provide low H_T coverage ($H_T > 200$ GeV) for the $Z \rightarrow \nu\bar{\nu}$ background prediction, where the $\gamma+jets$ region (Section 7.2.3) is unable to do so.

Triggers

The trigger used is the same as for the $\mu+jets$ region, as described in Section 7.2.1. Trigger efficiencies are significantly improved for the dimuon selection given that either of the muons can cause a positive trigger decision, as shown in Table 7.3. Systematic errors are considered of the same magnitude as for the $\mu+jets$ trigger efficiencies.

Table 7.3 Muon trigger efficiencies (%) for the $\mu\mu+jets$ selection listed by H_T bin and n_{jet} category.

n_{jet}	HT bin low edge (GeV)											
	150	200	275	325	375	475	575	675	775	875	975	1075
2–3	98.4	98.5	98.5	98.6	98.6	98.6	98.6	98.7	98.6	98.7	98.7	98.7
≥ 4	98.4	98.4	98.4	98.6	98.5	98.6	98.6	98.6	98.6	98.6	98.8	98.7

Selection Criteria

The selection for the $\mu\mu+jets$ region is very similar to that of the $\mu+jets$ region, described in Section 7.2.1, with differences chosen to enrich the region in Z bosons decaying to pairs of muons in the kinematic phase space of the signal region. Two tight isolated muons are selected, each with $p_T > 30$ GeV and $|\eta| < 2.1$. Their invariant mass is required to be tight around m_Z , $m_Z - 25 < M_{\mu_1\mu_2} < m_Z + 25$ GeV. Furthermore, a veto is made on events satisfying $\Delta R(\mu_i, jet_j) < 0.5$, for every muon i and every jet j . Similarly as in the $\mu+jets$ region selection, no α_T requirement is made.

Example distributions of transverse mass of the muon pair, $M_T(\mu\mu)$, and $\mu_2 p_T$ for this selection are shown in Figure 7.2.

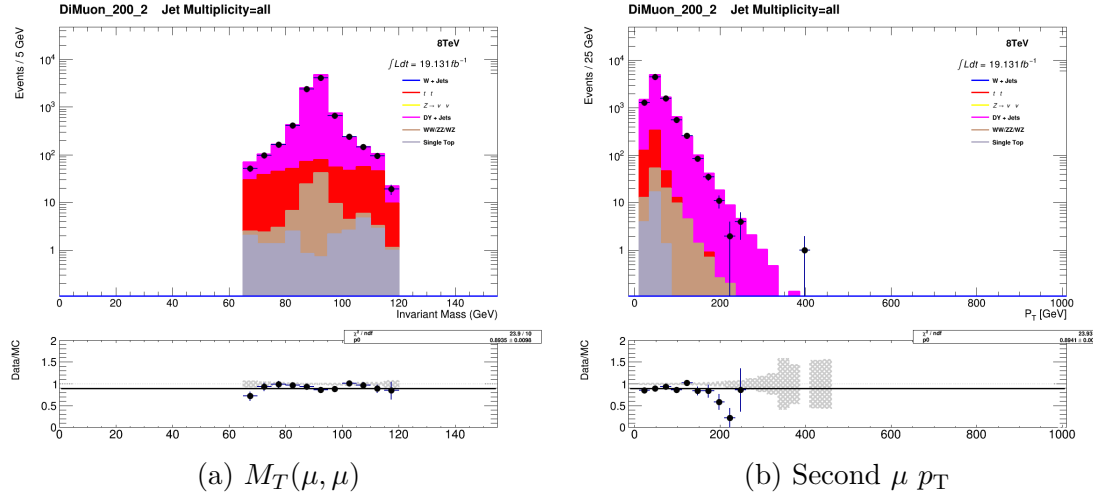


Fig. 7.2 Comparison of data with MC for the $\mu\mu$ +jets control selection. The plots show an inclusive selection, $H_T > 200$ GeV, $n_{\text{jet}} \geq 2$, $n_b \geq 0$.

7.2.3 γ +jets

The γ +jets region is used to predict the $Z \rightarrow \nu\bar{\nu}$ background contribution, given its similar kinematics when the γ is ignored from the event, as well as a larger production cross section relative to $\mu\mu$ +jets. Due to trigger thresholds, the γ +jets region cannot make predictions for $H_T < 375$ GeV, and so is complimentary to the $\mu\mu$ +jets region prediction.

Triggers

Events are collected using the `HLT_Photon150` trigger. The trigger's efficiency is measured using a procedure equivalent to the method used for the signal triggers, described in Section 6.3, with the `HLT_Photon90` trigger as a reference. The trigger is found to be 100% efficient for $E_T^\gamma > 165$ GeV and $H_T > 375$ GeV, as shown by the turn on curves in Figure 7.3.

Selection Criteria

Exactly one photon satisfying tight isolation criteria is required, with $p_T > 165$ GeV and $|\eta| < 1.45$. In addition, events are vetoed if $\Delta R(\gamma, \text{jet}_i) < 1.0$ is satisfied, for all jets i in the event.

An example distribution of the γ p_T for this selection is shown in Figure 7.4.

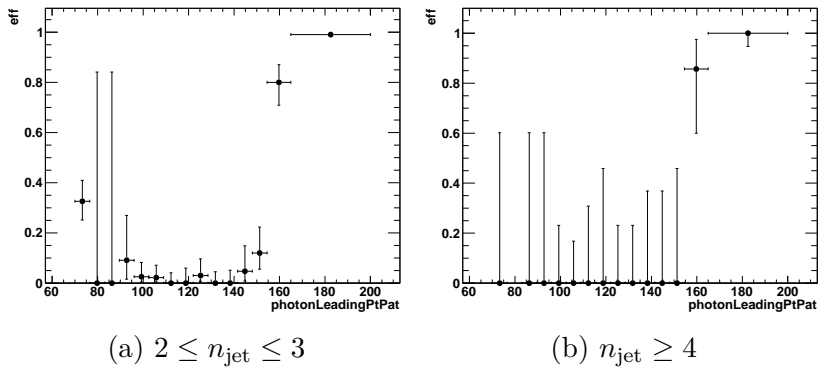


Fig. 7.3 Efficiency turn-on curves for the photon trigger, based on the $\gamma + \text{jets}$ selection, for $H_T > 375$ GeV, with $2 \leq n_{\text{jet}} \leq 3$ (Left) and $n_{\text{jet}} \geq 4$ (Right).

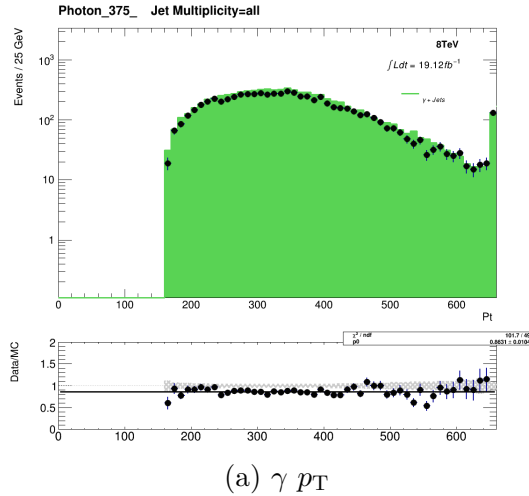


Fig. 7.4 Comparison of data with MC for the γ +jets control selection. The plot shows an inclusive selection, $H_T > 200$ GeV, $n_{\text{jet}} \geq 2$, $n_b \geq 0$.

7.3 Systematic uncertainties on SM background predictions

In order to probe the levels at which the transfer factors are sensitive to relevant uncertainties, a statistically powerful ensemble of Closure Tests (CTs) have been designed. The CT method works by constructing a TF to extrapolate from one sub-region of a particular control region into another control region sub-region. This prediction method is identical to that described in Section 7.1 with the difference that a prediction is made from a control region to another control region, rather than to the signal

region. In doing so, tests can be designed to specifically probe any potential sources of bias in the transfer factors.

7.3.1 Closure tests

Closure tests are performed as a function of H_T , in the two n_{jet} categories, $2 \leq n_{\text{jet}} \leq 3$ and $n_{\text{jet}} \geq 4$. The level of closure is represented by the statistical consistency between predicted and observed yields for each test, in the absence of any assumed systematic uncertainty. The test statistic is defined as $(N_{\text{obs}} - N_{\text{pred}})/N_{\text{pred}}$, with any bias being observed as a statistically significant deviation from zero, or trend in H_T .

Figure 7.5 shows a summary of the eight closure tests considered as ‘core’ tests for the analysis, split into both $2 \leq n_{\text{jet}} \leq 3$ (Figure 7.5a) and $n_{\text{jet}} \geq 4$ (Figure 7.5b). It should be noted that numerous other tests are also considered, but that these eight represent those deemed most important to the background prediction and are therefore used to derive related uncertainties.

The first test, represented by open circles, inspects the modelling of the α_T variable in the $\mu+\text{jets}$ control region. In the analysis a prediction is made between the $\mu+\text{jets}$ region, which has no α_T requirement, and the signal region, with its tight α_T requirement. This particular test probes the validity of the prediction between the ‘bulk’ of the α_T distribution in the control region and the ‘tail’ of the distribution in the signal region. A similar test, not shown here, is also performed for the $\mu\mu+\text{jets}$ control region.

The next two tests, represented by crosses and open squares, probe the different b tag multiplicities in the $\mu+\text{jets}$ control region. The b tag requirements greatly changes the relative admixture of, for example, $W+\text{jets}$ ($n_b = 0$) and $t\bar{t}+\text{jets}$ ($n_b = 1$) events. It is important to note that this test is considered conservative, given that the admixture of $W + \text{jets}$ to $t\bar{t} + \text{jets}$ events varies minimally between control and signal regions, where this extrapolation is made between identical n_b categories in the analysis. Given the focus on b tagging, these tests also investigate the modelling of b quark jets in the simulated data.

Represented by open triangles, a similar test is made for the relative admixture of $Z(\nu\nu) + \text{jets}$ to $W + \text{jets}$ and $t\bar{t} + \text{jets}$, by predicting between the $\mu+\text{jets}$ and $\mu\mu+\text{jets}$ control regions. Again, this test is considered conservative, and also probes the muon reconstruction and trigger efficiencies between the different muon multiplicities. These are however already well studied by the muon *POG* using data-driven techniques.

As described in Section 7.1, the $Z \rightarrow \nu\bar{\nu}$ prediction is made from both the $\gamma+\text{jets}$

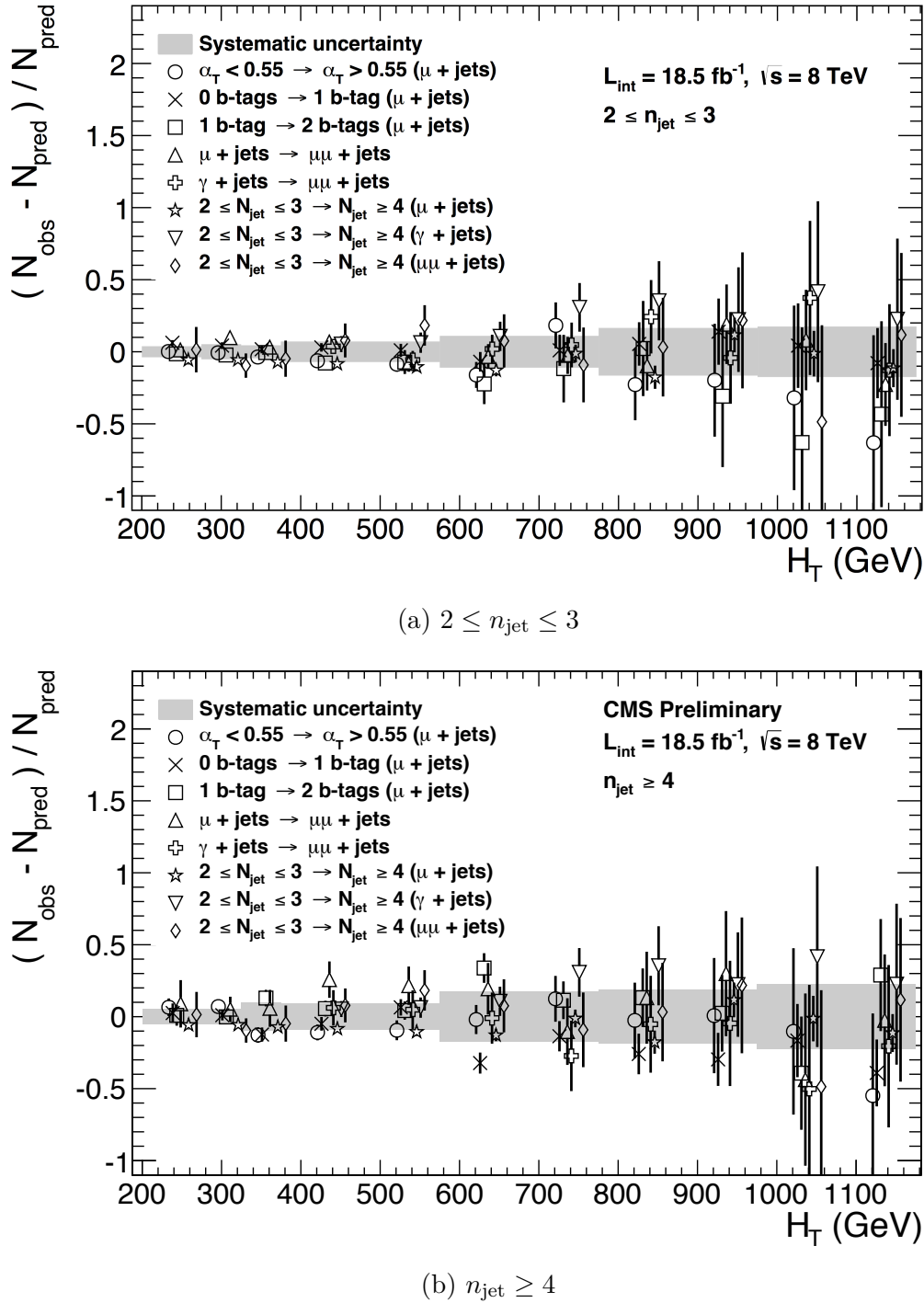


Fig. 7.5 The results of the eight core closure tests (open symbols), shown over the systematic uncertainty bands for each of the five H_T regions (shaded grey), for the two jet multiplicity regions (a) $2 \leq n_{\text{jet}} \leq 3$ and (b) $n_{\text{jet}} \geq 4$.

and $\mu\mu+\text{jets}$ regions, and so a test is constructed to predict between these two orthogonal control regions, as shown by the open crosses.

The final three tests, indicated by open stars, triangles and diamonds, make predictions between the two different jet multiplicity categories in each control region, thereby testing jet reconstruction and modelling. These tests are also considered conservative as the analysis only predicts between identical n_{jet} categories in the control and signal regions.

Summary plots of these eight tests are shown in Figure 7.5, indicating no statistically significant biases or H_T dependencies. Figures 7.6a and 7.7a show zeroeth order polynomial fits (blue lines) made to each individual test to assess the level of any potential bias present. In addition, first order polynomial fits (red lines) are made to assess any potential H_T dependence present in the tests, as shown in Figures 7.6b and 7.7b. The best-fit values, χ^2 and p -values obtained from both fits are summarised for each n_{jet} category in Tables 7.4, 7.5 and 7.6.

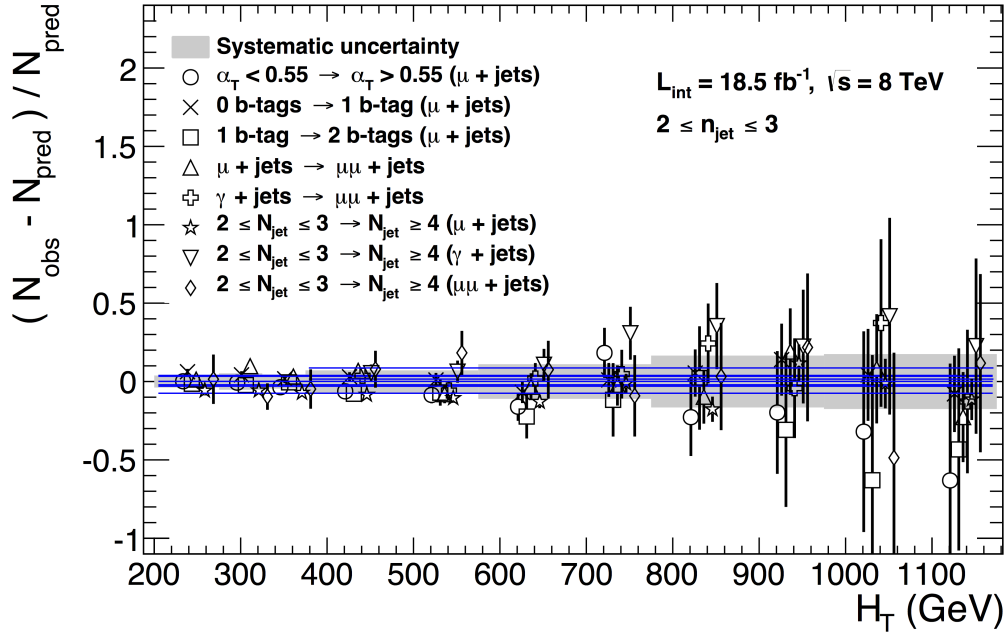
The fits show no significant biases or trends and therefore indicate good closure. The only exception is the 0 b-jets \rightarrow 1 b-jet ($\mu+\text{jets}$) test for the $n_{\text{jet}} \geq 4$ category which has a sub-optimal goodness of fit value for the zeroeth order test. This is attributed to a downwards fluctuation in the adjacent 575–675 GeV bin. Also shown in Table 7.5 are significantly improved fit parameters observed when the same fit is made while ignoring this bin. This leads to the conclusion that this originates from a statistical fluctuation as opposed to a systematic bias. Despite this additional procedure however, it is worth noting this is the only test out of the large ensemble considered indicating a poor fit, further adding to the conclusion that this is indeed due to a statistical fluctuation.

Table 7.4 Results of zeroeth (i.e. constant) and first order (i.e. linear) fits for five sets of closure tests, performed in the $2 \leq n_{\text{jet}} \leq 3$ category.

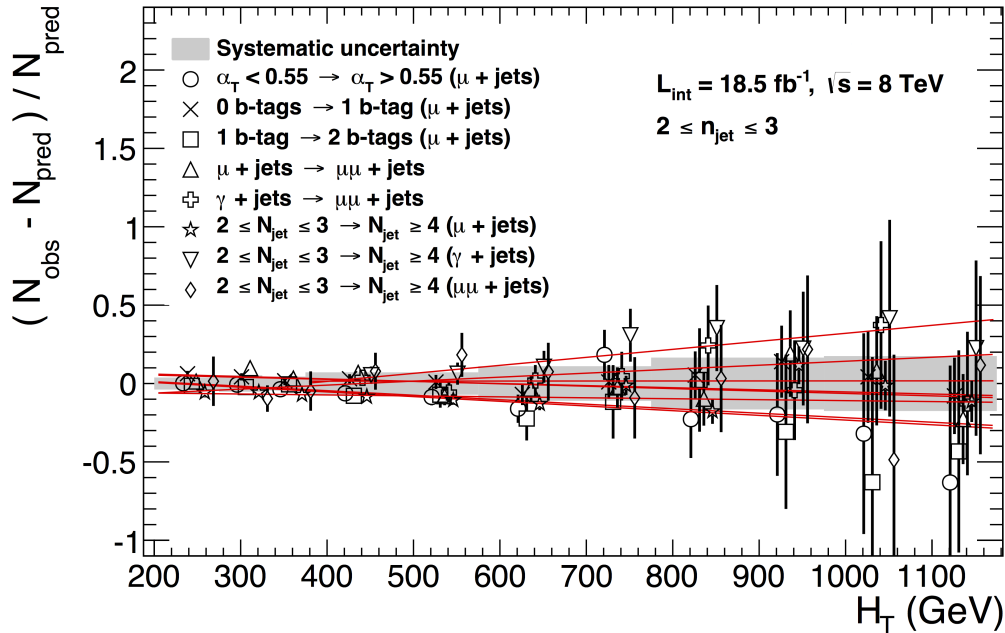
Closure test	Symbol	Constant fit				Linear fit	
		Best fit value	χ^2	d.o.f.	p -value	Slope (10^{-4})	p -value
$\alpha_T < 0.55 \rightarrow \alpha_T > 0.55 (\mu+\text{jets})$	Circle	-0.02 ± 0.01	11.3	10	0.34	-2.9 ± 1.1	0.83
0 b-jets \rightarrow 1 b-jet ($\mu+\text{jets}$)	Times	0.04 ± 0.01	5.8	10	0.83	-1.5 ± 0.9	0.97
1 b-jet \rightarrow 2 b-jets ($\mu+\text{jets}$)	Square	-0.03 ± 0.02	5.3	10	0.87	-3.0 ± 1.7	0.99
$\mu+\text{jets} \rightarrow \mu\mu+\text{jets}$	Triangle	0.03 ± 0.02	12.3	10	0.27	-1.3 ± 1.1	0.28
$\gamma+\text{jets} \rightarrow \mu\mu+\text{jets}$	Cross	-0.02 ± 0.03	3.0	7	0.88	0.0 ± 2.7	0.81

7.3.2 Background systematic uncertainty summary

Under the assumption of closure for the eight core tests, systematic errors on the EWK background prediction are derived for each n_{jet} category in seven regions of



(a) Constant function



(b) Linear function

Fig. 7.6 The results of the eight core closure tests (open symbols), shown over the systematic uncertainty bands for each of the five H_T regions (shaded grey), for $2 \leq n_{\text{jet}} \leq 3$. Included are zeroeth order (left column, blue) and first order (right column, red) fits to each individual closure test.

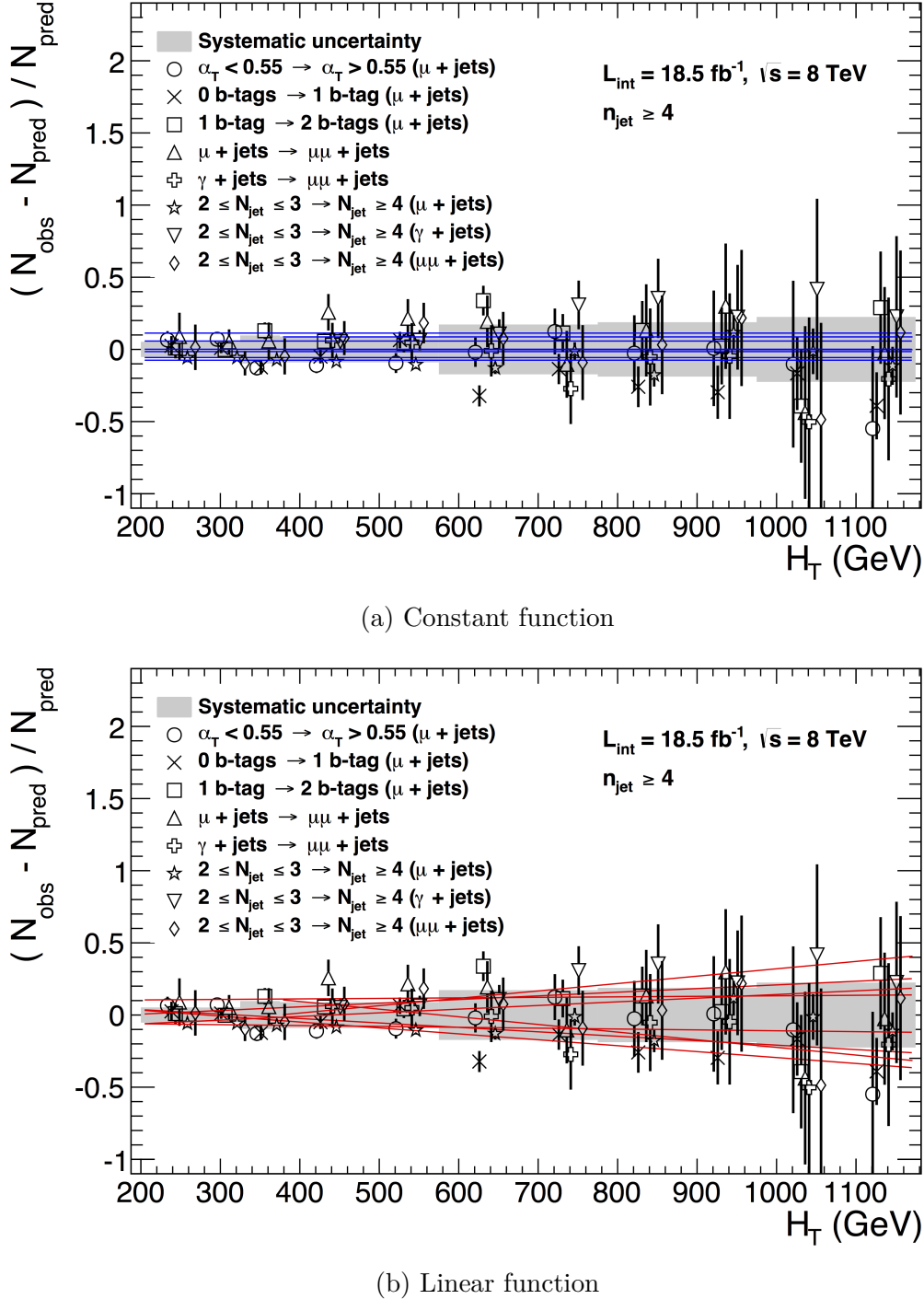


Fig. 7.7 The results of the eight core closure tests (open symbols), shown over the systematic uncertainty bands for each of the five H_T regions (shaded grey), for $n_{\text{jet}} \geq 4$. Included are zeroeth order (left column, blue) and first order (right column, red) fits to each individual closure test.

Table 7.5 Results of zeroeth (i.e. constant) and first order (i.e. linear) fits for five sets of closure tests, performed in the $n_{\text{jet}} \geq 4$ category. An additional test marked with a † is listed, as described in the text.

Closure test	Symbol	Constant fit				Linear fit	
		Best fit value	χ^2	d.o.f.	p-value	Slope (10^{-4})	p-value
$\alpha_T < 0.55 \rightarrow \alpha_T > 0.55 (\mu+\text{jets})$	Circle	-0.02 ± 0.02	17.6	10	0.06	-3.1 ± 1.7	0.11
$0 \text{ b-jets} \rightarrow 1 \text{ b-jet } (\mu+\text{jets})$	Times	-0.06 ± 0.02	24.8	10	0.01	-4.1 ± 1.2	0.02
$0 \text{ b-jets} \rightarrow 1 \text{ b-jet } (\mu+\text{jets})^\dagger$	Times	-0.04 ± 0.02	14.9	9	0.10	-3.9 ± 1.3	0.78
$1 \text{ b-jet} \rightarrow 2 \text{ b-jets } (\mu+\text{jets})$	Square	0.06 ± 0.02	13.7	10	0.19	2.5 ± 1.6	0.28
$\mu+\text{jets} \rightarrow \mu\mu+\text{jets}$	Triangle	0.11 ± 0.05	4.8	10	0.90	0.4 ± 2.7	0.85
$\gamma+\text{jets} \rightarrow \mu\mu+\text{jets}$	Cross	-0.00 ± 0.07	2.3	7	0.94	-5.3 ± 4.7	0.99

Table 7.6 Results of zeroeth (i.e. constant) and first order (i.e. linear) fits for the three sets of closure tests probing the accuracy of jet multiplicity modelling in MC, for each control region.

Region	Symbol	Constant fit				Linear fit	
		Best fit value	χ^2	d.o.f.	p-value	Slope (10^{-4})	p-value
$\mu+\text{jets}$	Star	-0.08 ± 0.01	9.3	10	0.50	0.6 ± 0.7	0.48
$\gamma+\text{jets}$	Inverted triangle	0.09 ± 0.04	3.7	7	0.82	5.1 ± 3.2	0.98
$\mu\mu+\text{jets}$	Diamond	-0.00 ± 0.05	4.7	10	0.91	2.5 ± 2.9	0.92

H_T . Uncertainties are calculated by summing in quadrature the weighted mean and sample variance for all eight tests in a given H_T region, in order to ensure coverage of all test points in that region. These values are summarised in Table 7.7 and also in the summary plots of Figure 7.5, shown as grey bands.

Table 7.7 Summary of the magnitude of systematic uncertainties (%) on the EWK background prediction, derived from the eight core closure tests, for each n_{jet} category and H_T region.

n_{jet}	H_T region (GeV)						
	200–275	275–325	325–375	375–575	575–775	775–975	> 975
2–3	4	6	6	8	12	17	19
≥ 4	6	6	11	11	18	20	26

Systematic uncertainties are considered as fully uncorrelated between the different analysis categories and the H_T regions. As some correlation between, for example, adjacent H_T bins may be expected, this is again considered as a conservative approach as the fit gains more freedom to accommodate the background prediction shape within the data observation.

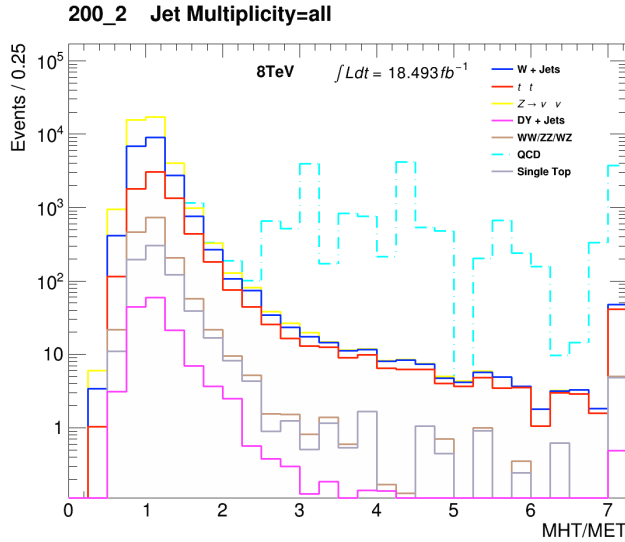


Fig. 7.8 The $\cancel{H}_T/\cancel{E}_T$ distribution of MC events following the hadronic selection criteria, minus the nominal $\cancel{H}_T/\cancel{E}_T$ requirement. The MC yields are stacked, with the QCD contribution shown in cyan. The plot is for a fully inclusive selection of $n_b \geq 0$, $n_{jet} \geq 2$ and $H_T > 200$ GeV.

7.4 Eliminating QCD events

While the α_T requirement removes many orders of magnitude of QCD events, there still exist scenarios in which these events may pass the signal region selection. Accordingly, further requirements are made to ensure the search region is free of any residual QCD contamination, such that it is negligible when compared to the uncertainty on the EWK background prediction.

7.4.1 Multiple jets below threshold

Events are able to acquire non-negligible amounts of \cancel{H}_T without the presence of real \cancel{E}_T if multiple jets are below the jet p_T threshold and their configuration conspires to form a topology that gives high values of α_T . Such events will contain a disparity between the \cancel{E}_T and \cancel{H}_T variables, given that the former is reconstructed using energy deposits and particle flow techniques, while the latter is reconstructed with jet objects. Figure 7.8 shows the contribution of QCD at high $\cancel{H}_T/\cancel{E}_T$ values, even following the α_T requirement. To protect against this scenario, events are required to have $\cancel{H}_T/\cancel{E}_T < 1.25$.

7.4.2 Instrumental effects

It is possible to observe fake \cancel{H}_T if an event's jet is mismeasured. Such mismeasurement can occur due to instrumental effects, such as if a jet deposits energy in a region of the calorimeter system known to be damaged or faulty (hereby referred to as ‘dead’). To protect against this, a filter is employed that finds such a mismeasured jet, rejecting the event if the jet overlaps with a dead region. This filter is known as the ‘Dead ECAL Filter’. To detect such mismeasured jets, the variable $\Delta\phi^*$ is used, defined for a jet j as:

$$\Delta\phi_j^* = \Delta\phi\left(\vec{p}_{\text{T}j}, -\sum_{i \neq j} \vec{p}_{\text{T}i}\right). \quad (7.7)$$

This quantity is the difference in ϕ between the jet and the missing hadronic energy vector calculated using all other remaining jets in the event. An advantage of this variable with respect to the often used $\Delta\phi(\vec{p}_{\text{T}j}, \cancel{H}_T)$, is its detection of spurious missing energy vectors caused by both under-measurements or over-measurements of a jet's energy. In the case of an over-measured jet the nominal \cancel{H}_T would point in the opposite direction to that jet, whereas \cancel{H}_T calculated from all other jets would point in the same direction, giving a low $\Delta\phi^*$.

Events are vetoed if a jet with $\Delta\phi^* < 0.5$ is within $\Delta R < 0.3$ of a known dead region of the calorimeter.

To protect against further jet mismeasurements arising from instrumental effects, multiple event filters (see Table 4.5) are applied to account for well-understood detector issues. However, previously undiscovered and therefore rare detector effects may still be present. To check for such issues the jet giving the minimum $\Delta\phi^*$ value in an event, $\Delta\phi_{\min}^*$, is found and a single entry of the η and ϕ direction of the jet's axis is entered into a map of the detector, as shown in Figure 7.9. Any areas of instrumental issue would be visible as clusters of high event counts. Figures 7.9a and 7.9b show the detector map and the 1D distribution of counts before the Dead ECAL filter is applied, with areas of potential instrumental defects clearly visible, notably as outliers in 1D distribution. Following the application of the Dead ECAL filter, as seen in Figures 7.9c and 7.9d, the hotspot areas and the corresponding outliers are removed. The lack of localised high-count regions or the presence of a tail in the 1D distribution indicate there to be no significant instrumental issues remaining.

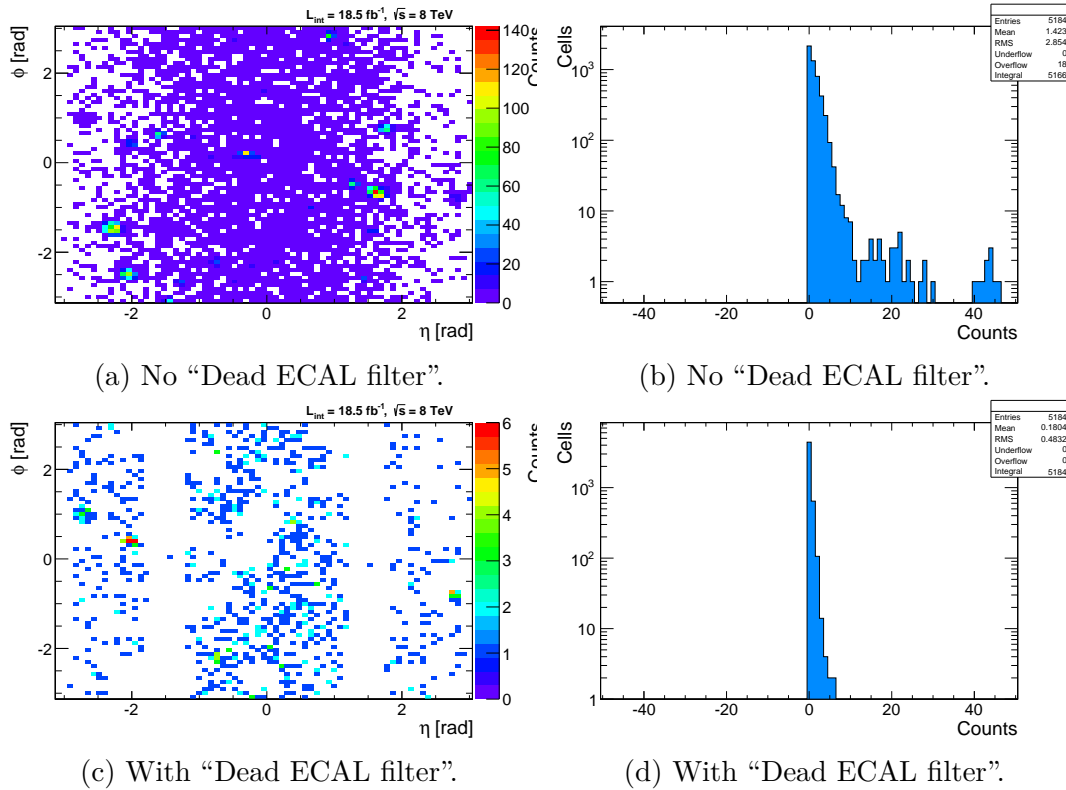


Fig. 7.9 Distribution of jets in (η, ϕ) -space that are responsible for the $\Delta\phi_{min}^*$ value of an event, with (a, b) and without (c, d) the “Dead ECAL filter” requirement applied as part of the signal region selection.

7.4.3 Heavy-flavour jet decays

Jets can also appear to be mismeasured if the parton shower contains heavy flavour mesons which decay semi-leptonically. In rare circumstances, these decays can give the largest fraction of the available momenta to the subsequent neutrino, leading to significant amounts of real \cancel{E}_T and soft-leptons which can evade the lepton vetoes. This effect is compounded when multiple neutrinos are produced in the decay, with a significant fraction of the jet’s energy therefore evading detection.

An event display of a typical event is shown in Figure 7.13. It is important to note the high amount, 185 GeV, of generator level \cancel{E}_T (‘genmetP4True’, thin pink arrow) pointing along the axis of a reconstructed jet with $p_T = 119$ GeV (bold blue arrow) - a configuration which, coupled with multiple additional jets, can conspire to give large values of α_T . The sum of the generator level \cancel{E}_T and the p_T of the jet equate to the p_T of the generator level jet (bold black arrow), indicating that the missing

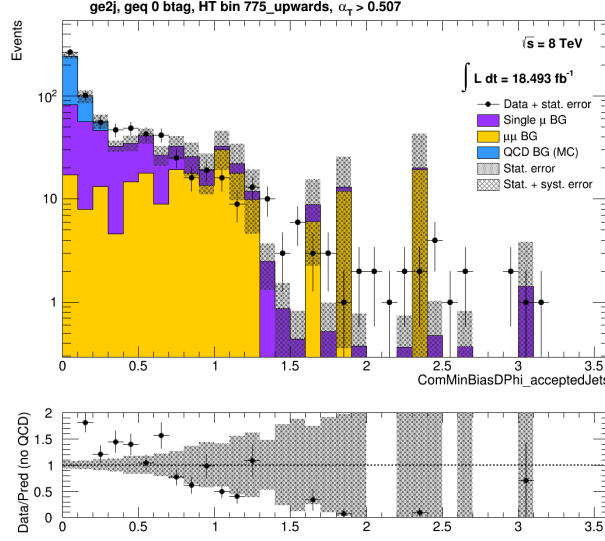


Fig. 7.10 Data (black points) against the EWK background prediction (stacked, yellow and purple) as a function of $\Delta\phi_{min}^*$. The expected yield from QCD MC (cyan) is stacked on top of the EWK prediction, but not included in the ratio plot. The plot represents the QCD control study region, with $n_b \geq 0$, $n_{jet} \geq 2$, $H_T > 775 \text{ GeV}$ and $\alpha_T > 0.507$.

energy of the event comes almost entirely from the neutrinos in the decay of the jet. Furthermore, this implies the ratio $\cancel{H}_T/\cancel{E}_T$ to be near unity, allowing events to also evade the $\cancel{H}_T/\cancel{E}_T < 1.25$ requirement of the signal region.

To investigate events of this type a study region is defined, populated by the single-object H_T trigger, HLT-HT750, which remained un-prescaled throughout Run I. As opposed to a typical signal trigger, the lack of an α_T requirement allows events with low α_T values to be studied. The region is therefore defined by $H_T > 775 \text{ GeV}$ and $0.507 < \alpha_T < 0.55$. Due to the intrinsic correlation of H_T and \cancel{H}_T within the α_T variable (Figure 6.2), this selection provides an effective \cancel{H}_T requirement similar to that of the low H_T categories of the nominal analysis.

Jets containing a \cancel{E}_T source appear as mismeasured and therefore populate a region of low $\Delta\phi^*$ (Equation 7.7). Figure 7.10 shows the data compared to the EWK background prediction as a function of the $\Delta\phi_{min}^*$ value of each event. The disagreement observed at low $\Delta\phi_{min}^*$ is well accounted for by the yield from QCD MC. However, it should be noted that while simulated MC can provide a qualitative understanding of the QCD contamination, it should not be relied upon to determine a quantitative understanding of the phenomenon.

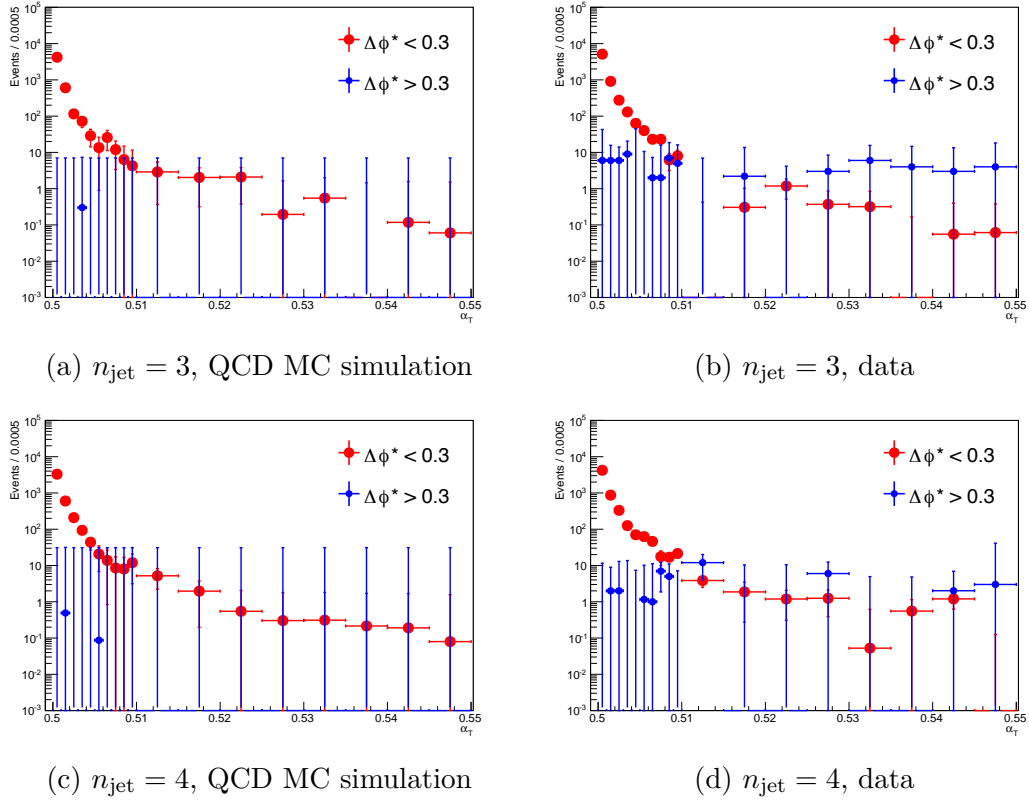


Fig. 7.11 The α_T distribution for events with no $\Delta\phi_{min}^*$ requirement (red circles) and with the $\Delta\phi_{min}^* > 0.3$ requirement (blue circles) as determined from QCD multijet simulation (left column) or data (right column) and the exclusive $n_{\text{jet}} = 3$ (top row) or $n_{\text{jet}} = 4$ (bottom row). Note that negligible QCD contamination is seen in the $n_{\text{jet}} = 2$ category and consequently is not shown here. The QCD control study region requirements have been applied, $H_T > 775$ GeV and $\alpha_T > 0.507$, with $n_b \geq 0$.

As motivated by Figure 7.10, the residual QCD events appear to be well isolated in the region $\Delta\phi_{min}^* < 0.3$. The effect of applying this threshold in the QCD control study region is shown in Figure 7.11. When considering simulation (Figures 7.11a and 7.11c), the requirement of $\Delta\phi_{min}^* > 0.3$ removes all QCD events. However care must be taken when interpreting the same plots for data (Figures 7.11b and 7.11d). To extract the expected QCD MJ contribution from data, observed event counts are corrected to subtract the expected contribution from EWK background processes, as estimated using the standard EWK background prediction method. Given this subtraction, the remaining number of events is expected to be compatible with zero within errors as opposed to exactly zero, as is seen in the data distributions. This supports the conclusion found in simulation that the heavy flavour QCD events are

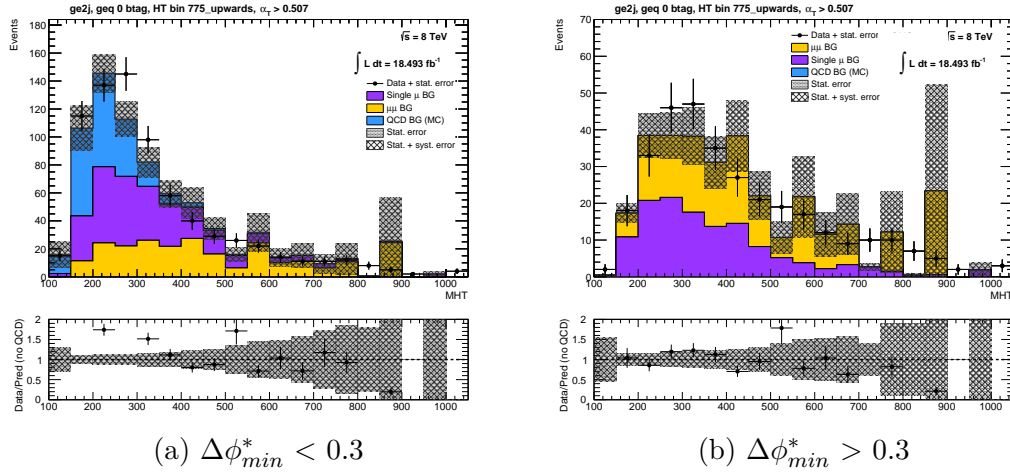


Fig. 7.12 Observations in data compared to the EWK background prediction as a function of the \cancel{H}_T variable. An inclusive selection is made in the QCD study region, $H_T > 775$ GeV, $\alpha_T > 0.507$, $n_{jet} \geq 2$ and $n_b \geq 0$. Plots are shown for both the QCD-enriched $\Delta\phi_{min}^* < 0.3$ and QCD-cleaned $\Delta\phi_{min}^* > 0.3$ regions. Yields from QCD MC (cyan) are shown stacked on the total EWK background prediction, but not included in the ratio.

removed by the application of the $\Delta\phi_{min}^* > 0.3$ requirement.

Figure 7.12 shows data observations compared to the EWK background prediction as a function of \cancel{H}_T for the QCD study region, with both the $\Delta\phi_{min}^* < 0.3$ (Figure 7.12a) and $\Delta\phi_{min}^* > 0.3$ (Figure 7.12b) requirements applied. Following the removal of the low $\Delta\phi_{min}^*$ events, observations agree well with the EWK prediction. As a consequence of these studies, the analysis additionally requires that all events have $\Delta\phi_{min}^* > 0.3$ in the signal region.

7.4 Eliminating QCD events

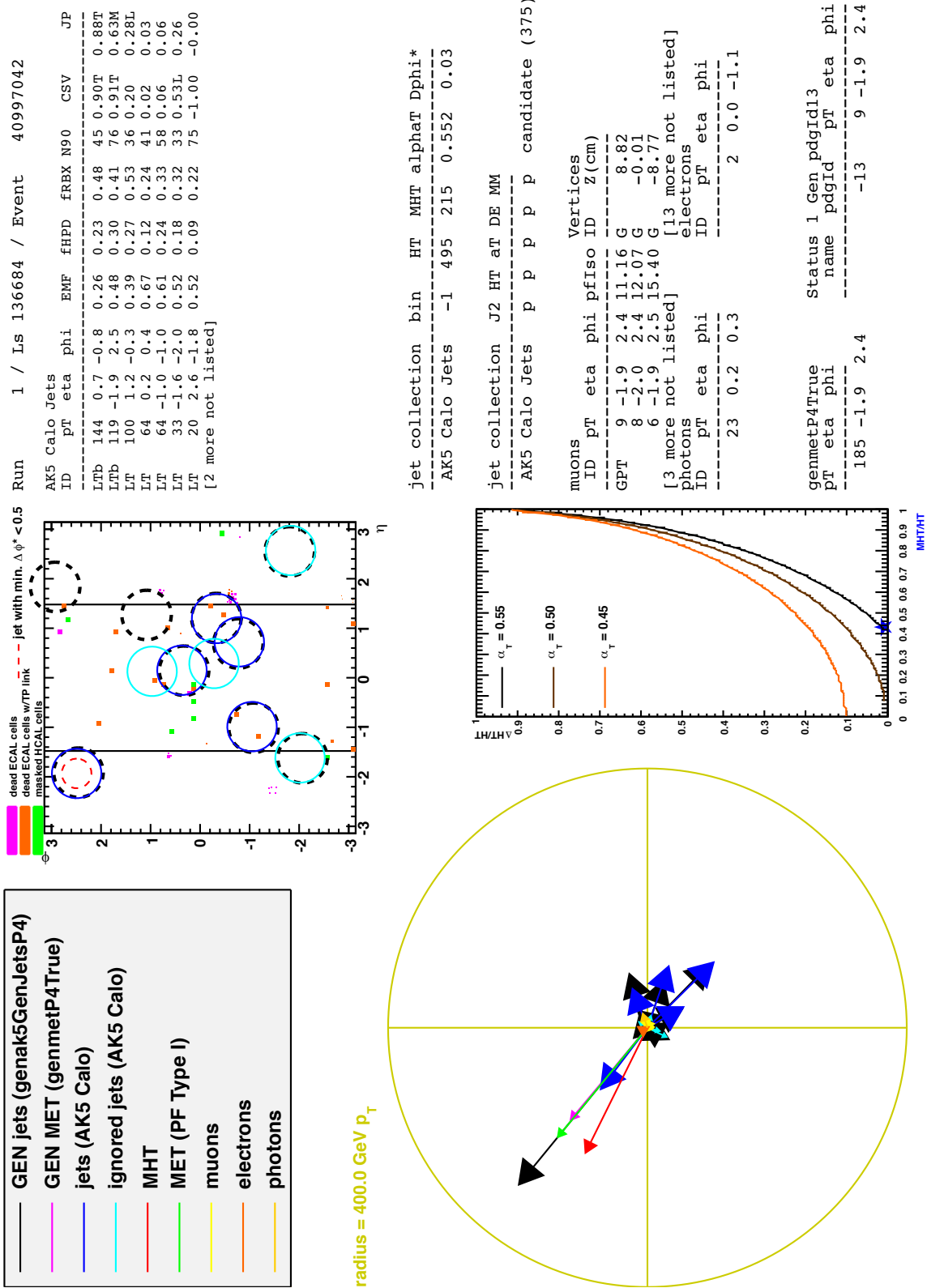


Fig. 7.13 An event display of a typical heavy flavour QCD event, with a jet decaying semi-leptonically with high- p_T neutrinos and therefore considerable generator-level Σ_T .

CHAPTER 8

FIT MODEL AND RESULTS

8.1 Likelihood Model

The likelihood is defined for each analysis category of n_b and n_{jet} as follows.

8.1.1 Hadronic Signal Region

Let n^i be the observed number of events following the full selection in the i^{th} of N bins of H_T . The likelihood is constructed as:

$$L_{hadronic} = \prod_i \text{Pois}(n^i | b^i + s^i), \quad (8.1)$$

where b^i and s^i represent the expected number of background events from SM processes and the expected number of signal events in the bin i . Pois is the Poisson distribution:

$$\text{Pois}(k; \lambda) = \frac{1}{k!} \lambda^k e^{-\lambda}. \quad (8.2)$$

8.1.2 Electroweak Background Contribution

The background is considered to be entirely EWK in origin ($b^i = \text{EWK}^i$), as QCD is made negligible, so can be de-constructed using the relative fraction of $Z \rightarrow \nu\bar{\nu}$ events, f_{Zinv} as:

$$Z_{inv}^i = f_{Zinv} \times \text{EWK}^i, \quad (8.3)$$

$$\text{ttW}^i = (1 - f_{Zinv}) \times \text{EWK}^i, \quad (8.4)$$

where EWK^i is number of expected events from the total EWK background, Z_{inv}^i is the number of expected events from the $Z \rightarrow \nu\bar{\nu}$ contribution and ttW^i is the number of expect events from the W boson production and top quark decay contribution, all in the i^{th} bin. The variable $f_{Z_{\text{inv}}}$ is allowed to float between 0 and 1.

EWK backgrounds are predicted using sideband control regions and transfer factors (Chapter 7). Let n_γ^i , n_μ^i and $n_{\mu\mu}^i$ be the observed event counts in the $\gamma+\text{jets}$, $\mu+\text{jets}$ and $\mu\mu+\text{jets}$ control regions, respectively, with corresponding yields in MC: MC_γ^i , MC_μ^i , $MC_{\mu\mu}^i$. These are further separated into contributions from $Z \rightarrow \nu\bar{\nu}$, $MC_{Z_{\text{inv}}}^i$, and ttW , $MC_{t\bar{t}+W}^i$. Purely as an arbitrary convention, transfer factors are defined as the inverse as those of the analysis:

$$r_\gamma^i = \frac{MC_\gamma^i}{MC_{Z_{\text{inv}}^i}}; \quad r_{\mu\mu}^i = \frac{MC_{\mu\mu}^i}{MC_{Z_{\text{inv}}^i}}; \quad r_\mu^i = \frac{MC_\mu^i}{MC_{t\bar{t}+W}^i}, \quad (8.5)$$

and so likelihoods are written as:

$$L_\gamma = \prod_i \text{Pois}(n_\gamma^i | \rho_{\gamma Z}^j \cdot r_\gamma^i \cdot Z_{\text{inv}}^i), \quad (8.6)$$

$$L_{\mu\mu} = \prod_i \text{Pois}(n_{\mu\mu}^i | \rho_{\mu\mu Z}^j \cdot r_{\mu\mu}^i \cdot Z_{\text{inv}}^i), \quad (8.7)$$

$$L_\mu = \prod_i \text{Pois}(n_\mu^i | \rho_{\mu W}^j \cdot r_\mu^i \cdot \text{ttW}^i + s_\mu^i). \quad (8.8)$$

Both equations 8.6 and 8.7 are used to estimate the maximum likelihood value for Z_{inv}^i , alongside Equation 8.8 for ttW^i , all considered simultaneously through the relationships defined in equations 8.3 and 8.4.

The terms $\rho_{\gamma Z}^j$, $\rho_{\mu\mu Z}^j$ and $\rho_{\mu W}^j$ are correction factors accommodating the systematic uncertainties associated with the control region based background predictions. The relative uncertainties are derived in Section 7.3 and represented by the terms $\sigma_{\gamma Z}^j$, $\sigma_{\mu\mu Z}^j$ and $\sigma_{\mu W}^j$, their values summarised in Table 7.7. Systematics enter the total likelihood as:

$$L_{\gamma \text{ syst.}} = \prod_j \text{Logn}(1.0 | \rho_{\gamma Z}^j, \sigma_{\gamma Z}^j), \quad (8.9)$$

$$L_{\mu\mu \text{ syst.}} = \prod_j \text{Logn}(1.0 | \rho_{\mu\mu Z}^j, \sigma_{\mu\mu Z}^j), \quad (8.10)$$

$$L_{\mu \text{ syst.}} = \prod_j \text{Logn}(1.0 | \rho_{\mu W}^j, \sigma_{\mu W}^j), \quad (8.11)$$

where Logn is the log-normal distribution (as recommended by [81]):

$$\text{Logn}(x|\mu, \sigma) = \frac{1}{x\sqrt{2\pi\ln k}} \exp\left(-\frac{\ln^2\left(\frac{x}{\mu}\right)}{2\ln^2 k}\right); k = 1 + \sigma. \quad (8.12)$$

These terms are combined as:

$$L_{\text{EWK syst.}} = L_{\gamma \text{ syst.}} \times L_{\mu\mu \text{ syst.}} \times L_{\mu \text{ syst..}} \quad (8.13)$$

For $n_b \geq 2$ categories, the μ +jets control region is used to predict $Z \rightarrow \nu\bar{\nu}$ and ttW combined, giving:

$$r_\mu^{ri} = \frac{MC_\mu^i}{MC_{t\bar{t}+W+Z_{\text{inv}}}^i}; \quad (8.14)$$

$$L_\mu = \prod_i \text{Pois}(n_\mu^i | \rho_{\mu W}^j \cdot r_\mu^{ri} \cdot \text{EWK}^i + s_\mu^i). \quad (8.15)$$

Terms corresponding to the $\mu\mu$ +jets and γ +jets regions are subsequently dropped.

8.1.3 Signal Contribution

Let x be the cross section of the signal model under test, which can be varied according to a multiplicative factor f (a.k.a. the “mu-factor”), and l be the luminosity of the relevant collected data sample. ϵ_{had}^i and ϵ_μ^i are the signal acceptances of the hadronic and muon selections, respectively, for the given signal model. Finally, let δ be the relative systematic uncertainty on that signal acceptance, and ρ_{sig} be the corrective factor to the signal yield floated to accommodate this uncertainty. Therefore the yield of signal events for the hadronic region, s^i , and the yield of signal events in the muon region (i.e. “signal contamination”), s_μ^i , can be written as:

$$s^i = f \rho_{sig} x l \epsilon_{had}, \quad (8.16)$$

$$s_\mu^i = f \rho_{sig} x l \epsilon_\mu. \quad (8.17)$$

Furthermore, the signal systematic contribution to the likelihood is included as the term:

$$L_{signal} = \text{Logn}(1.0 | \rho_{sig}, \delta). \quad (8.18)$$

8.1.4 Total Likelihood

For a given analysis category k (n_b , n_{jet}), the total likelihood is constructed as:

$$L_{total}^k = L_{hadronic}^k \times L_\mu^k \times L_\gamma^k \times L_{\mu\mu}^k \times L_{\text{EWK syst.}}^k. \quad (8.19)$$

The number of nuisance parameters varies between different analysis categories, dependent on the number of H_T bins and control regions, as summarised in Table 8.1.

Table 8.1 Summary of likelihood nuisance parameters.

Description	Categories	Nuisance Parameters
11 H_T bins, $(\mu, \mu\mu, \gamma)$	$2 \leq n_{jet} \leq 3 / n_{jet} \geq 4$, $n_b = 0, 1$	$\{\text{EWK}^i, f_{Z\text{inv}}\}_{i=0}^{10}, \{\rho_{\gamma Z}^j\}_{j=3}^6$, $\{\rho_{\mu\mu Z}^j, \rho_{\mu W}^j\}_{j=0}^6$
8 H_T bins, (μ)	$2 \leq n_{jet} \leq 3 / n_{jet} \geq 4$, $n_b = 2, 3, \geq 4$	$\{\text{EWK}^i, f_{Z\text{inv}}\}_{i=0}^8, \{\rho_{\mu W Z}^j\}_{j=0}^6$
3 H_T bins, (μ)	$2 \leq n_{jet} \leq 3 / n_{jet} \geq 4$, $n_b = 2, 3, \geq 4$	$\{\text{EWK}^i\}_{i=0}^3, \{\rho_{\mu W Z}^j\}_{j=0}^3$

When considering signal an additional term is introduced:

$$L = L_{signal} \times \prod_k L_{total}^k. \quad (8.20)$$

8.2 Fit Results

The likelihood model described in Section 8.1 is used to relate the observations in the signal and control regions, accommodate the calculated background systematic uncertainties, and allow for the presence of any potential signal. In order to test the compatibility with a Standard Model only hypothesis, signal contribution is set to zero and the likelihood is maximized over all parameters using `Roofit` [82] and `MINUIT` [83], for each analysis category of n_b and n_{jet} .

Uncertainties are determined by performing a number of pseudo-experiments for each (n_b, n_{jet}) category and H_T bin, with the fit yields being entered into a histogram, using the 68 % quantiles as the fit uncertainties.

Two different procedures are used to determine fits to observations, as described in the following sections.

8.2.1 Fit without Signal region

An “a-priori” fit is made by considering only yields from the control regions, and not data observations in the hadronic signal region. The results of this fit are shown in Figures 8.2, 8.3, 8.4, 8.5, 8.6, 8.7, 8.8 and 8.9, and summarised in Table 8.2. As data observations from the signal region are not considered, it should be noted that the SM expectation is simply the result of the transfer factor method (described in Chapter 7). Due to this the SM expectation in the μ +jets control region is equal to the data observation in that region, as the fit is not influenced by observations from the signal region. Differences between the SM expectation and the data observations are found in the $\mu\mu$ +jets and γ +jets control region plots, due to the fit considering both control regions separately to predict the $Z \rightarrow \nu\bar{\nu}$ background component.

8.2.2 Fit with Signal region

An “a-posteriori” fit is made by considering every region, including the hadronic signal region observation in data, is shown in Figures 8.10, 8.11, 8.12, 8.13, 8.14, 8.15, 8.16 and 8.17, and summarised in Table 8.3. Good agreement between the SM expectation and data are seen throughout the various analysis categories, both in the signal and control regions. In this fit scenario, observations in the signal region are able to influence the fit result in the control regions. This is most noticeable in the $\mu\mu$ +jets and γ +jets regions, but only minimally in the μ +jets region where the much larger statistics of the control region dominate the fit.

Table 8.2 Summary of the “a-priori” fit. ‘SM’ entries represent the prediction of the full SM background, obtained from the fit procedure.

n_{jet}	n_b	200–275	275–325	325–375	375–475	475–575	H_T (GeV)	675–775	775–875	875–975	975–1075	1075–∞
2–3	0	SM	12412 ⁺³⁶⁹ ₋₄₁₂	5535 ⁺³³⁸ ₋₂₃₄	3331 ⁺¹²⁶ ₋₁₆₇	2400 ⁺¹²² ₋₉₄	663 ⁺³⁴ ₋₂₆	225 ⁺²¹ ₋₁₇	68.5 ^{+6.9} _{-6.7}	10.3 ^{+3.9} _{-3.0}	5.1 ^{+1.0} _{-1.1}	4.5 ^{+0.9} _{-0.9}
	0	Data	13090	5331	3354	2326	671	206	76	29	10	2
2–3	1	SM	1669 ⁺⁶⁵ ₋₆₇	853 ⁺⁵⁰ ₋₄₆	525 ⁺³⁷ ₋₂₄	391 ⁺²³ ₋₂₁	94.3 ^{+6.0} _{-5.6}	24.5 ^{+2.5} _{-3.6}	9.0 ^{+1.2} _{-1.4}	2.8 ^{+0.6} _{-0.8}	2.5 ^{+0.8} _{-0.9}	0.2 ^{+0.1} _{-0.1}
	1	Data	1733	833	527	356	90	31	6	4	1	1
2–3	2	SM	187 ⁺⁷ ₋₈	118 ⁺⁷ ₋₇	98.7 ^{+7.1} _{-7.0}	61.3 ^{+5.9} _{-5.5}	12.3 ^{+1.7} _{-1.0}	2.8 ^{+0.5} _{-0.6}	0.7 ^{+0.2} _{-0.2}	0.2 ^{+0.1} _{-0.1}	0.1 ^{+0.0} _{-0.0}	0
	2	Data	172	116	101	55	16	9	0	0	0	0
≥ 4	0	SM	108 ⁺¹⁰ ₋₁₂	497 ⁺³⁴ ₋₃₆	403 ⁺³⁶ ₋₃₃	327 ⁺²⁵ ₋₂₂	193 ⁺¹⁴ ₋₁₃	94.6 ^{+13.0} _{-10.7}	40.3 ^{+5.9} _{-4.4}	14.5 ^{+3.5} _{-2.4}	7.1 ^{+1.7} _{-1.4}	3.2 ^{+0.7} _{-1.0}
	0	Data	99	568	408	336	211	117	38	13	9	4
≥ 4	1	SM	39.2 ^{+3.0} _{-3.5}	215 ⁺¹² ₋₁₆	208 ⁺²⁴ ₋₂₂	150 ⁺¹⁵ ₋₁₁	75.8 ^{+7.8} _{-6.6}	28.6 ^{+3.8} _{-3.7}	10.3 ^{+2.1} _{-1.4}	5.1 ^{+1.3} _{-0.9}	2.0 ^{+0.7} _{-0.5}	0.8 ^{+0.4} _{-0.3}
	1	Data	38	195	210	159	83	33	7	10	4	1
≥ 4	2	SM	12.3 ^{+1.0} _{-1.0}	76.7 ^{+5.6} _{-5.2}	92.6 ^{+11.0} _{-9.3}	63.0 ^{+7.8} _{-5.7}	34.0 ^{+3.6} _{-3.4}	10.1 ^{+2.6} _{-1.8}	3.4 ^{+0.9} _{-0.6}	1.0 ^{+0.2} _{-0.2}	0.7 ^{+0.1} _{-0.2}	1
	2	Data	16	81	88	64	43	14	5	1	1	1
≥ 4	3	SM	1.1 ^{+0.2} _{-0.1}	8.2 ^{+0.6} _{-0.9}	11.1 ^{+2.0} _{-1.6}	7.4 ^{+1.1} _{-1.0}	4.0 ^{+0.5} _{-0.6}	1.1 ^{+0.3} _{-0.3}	0.4 ^{+0.2} _{-0.1}	0.1 ^{+0.1} _{-0.0}	0.1 ^{+0.0} _{-0.0}	0
	3	Data	0	7	5	5	6	1	1	0	0	0
≥ 4	≥ 4	SM	0.0 ^{+0.0} _{-0.0}	0.2 ^{+0.1} _{-0.1}	0.5 ^{+0.3} _{-0.3}	0.3 ^{+0.2} _{-0.2}	0	2				
	≥ 4	Data	0	0	0	0						

8.2 Fit Results

Table 8.3 Summary of the “a-posteriori” fit. ‘SM’ entries represent the prediction of the full SM background, obtained from the fit procedure.

n_{jet}	n_b		200–275	275–325	325–375	375–475	H_T (GeV)	575–675	675–775	775–875	875–975	975–1075	1075– ∞
2–3	0	SM	13034 $^{+89}_{-117}$	5348 $^{+85}_{-67}$	3351 $^{+56}_{-50}$	2351 $^{+38}_{-45}$	655 $^{+14}_{-11}$	218 $^{+12}_{-17}$	68.5 $^{+4.9}_{-4.8}$	27.2 $^{+3.0}_{-3.0}$	10.4 $^{+1.5}_{-1.6}$	5.6 $^{+1.0}_{-1.0}$	4.3 $^{+0.7}_{-1.0}$
	0	Data	13090	5331	3354	2326	671	206	76	29	10	9	2
2–3	1	SM	1711 $^{+37}_{-33}$	839 $^{+21}_{-25}$	526 $^{+20}_{-17}$	372 $^{+12}_{-14}$	90.6 $^{+5.1}_{-4.6}$	25.8 $^{+2.9}_{-2.6}$	8.7 $^{+0.8}_{-1.4}$	3.0 $^{+0.7}_{-0.6}$	2.2 $^{+0.8}_{-0.6}$	0.3 $^{+0.2}_{-0.1}$	0.2 $^{+0.1}_{-0.2}$
	1	Data	1733	833	527	356	90	31	6	4	1	0	1
2–3	2	SM	184 $^{+5}_{-7}$	117 $^{+7}_{-5}$	99.4 $^{+5.4}_{-4.6}$	60.2 $^{+3.5}_{-3.8}$	12.4 $^{+1.2}_{-1.0}$	3.3 $^{+0.6}_{-0.5}$	0.7 $^{+0.2}_{-0.2}$	0.2 $^{+0.1}_{-0.1}$	0.1 $^{+0.0}_{-0.0}$		
	2	Data	172	116	101	55	16	9	0	0	0	0	0
≥ 4	0	SM	104 $^{+6}_{-8}$	544 $^{+21}_{-18}$	407 $^{+18}_{-18}$	337 $^{+15}_{-10}$	202 $^{+10}_{-8}$	105 $^{+9}_{-7}$	42.5 $^{+4.5}_{-3.3}$	14.3 $^{+1.7}_{-2.5}$	7.5 $^{+1.4}_{-1.5}$	3.5 $^{+0.8}_{-0.8}$	3.4 $^{+1.0}_{-0.7}$
	0	Data	99	568	408	336	211	117	38	13	9	4	6
≥ 4	1	SM	38.9 $^{+2.2}_{-3.7}$	206 $^{+12}_{-10}$	209 $^{+13}_{-10}$	157 $^{+9}_{-9}$	79.3 $^{+5.2}_{-4.7}$	29.4 $^{+3.8}_{-2.2}$	9.9 $^{+1.9}_{-1.3}$	6.2 $^{+1.2}_{-1.1}$	2.3 $^{+0.7}_{-0.7}$	0.9 $^{+0.3}_{-0.3}$	0.9 $^{+0.3}_{-0.4}$
	1	Data	38	195	210	159	83	33	7	10	4	1	1
≥ 4	2	SM	12.5 $^{+1.0}_{-1.0}$	77.8 $^{+4.7}_{-4.6}$	90.2 $^{+9.0}_{-6.5}$	66.1 $^{+4.6}_{-4.8}$	36.3 $^{+3.4}_{-2.9}$	11.4 $^{+1.8}_{-1.9}$	3.9 $^{+0.8}_{-0.7}$	1.0 $^{+0.2}_{-0.3}$	0.7 $^{+0.1}_{-0.2}$		
	2	Data	16	81	88	64	43	14	5	1	1	1	1
≥ 4	3	SM	1.1 $^{+0.2}_{-0.2}$	8.1 $^{+0.9}_{-0.9}$	9.9 $^{+1.5}_{-1.3}$	7.2 $^{+0.9}_{-0.7}$	4.1 $^{+0.6}_{-0.6}$	1.1 $^{+0.3}_{-0.3}$	0.4 $^{+0.1}_{-0.1}$	0.1 $^{+0.1}_{-0.0}$	0.1 $^{+0.0}_{-0.0}$		
	3	Data	0	7	5	6	1	1	0	0	0	0	0
≥ 4	≥ 4	SM	0.0 $^{+0.0}_{-0.0}$	0.1 $^{+0.1}_{-0.1}$	0.4 $^{+0.2}_{-0.3}$	0.4 $^{+0.2}_{-0.2}$							
	≥ 4	Data	0	0	0	2							

8.2.3 Pulls and p-values

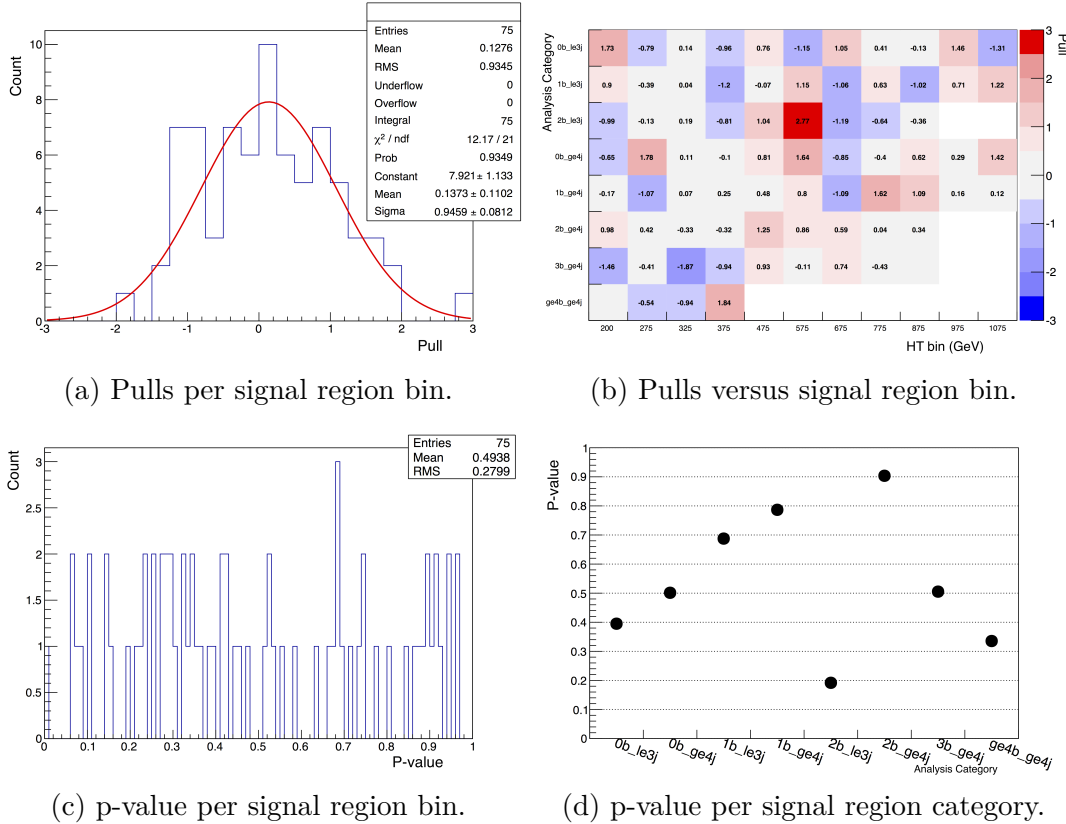


Fig. 8.1 Pulls for each analysis bin shown as a 1D distribution (Figure 8.1a) and as a function of the H_T bin and analysis category (n_{jet} , n_b) (Figure 8.1b). P-values for every analysis bin shown as a 1D distribution (Figure 8.1c) and for each analysis category, for an inclusive H_T range (Figure 8.1d).

The goodness-of-fit of the SM-only hypothesis is determined using a profile-likelihood method taken from [84]. The observed maximised likelihood value, L_{\max}^{data} , is used as a PDF to generate pseudo-experiments for which the likelihood is again maximised, with the new maximised value, L_{\max} , being noted. These values are entered into a histogram from which the L_{\max}^{data} quantile is taken, interpreted as the p-value and further converted into an observed significance, or pull. The p-values and pulls are summarised for various different analysis categories and individual H_T bins in the plots shown in Figure 8.1.

The 1D distribution of the pulls is shown in Figure 8.1a, with a Gaussian fit (red) indicating good Gaussian behaviour, with mean and sigma values statistically compatible with 0 and 1, respectively. Furthermore, the distribution of these pulls as

a function of the H_T bin and the analysis category (n_b , n_{jet}) is shown in Figure 8.1b to be randomly distributed, with no apparent pattern to a given region.

The distribution of p-values for every bin of H_T and analysis category can be seen in Figure 8.1c to be uniformly distributed between 0 and 1. The same information is shown in Figure 8.1d when a single p-value is calculated for an entire H_T range, for each analysis category, where the lowest value is 0.19.

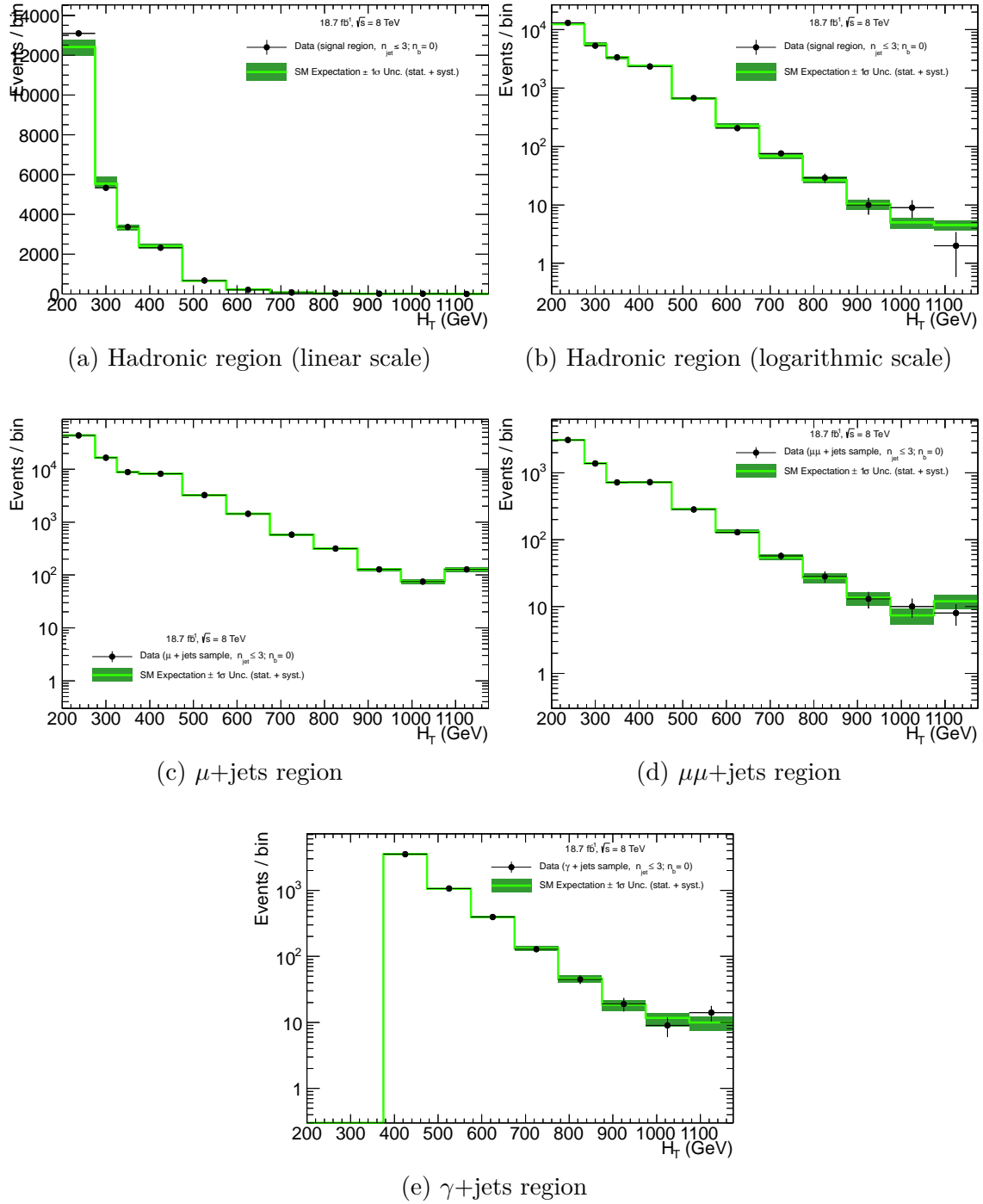


Fig. 8.2 Observations in data for the signal and control regions of the analysis, compared to the result of the full likelihood model simultaneous fit, when the hadronic data observations are not considered. The plots shown are for the $2 \leq n_{\text{jet}} \leq 3, n_b = 0$ analysis category.

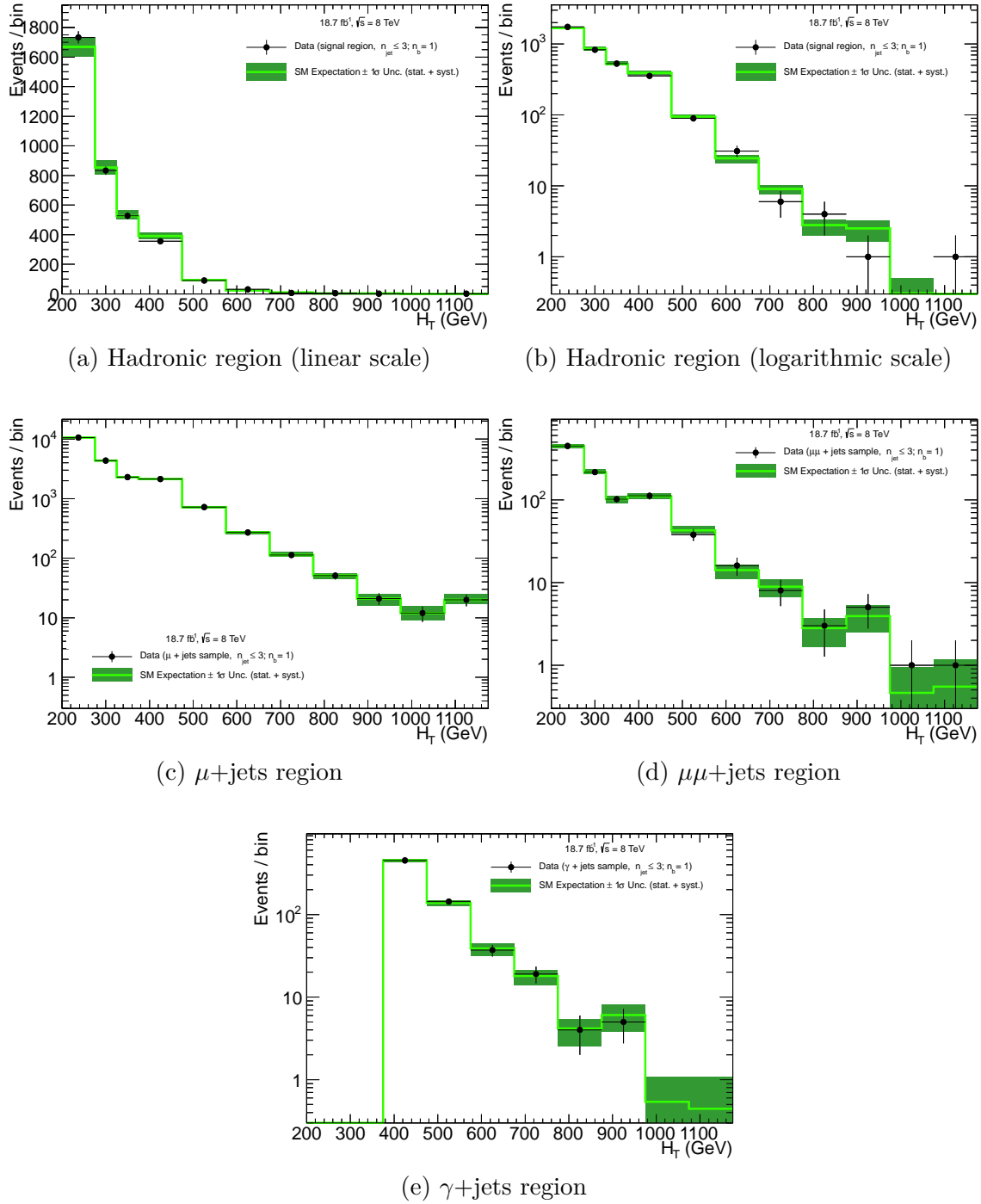


Fig. 8.3 Observations in data for the signal and control regions of the analysis, compared to the result of the full likelihood model simultaneous fit, when the hadronic data observations are not considered. The plots shown are for the $2 \leq n_{\text{jet}} \leq 3, n_b = 1$ analysis category.

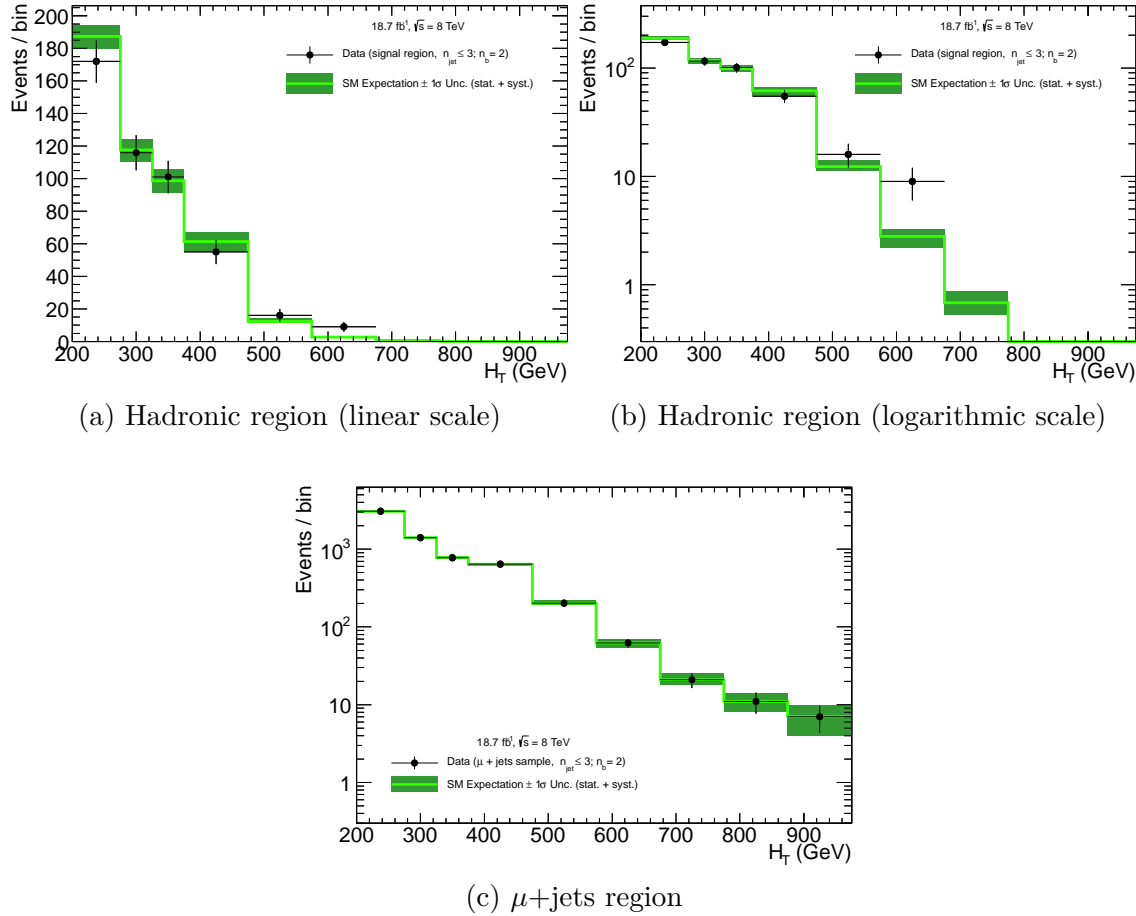


Fig. 8.4 Observations in data for the signal and control regions of the analysis, compared to the result of the full likelihood model simultaneous fit, when the hadronic data observations are not considered. The plots shown are for the $2 \leq n_{\text{jet}} \leq 3, n_b = 2$ analysis category.

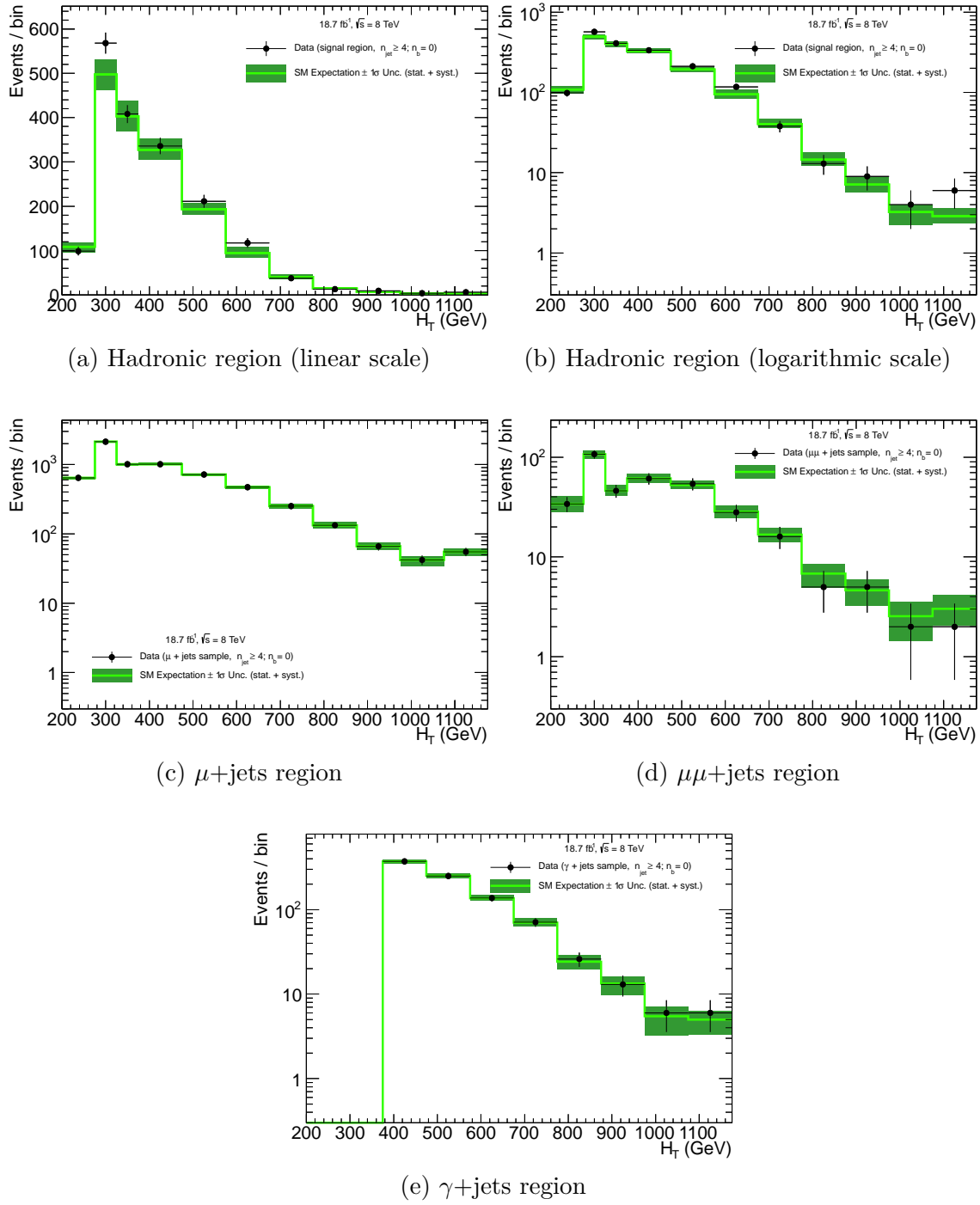


Fig. 8.5 Observations in data for the signal and control regions of the analysis, compared to the result of the full likelihood model simultaneous fit, when the hadronic data observations are not considered. The plots shown are for the $n_{\text{jet}} \geq 4, n_b = 0$ analysis category.

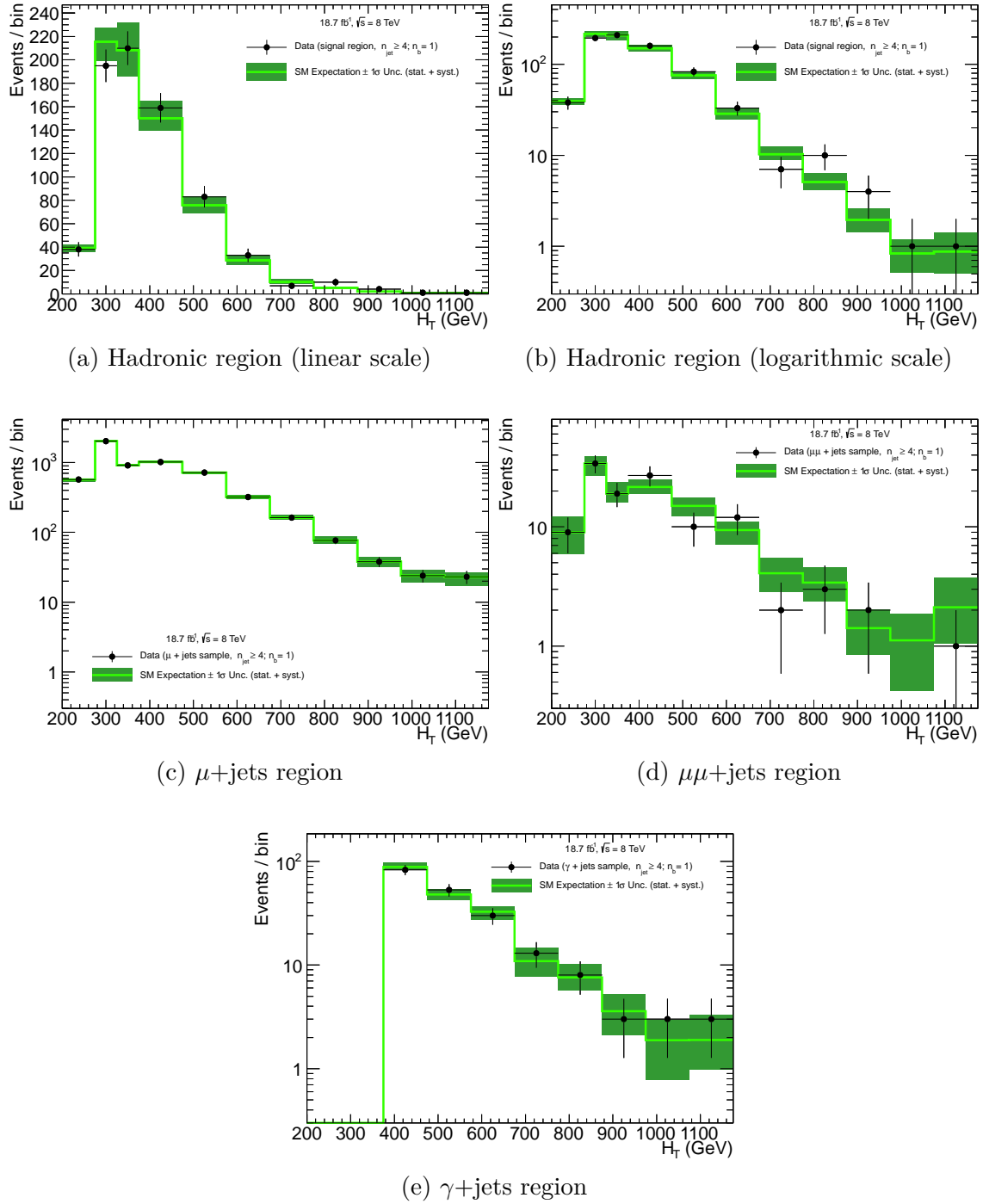


Fig. 8.6 Observations in data for the signal and control regions of the analysis, compared to the result of the full likelihood model simultaneous fit, when the hadronic data observations are not considered. The plots shown are for the $n_{\text{jet}} \geq 4$, $n_b = 1$ analysis category.

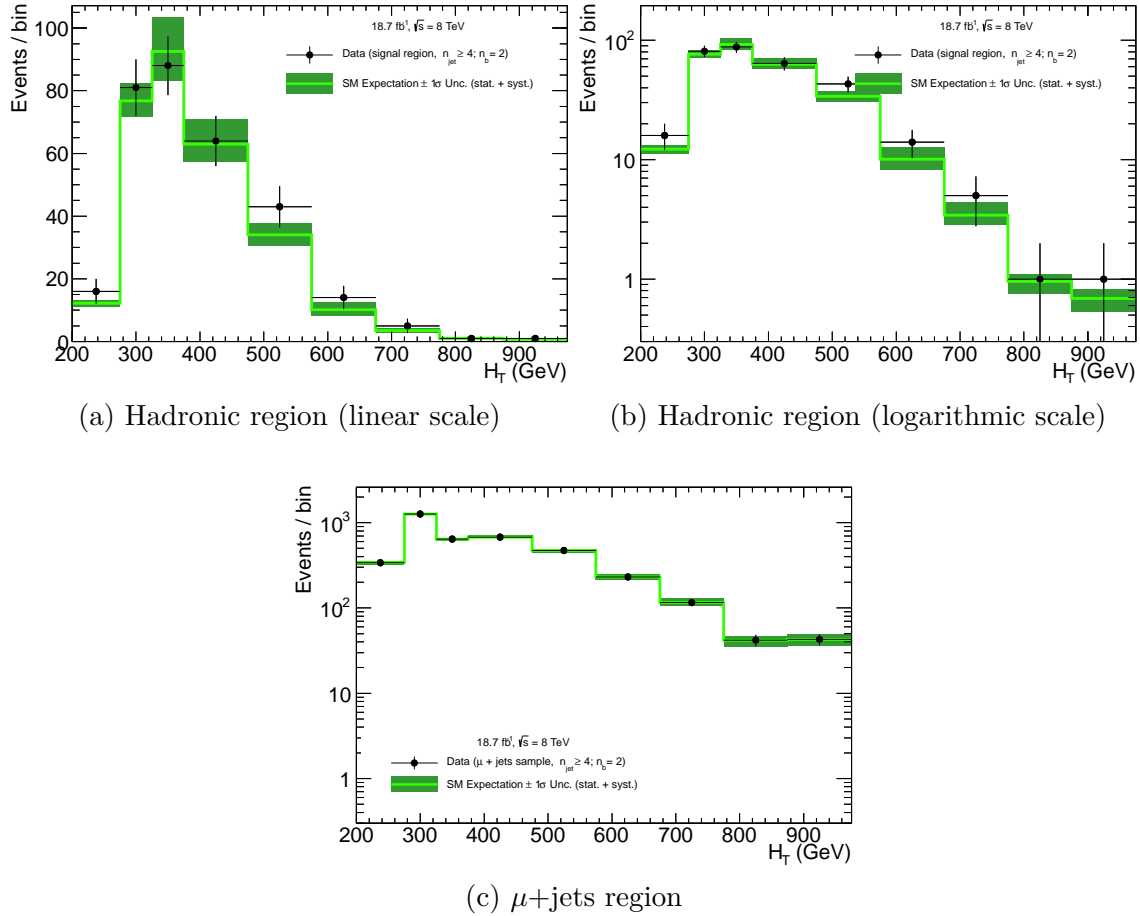


Fig. 8.7 Observations in data for the signal and control regions of the analysis, compared to the result of the full likelihood model simultaneous fit, when the hadronic data observations are not considered. The plots shown are for the $n_{\text{jet}} \geq 4$, $n_b = 2$ analysis category.

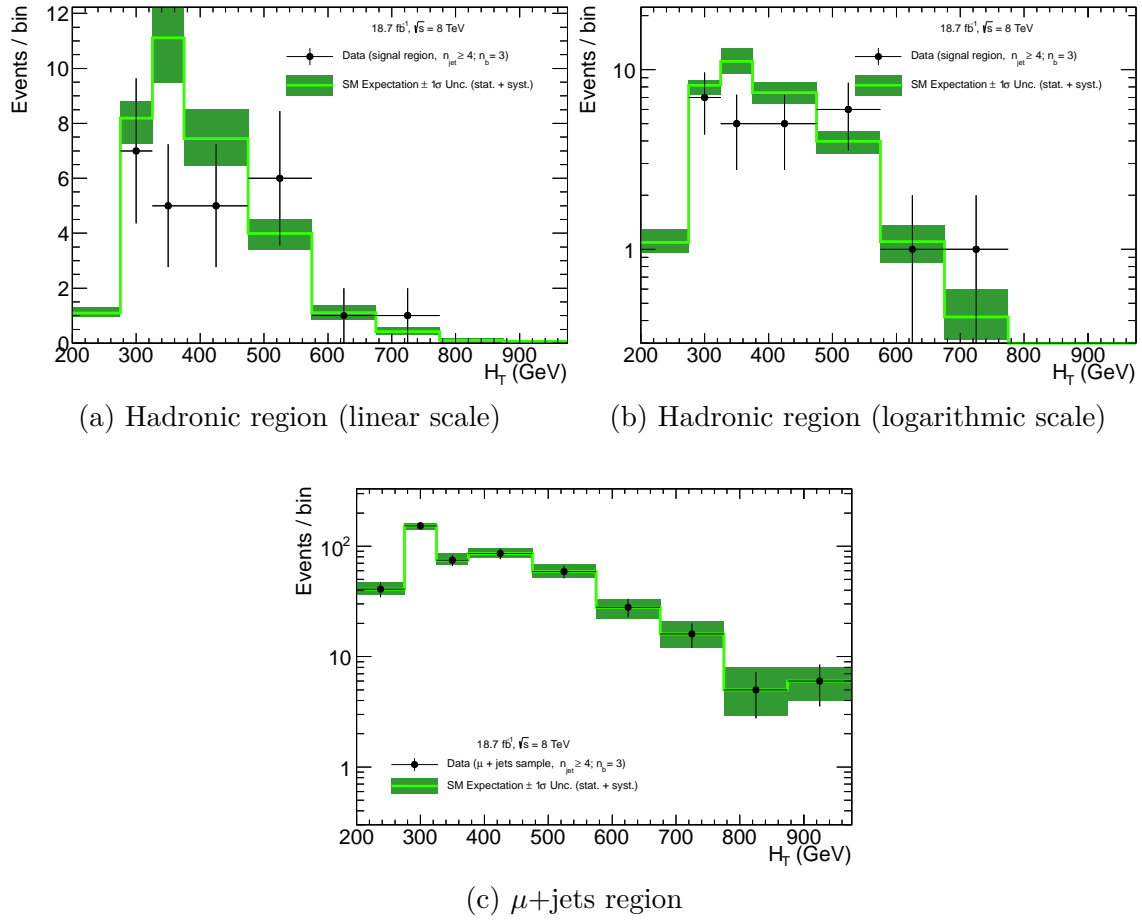


Fig. 8.8 Observations in data for the signal and control regions of the analysis, compared to the result of the full likelihood model simultaneous fit, when the hadronic data observations are not considered. The plots shown are for the $n_{\text{jet}} \geq 4$, $n_b = 3$ analysis category.

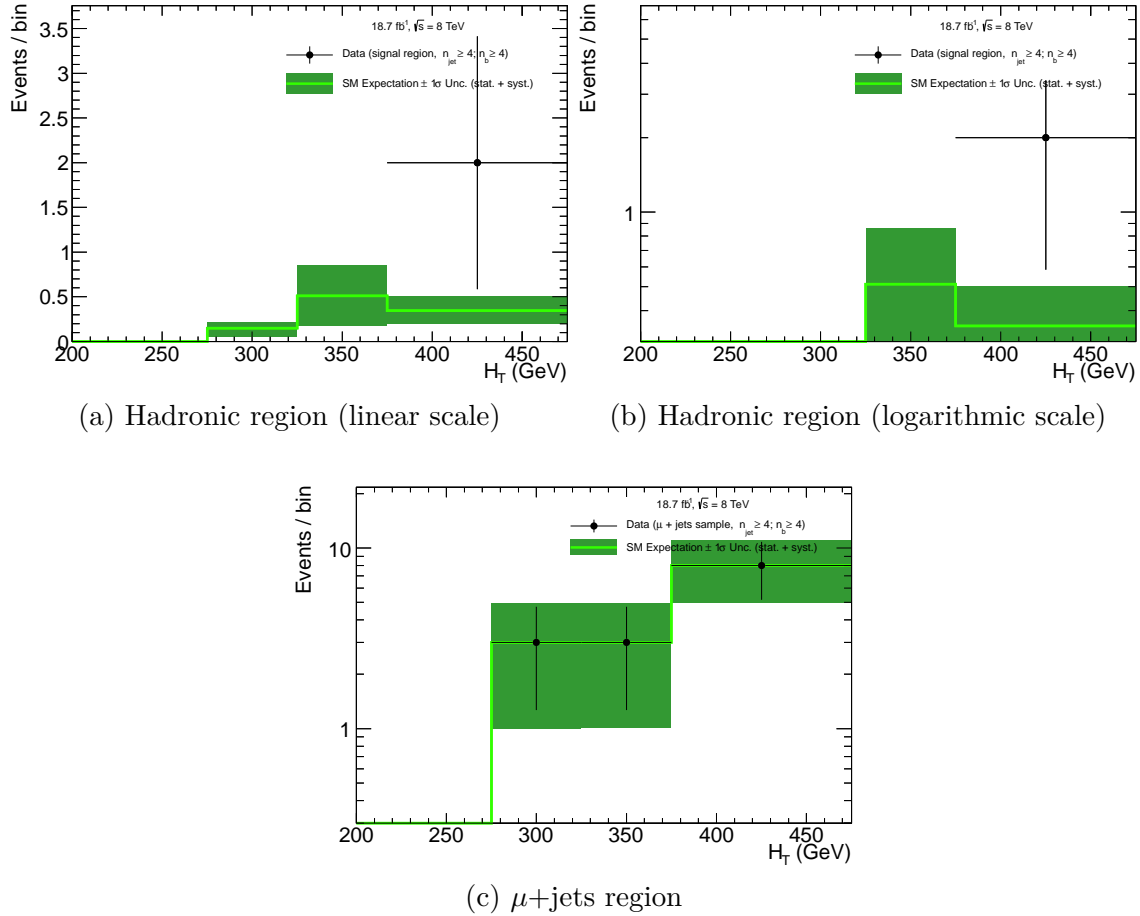


Fig. 8.9 Observations in data for the signal and control regions of the analysis, compared to the result of the full likelihood model simultaneous fit, when the hadronic data observations are not considered. The plots shown are for the $n_{\text{jet}} \geq 4$, $n_b \geq 4$ analysis category.

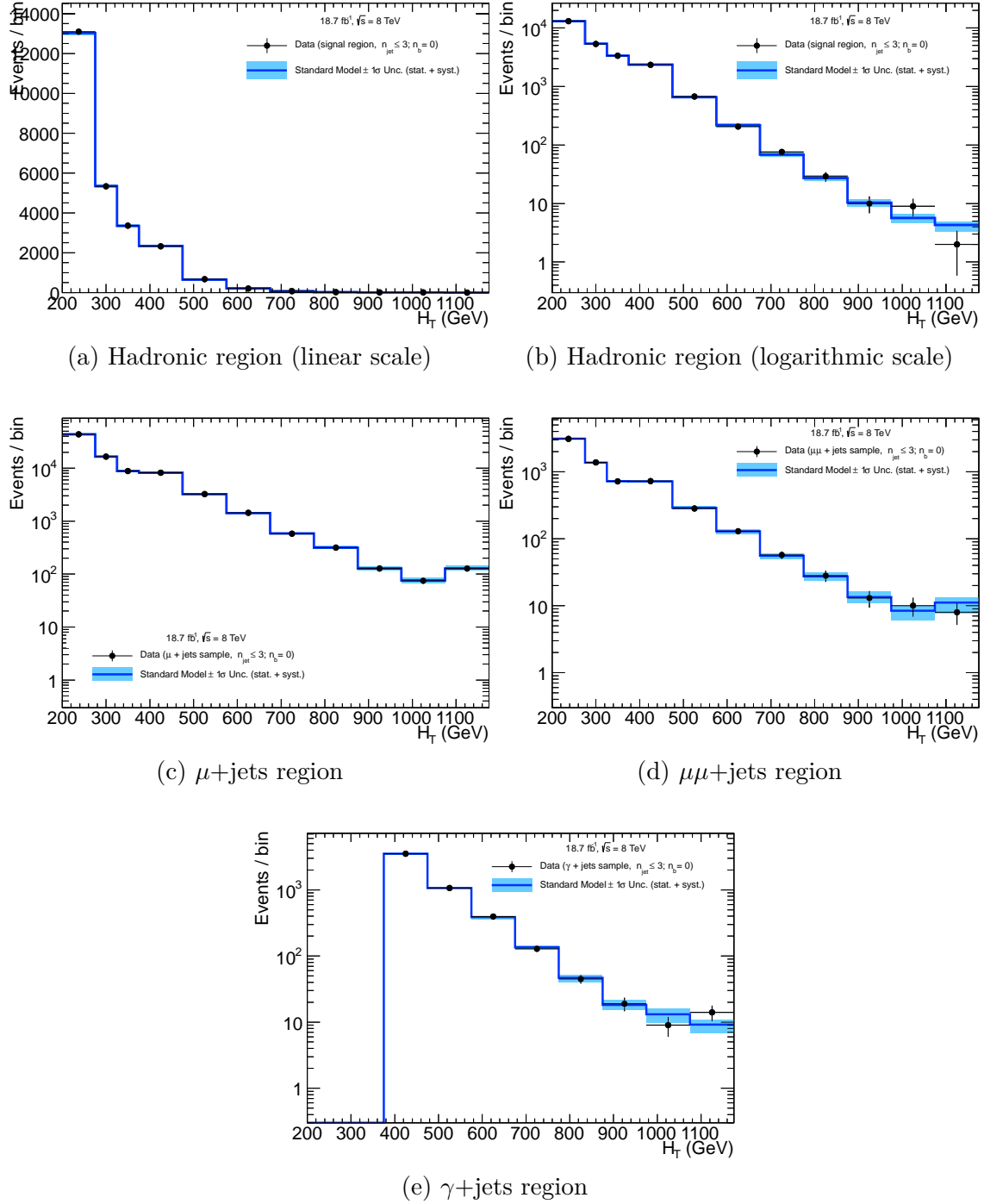


Fig. 8.10 Observations in data for the signal and control regions of the analysis, compared to the result of the full likelihood model simultaneous fit. The plots shown are for the $2 \leq n_{\text{jet}} \leq 3, n_b = 0$ analysis category.

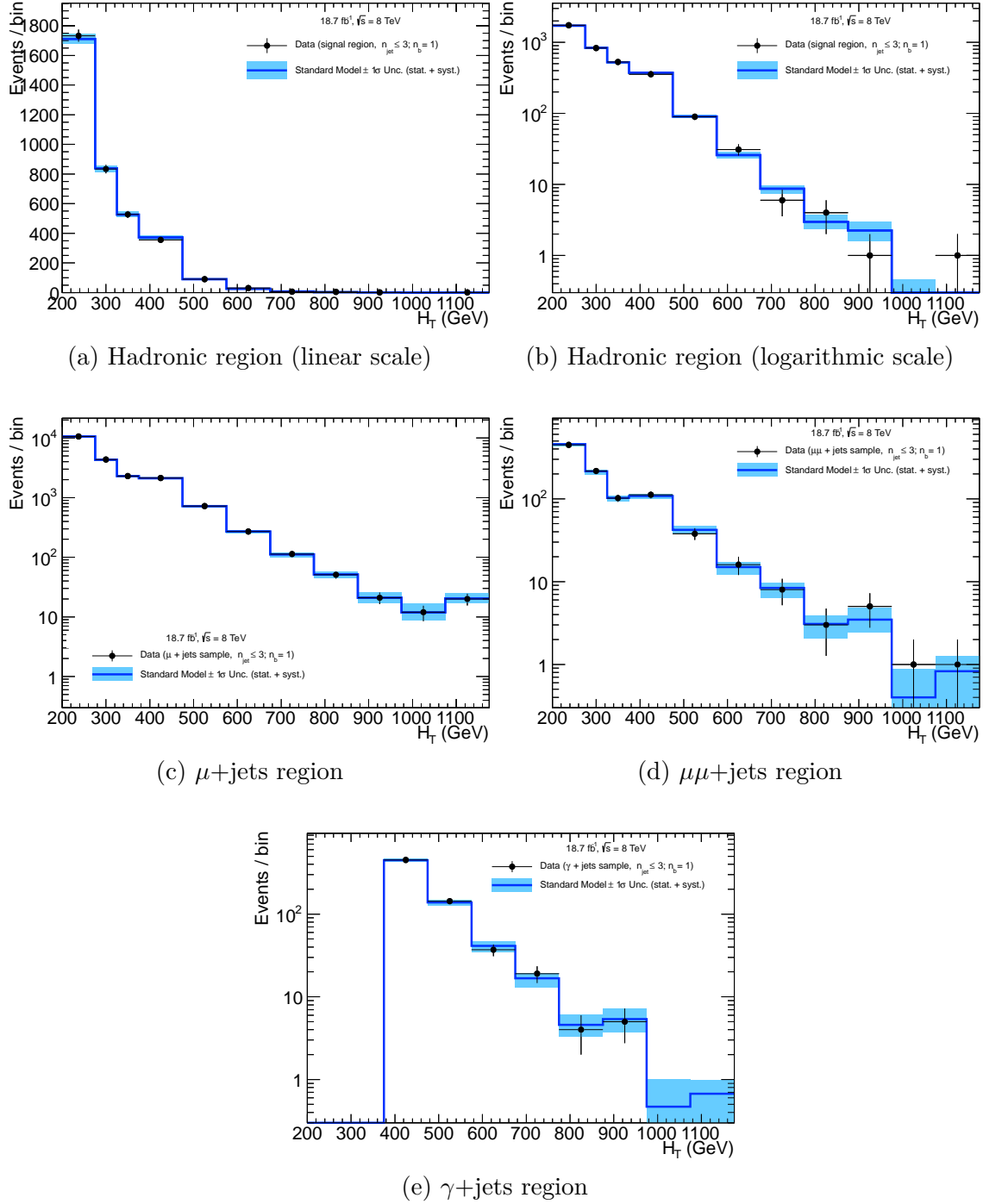


Fig. 8.11 Observations in data for the signal and control regions of the analysis, compared to the result of the full likelihood model simultaneous fit. The plots shown are for the $2 \leq n_{\text{jet}} \leq 3, n_b = 1$ analysis category.

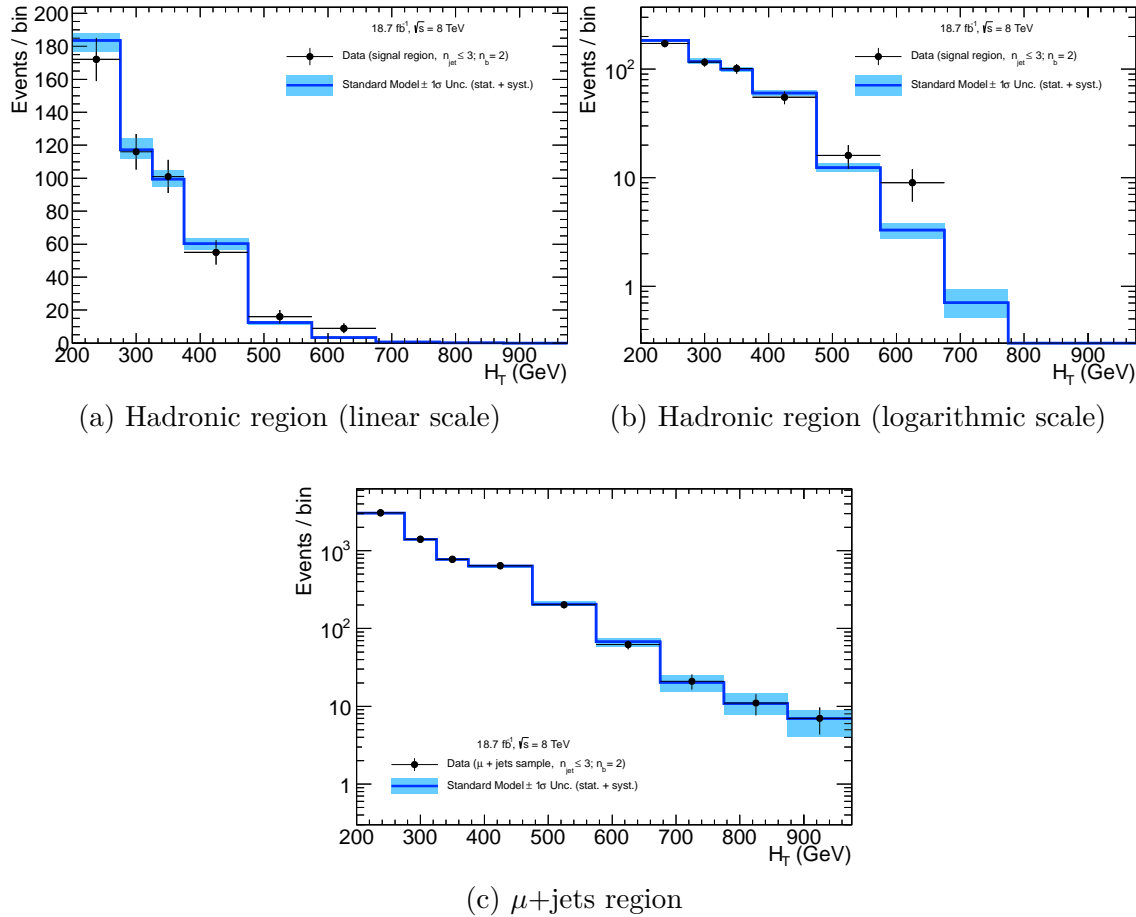


Fig. 8.12 Observations in data for the signal and control regions of the analysis, compared to the result of the full likelihood model simultaneous fit. The plots shown are for the $2 \leq n_{\text{jet}} \leq 3$, $n_b = 2$ analysis category.

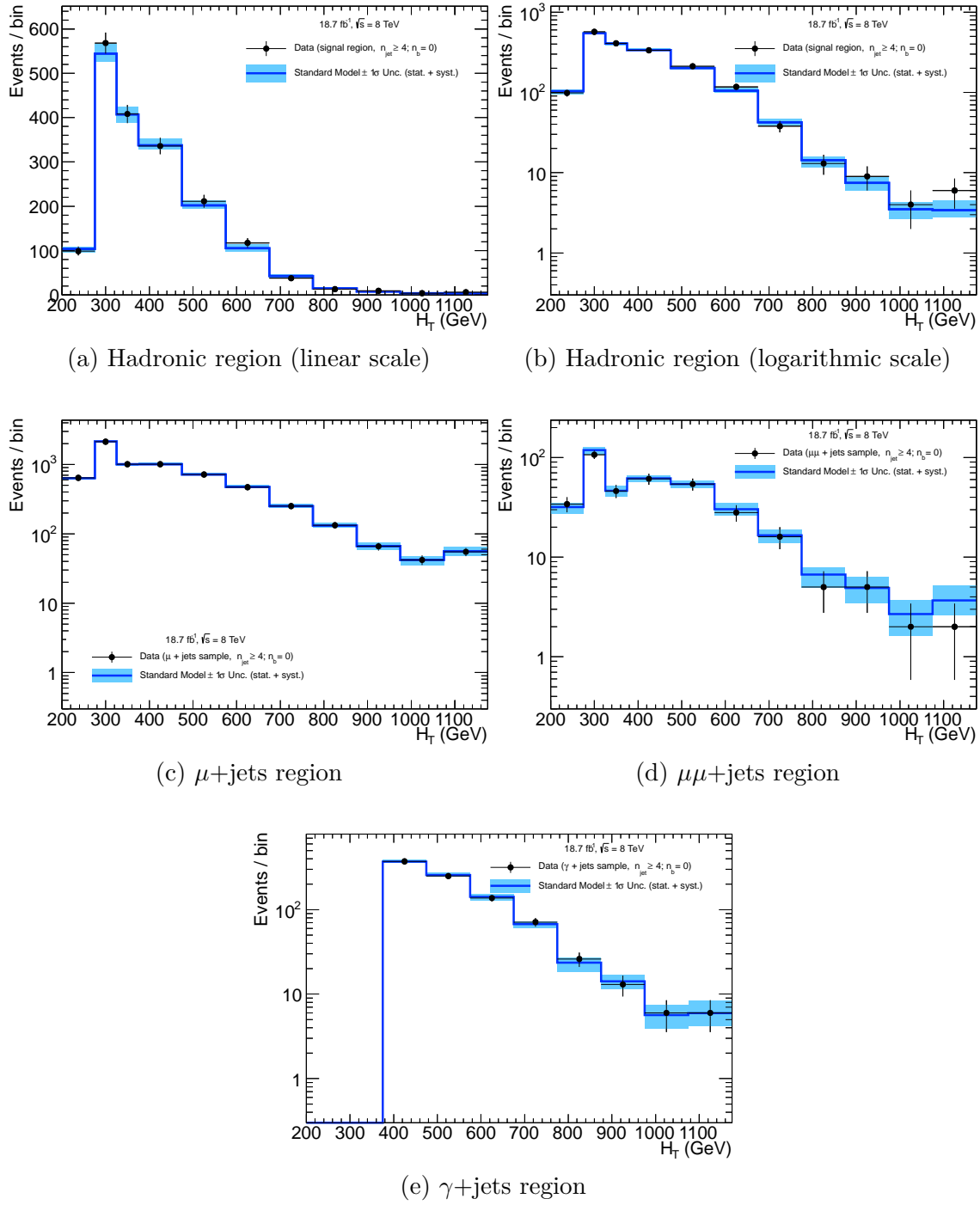


Fig. 8.13 Observations in data for the signal and control regions of the analysis, compared to the result of the full likelihood model simultaneous fit. The plots shown are for the $n_{\text{jet}} \geq 4, n_b = 0$ analysis category.

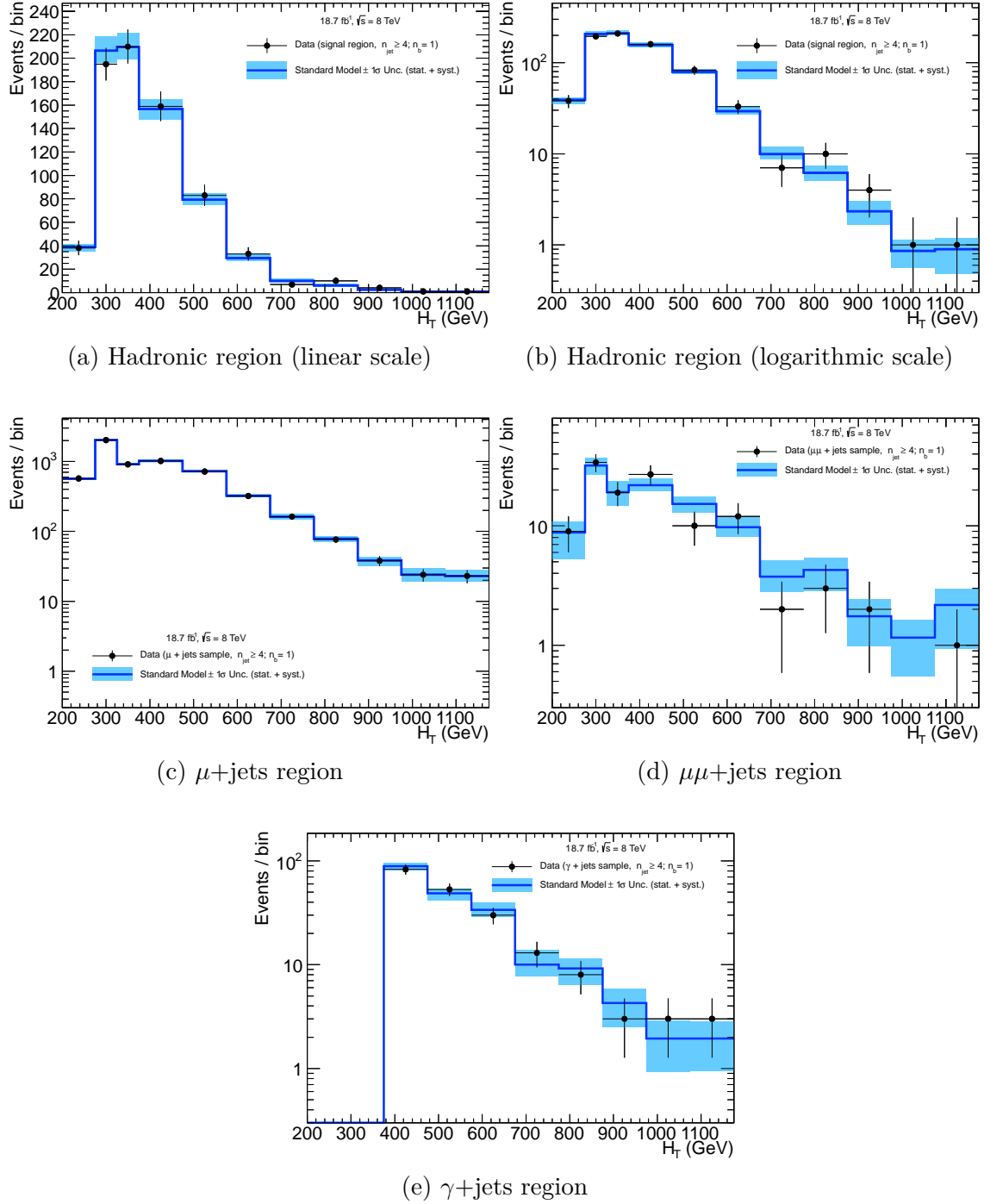


Fig. 8.14 Observations in data for the signal and control regions of the analysis, compared to the result of the full likelihood model simultaneous fit. The plots shown are for the $n_{\text{jet}} \geq 4$, $n_b = 1$ analysis category.

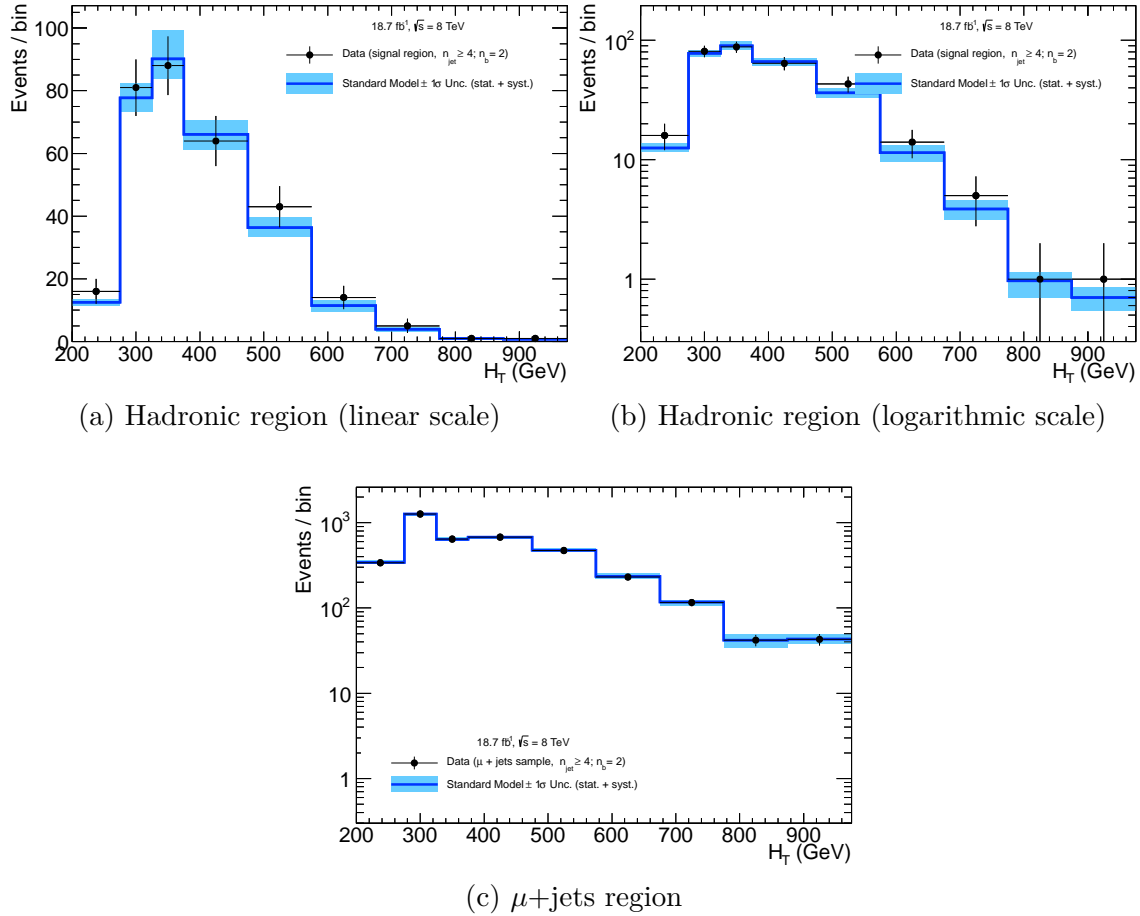


Fig. 8.15 Observations in data for the signal and control regions of the analysis, compared to the result of the full likelihood model simultaneous fit. The plots shown are for the $n_{\text{jet}} \geq 4$, $n_b = 2$ analysis category.

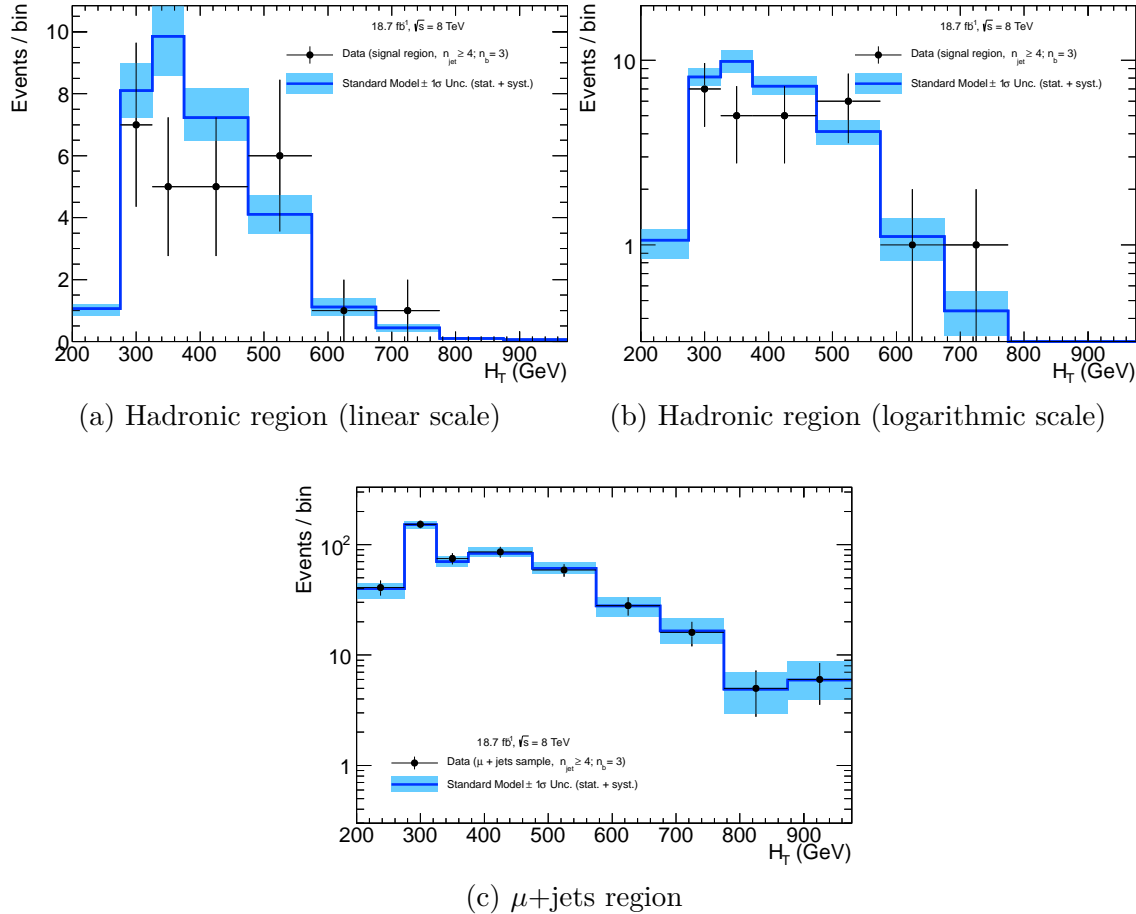


Fig. 8.16 Observations in data for the signal and control regions of the analysis, compared to the result of the full likelihood model simultaneous fit. The plots shown are for the $n_{jet} \geq 4$, $n_b = 3$ analysis category.

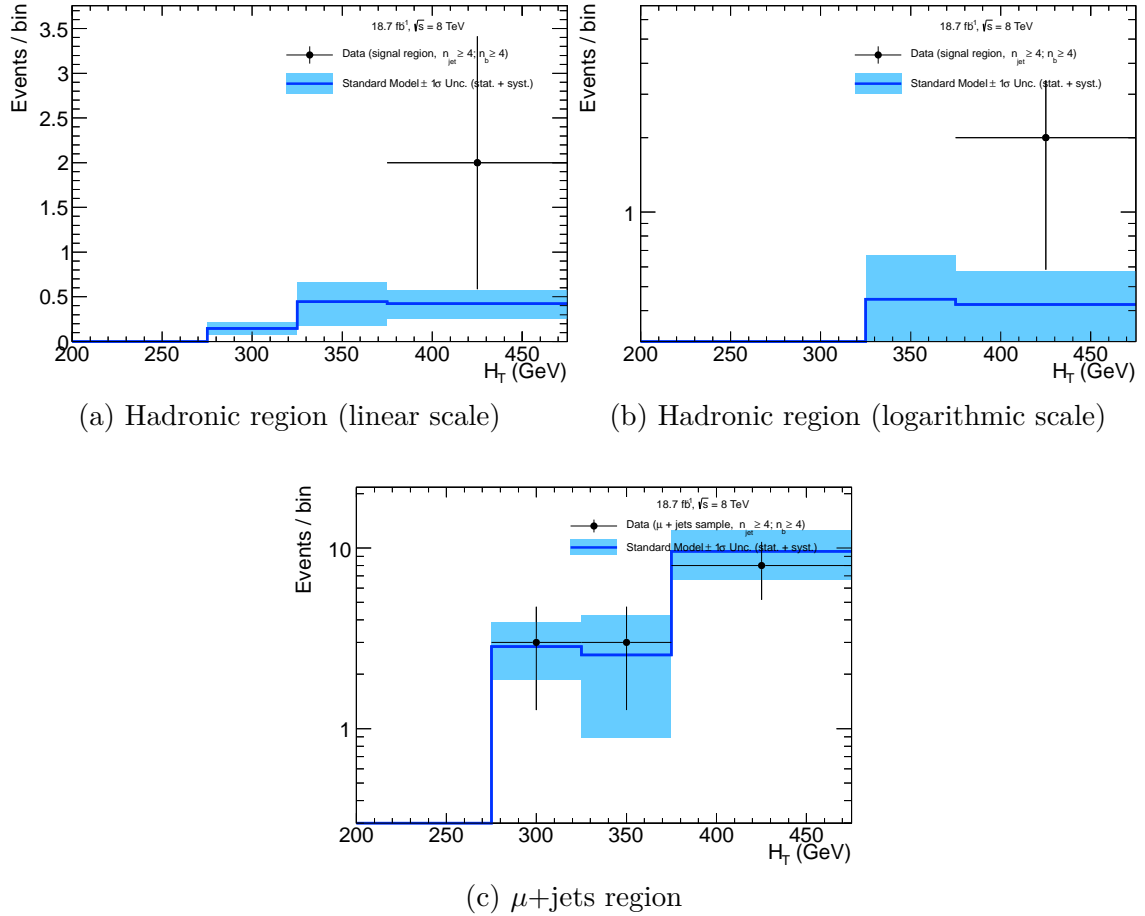


Fig. 8.17 Observations in data for the signal and control regions of the analysis, compared to the result of the full likelihood model simultaneous fit. The plots shown are for the $n_{jet} \geq 4, n_b \geq 4$ analysis category.

8.2.4 Summary

The ‘a-priori’ fit results described in Section 8.2.1 show the comparison of the data observations in the signal region with the expected SM background. This background prediction is made using the transfer factor technique described in Chapter 7. In general good agreement is observed, with only some bins deviating with pulls of up to 2.8 at the most. These bins appear to be uniformly distributed throughout the signal region, showing no particular signal-like structure. An analysis of the corresponding pulls and p-values, described in Section 8.2, indicate that all data observations are statistically in agreement with the SM background expectation, and that any deviations are compatible with statistical fluctuations.

Further to this, the ‘a-posteriori’ result described in Section 8.2.2, allows the fit model to consider observations in the hadronic signal region. By doing so, agreement further improves as the fit is able to accommodate the hadronic observations without tension. This is further evidence that data observations in the hadronic signal region are in agreement with the EWK background predictions, and therefore the SM-only hypothesis. It is concluded then that no statistically significant signal of BSM physics has been observed.

CHAPTER 9

INTERPRETATION

9.1 Signal Acceptance

Model acceptance is determined as a function of analysis category (n_b , n_{jet}) and H_T bin. This calculation is performed individually for each mass point in the scan plane for both the hadronic and muon selections (to determine signal contamination in the control region). Interpretations are made using a selected subset of the most sensitive analysis categories, but an inclusive H_T selection. The four most sensitive analysis categories are selected after an inspection of each categories expected limit reach. This is tested by setting data observations as equal to the result of the ‘a-priori’ fit, so as to not allow the signal observation in data to influence the result.

9.1.1 Charm decay

Signal efficiency times acceptance for the charm decay model, $pp \rightarrow \tilde{t}\tilde{t}^* \rightarrow c\tilde{\chi}^0 \bar{c}\tilde{\chi}^0$, is shown in Figure 9.1 for the four categories with the greatest sensitivity. The largest acceptance is seen in the $2 \leq n_{jet} \leq 3$, $n_b = 0$ analysis category (Figure 9.1a), where efficiencies are around the percent level. At small mass splittings, nearest the kinematically inaccessible region above the diagonal, acceptance is due to hard initial state radiation (ISR) jets balancing a soft SUSY decay system. Small mass splittings imply little energy being available for decay products to gain sufficient momentum to be within acceptance, and therefore become invisible to the analysis. In order for such an event to pass the selection criteria of the signal region, hard ISR jets are required to be within kinematic acceptance and boosting this decay system.

Moving away from the diagonal to increasing values of Δm indicates a drop in acceptance, eventually leading to an increase due to a competing effect from the increase

in available kinematic phase space. Far from the diagonal, decay products are able to gain sufficient momentum to enter acceptance and become visible. There is still a dependence on ISR jets boosting this system, however crucially jets originating from charm quarks can now be observed. Contributions to acceptance therefore increase not only for this $n_b = 0$ category, but similarly for $n_b = 1$ categories, due to mistagging of the visible charm jets, where lower acceptance is observed at small Δm .

Finally, increased acceptance is observed in the $n_{\text{jet}} \geq 4$ categories, predominantly away from the diagonal. Again, given the increased kinematic phase space of the larger mass splitting scenarios, more jets are above the analysis threshold and therefore visible.

Signal contamination in the $\mu + \text{jets}$ selection is shown to be negligible, given the lack of leptons in the final state.

Example cut-flows from the signal region are shown in Table 9.1 for two mass points with the extremal Δm values of the scan, both for values of $m_{\tilde{t}}$ near the limits of sensitivity.

Table 9.1 Cutflow table for two mass points ($m_{\tilde{t}} = 250$ GeV, $m_{\tilde{\chi}^0} = 240$ GeV and $m_{\tilde{t}} = 250$ GeV, $m_{\tilde{\chi}^0} = 170$ GeV) of the charm decay signal model. The selection represents the hadronic signal region for the $H_T > 375$ GeV region.

Cut Name ($m_{\tilde{t}}, m_{\tilde{\chi}^0}$)	Cumulative Eff. (%)	
	(250, 240)	(250, 170)
Event Counter	100.00	100.00
$n_{\text{jet}} \geq 2$	12.99	59.52
MET Filters	12.99	59.52
Vertex Noise Filter	12.99	59.52
DeadECAL Filter	10.77	43.88
$n_e = 0$	10.77	43.88
$n_\gamma = 0$	10.77	43.7
$n_\mu = 0$	10.77	43.7
EMF_{\max} for all jets > 0.1	10.77	43.7
Leading jet $p_T > 100$ GeV	7.37	24.79
Leading jet $\eta < 2.5$	7.04	24.21
Sub-Leading jet $p_T > 100$ GeV	2.31	8.92
$n_{j,fail} = 0$	2.26	8.66
$\Delta R(\mu_{fail}^i, jet^j) < 0.5$	2.26	8.65
$n_{SIT} = 0$	2.09	8.03
$\Delta\phi_{min}^* > 0.3$	1.84	5.42
$\cancel{H}_T/\cancel{E}_T < 1.25$	1.68	4.46
$H_T > 375$ GeV	0.90	2.05
$\alpha_T > 0.55$	0.45	0.40
$\cancel{H}_T/\cancel{E}_T < 1.25$	0.45	0.40

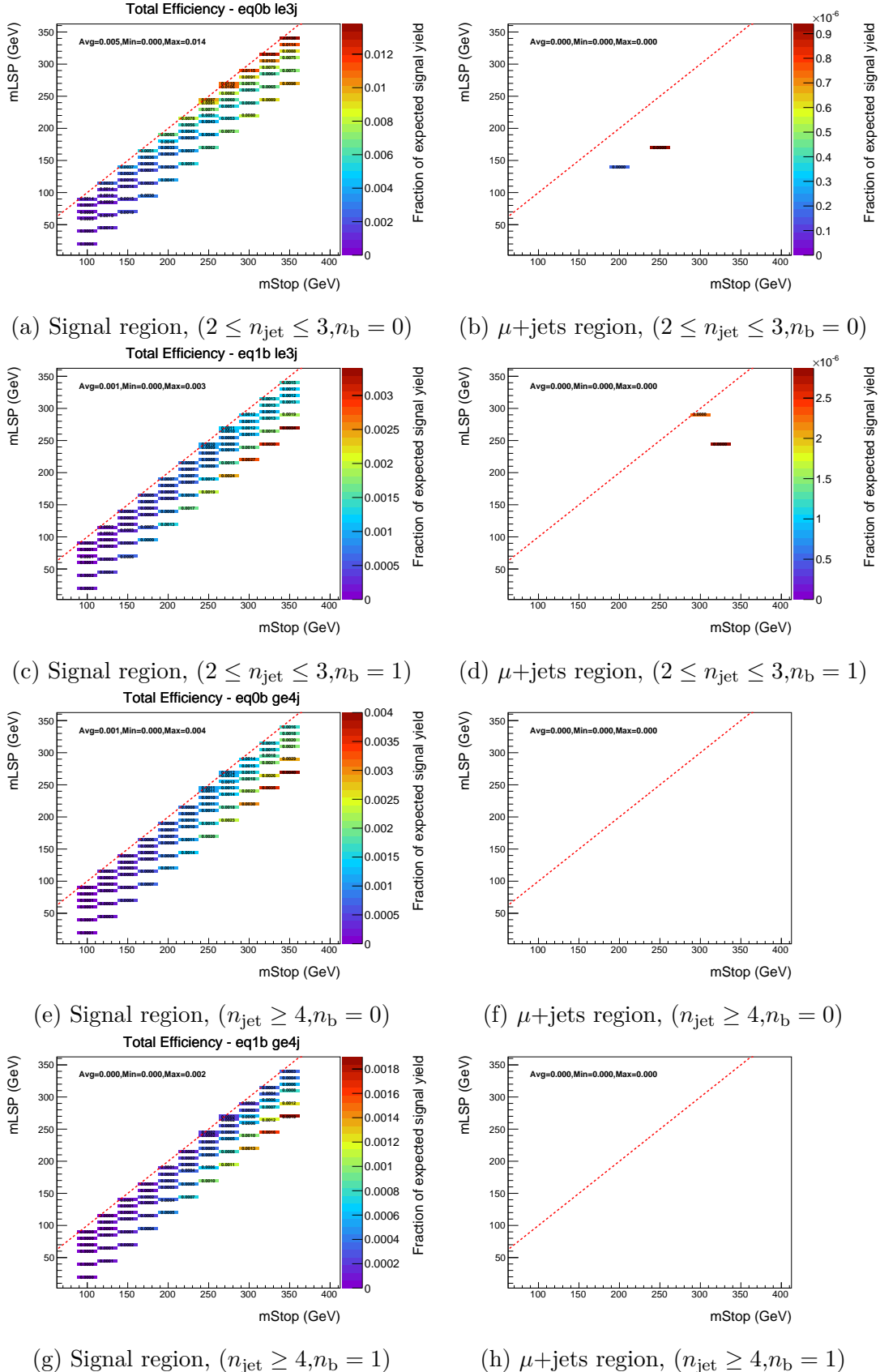


Fig. 9.1 Signal efficiency times acceptance of the $\text{pp} \rightarrow \tilde{t}\tilde{t}^* \rightarrow c\chi_0^0 \bar{c}\chi_0^0$ simplified model, for the hadronic selection (left) and the $\mu + \text{jets}$ selection (right), shown for the four most sensitive analysis categories with an inclusive selection on H_T .

9.1.2 Four-body decay

The signal efficiency times acceptance distributions for the four-body model, $\text{pp} \rightarrow \tilde{t}\tilde{t}^* \rightarrow bff'\tilde{\chi}^0 bff'\tilde{\chi}^0$, are shown in Figure 9.2 in the four most sensitive analysis categories. The plots show inclusive H_T selections, both for the hadronic and $\mu+\text{jets}$ selections. There are strong similarities with the acceptance profiles shown earlier for the charm decay model, both in magnitude and distribution about the plane. At small values of Δm , given that the entire SUSY decay system becomes invisible due to a lack of available kinematic phase space, both models show very similar efficiencies, where acceptance is almost entirely due to hard ISR jets. There is a significant difference however, when a b-tagged jet is required, for example in the $2 \leq n_{\text{jet}} \leq 3$, $n_b = 1$ category (Figure 9.2c), where the presence of a jet originating from a real b quark improves acceptance, particularly away from the diagonal where the jet is more likely to pass analysis thresholds. Less significant are the efficiencies seen in the $n_{\text{jet}} \geq 4$ categories, given the larger number of final state objects, each requiring a share of the energy originating from the mass splitting of the mother and daughter sparticles.

Table 9.2 Cutflow table for two mass points ($m_{\tilde{t}} = 250$ GeV, $m_{\tilde{\chi}^0} = 240$ GeV and $m_{\tilde{t}} = 250$ GeV, $m_{\tilde{\chi}^0} = 170$ GeV) of the four-body decay signal model. The selection represents the hadronic signal region for the $H_T > 375$ GeV region.

Cut Name ($m_{\tilde{t}}, m_{\tilde{\chi}^0}$)	Cumulative Eff. (%)	
	(250, 240)	(250, 170)
Event Counter	100.00	100.00
$n_{\text{jet}} \geq 2$	10.80	32.33
MET Filters	10.80	32.33
Vertex Noise Filter	10.80	32.33
DeadECAL Filter	9.13	21.30
$n_e = 0$	9.13	19.70
$n_\gamma = 0$	9.13	19.55
$n_\mu = 0$	9.13	17.41
EMF_{\max} for all jets > 0.1	9.13	17.41
Leading jet $p_T > 100$ GeV	6.01	8.70
Leading jet $\eta < 2.5$	5.70	8.37
Sub-Leading jet $p_T > 100$ GeV	1.64	2.23
$n_{j,\text{fail}} = 0$	1.61	2.17
$\Delta R(\mu_{\text{fail}}^i, \text{jet}^j) < 0.5$	1.61	2.11
$n_{SIT} = 0$	1.50	1.67
$\Delta\phi_{\min}^* > 0.3$	1.35	0.93
$\cancel{H}_T/\cancel{E}_T < 1.25$	1.24	0.68
$H_T > 375$ GeV	0.55	0.37
$\alpha_T > 0.55$	0.26	0.08
$\cancel{H}_T/\cancel{E}_T < 1.25$	0.26	0.08

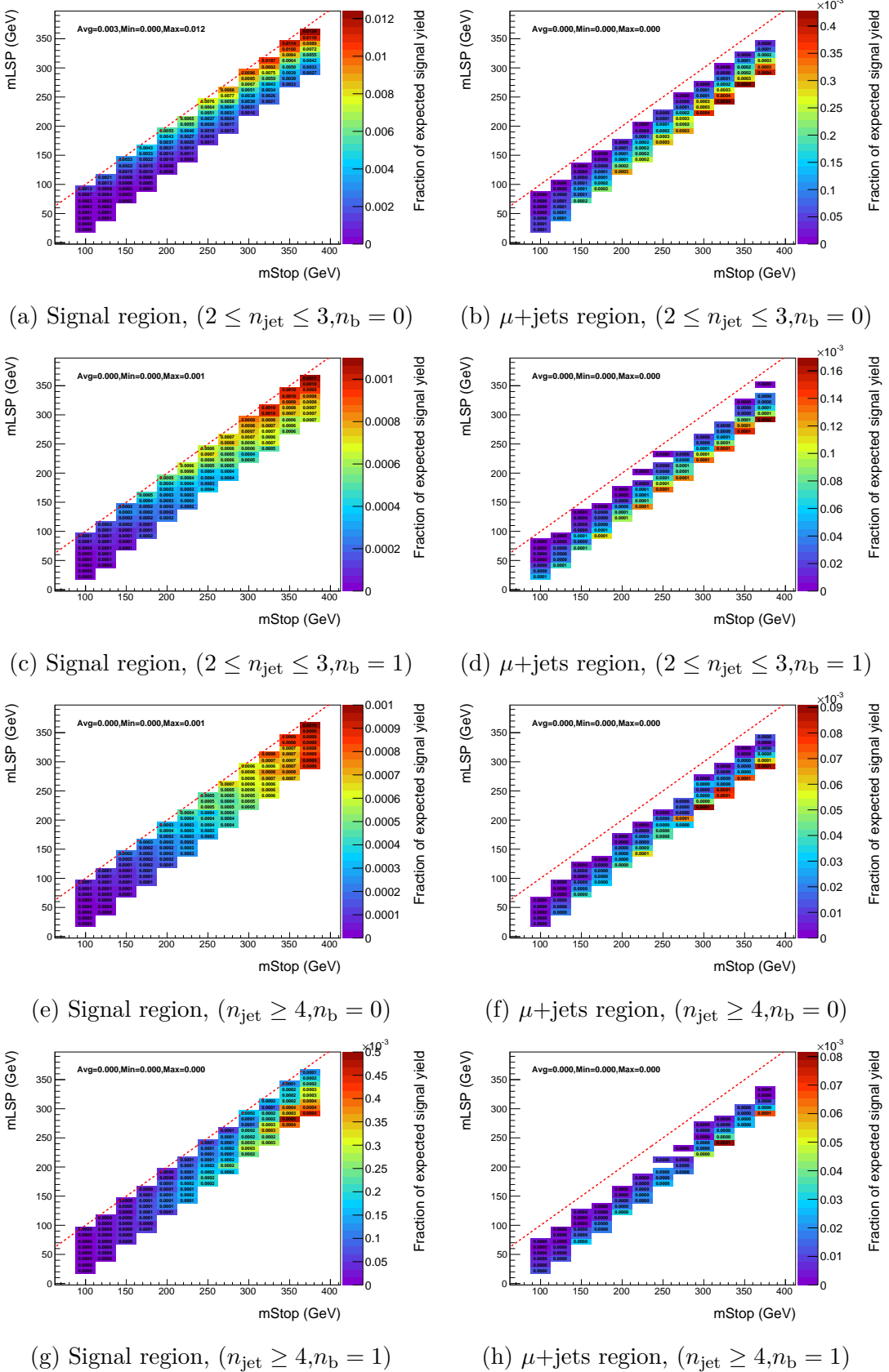


Fig. 9.2 Signal efficiency times acceptance of the $\text{pp} \rightarrow \tilde{t}\tilde{t}^* \rightarrow bff'\chi^0 bff'\chi^0$ simplified model, for the hadronic selection (left) and the $\mu + \text{jets}$ selection (right), shown for the four most sensitive analysis categories with an inclusive selection on H_T .

Also of note is the increase in signal contamination observed in the μ +jets selection, due to the presence of $f\bar{f}$ in the decay chain, potentially introducing leptons to the final state.

Example cut-flows from the signal region are shown in Table 9.2 for two mass points with extremal Δm , at an $m_{\tilde{t}}$ value near the limit of sensitivity.

9.1.3 ISR Corrections to compressed spectra MC signal samples

Given the reliance of such compressed spectra models on ISR jets for acceptance, a dedicated study was performed within the SUSY Physics Analysis Group (*PAG*) into the accuracy of its modelling and relevant systematic uncertainties [85].

A comparison of data to MC for a pure, high-statistics selection of Z boson production with associated jets, where the Z decays to an opposite-sign, same-flavour (OSSF) lepton pair, $Z \rightarrow l\bar{l}$. By tagging the leptons in the event, remaining jets can be considered as an ISR jet “recoil system” against that of the Z boson decay. Comparisons of data to MC for both the vectorial sum of the lepton \vec{p}_T ’s and the recoil jet system’s \vec{p}_T indicate an over-estimation in MC as a function of the system’s p_T , of up to 20% in high p_T scenarios, shown in Figure 9.3.

Correction factors for MADGRAPH based samples, dependent on the p_T of the jet system, can therefore be derived by extracting the ratio of data to MC. These values

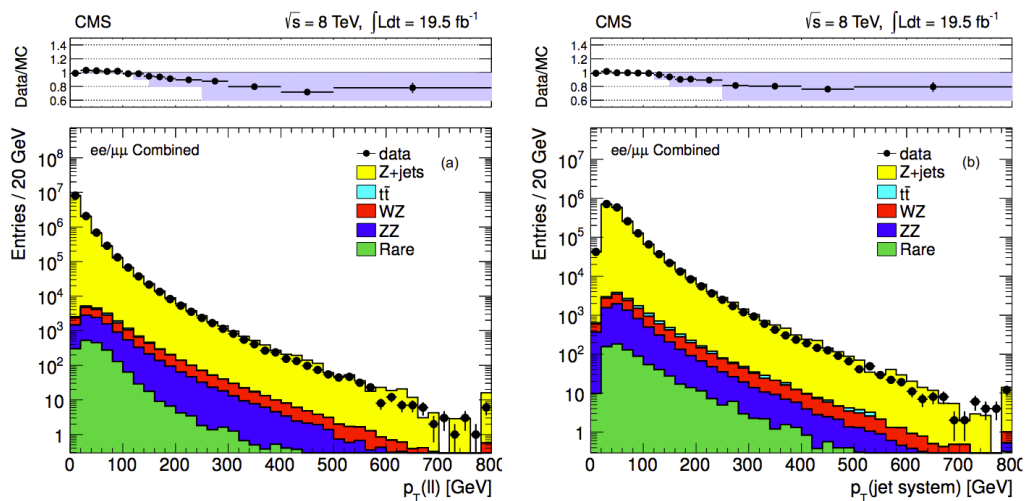


Fig. 9.3 Data to MC comparisons for an enriched $Z \rightarrow l\bar{l}$ selection, with the vectorial sum of lepton p_T ’s (left) and of the recoil jets (right) [85].

are summarised in Table 9.3. Weights are applied to both the charm and four-body decay signal samples at the event level, where the event’s boost p_T is determined by calculating the vectorial sum of the two, pair-produced generator level \tilde{t} particles.

Table 9.3 Correction factors for MADGRAPH based signal samples to account for MC over-prediction of ISR.

boost p_T (GeV)	Correction Factor
$0 < p_T \leq 120$	1.00
$120 < p_T \leq 150$	0.95
$150 < p_T \leq 250$	0.90
$250 < p_T$	0.80

9.2 Systematic Uncertainties on Signal Acceptance

A range of sources of systematic uncertainty on the acceptance times signal efficiency are considered for each signal model. The main sources, namely jet energy scale (JES), initial state radiation (ISR), b tag scale factors, parton distribution function (PDF), the H_T/\mathbb{E}_T cut and the dead ECAL filter, have systematic values determined per point in the scan plane, as a function of H_T , n_b and n_{jet} . The remaining systematics are applied as a flat contribution across the entire plane, considered as a conservative approach.

Although signal systematics are considered in the likelihood model as a function of the H_T dimension of the analysis, all results discussed here are representative of an inclusive selection of $H_T > 200$ GeV.

9.2.1 Jet Energy scale

The acceptance times signal efficiency is tested for sensitivity to jet energies by measuring its sensitivity to upwards and downwards variations of all jet energies by the p_T and η -dependent jet energy scale (JES) uncertainty, as prescribed by the JetMET *POG*. Ultimately the number of events that fall in or out of acceptance across the analysis is being tested, and as such the inclusive analysis category of $n_{jet} \geq 2$ and $n_b \geq 0$ is used to determine a systematic which is applied to all individual analysis categories.

Distributions showing the acceptance changes due to the variations in JES are shown in Appendix A for both signal models. Systematics are typically on the order of a 5–10% for both models.

9.2.2 Initial State Radiation

As described in Section 9.1.3, boost- p_T dependent event weights are taken from the study performed within the SUSY *PAG*. A procedure is also defined to determine related systematics, by applying upwards and downwards variations of weights corresponding to the magnitude of the corrections themselves, and studying the effect on signal efficiency times acceptance. These weights are summarised in Table 9.4.

Table 9.4 Systematic factors for MADGRAPH based signal samples to determine ISR modelling related systematics.

$p_{T\text{boost}}$ (GeV)	Systematic Variation
$0 < p_T \leq 120$	± 0.0
$120 < p_T \leq 150$	± 0.05
$150 < p_T \leq 250$	± 0.10
$250 < p_T$	± 0.20

As discussed previously in sections 9.1.1 and 9.1.2, acceptance for compressed spectra models at the smallest Δm (i.e. nearest the diagonal) is predominantly due to presence of hard ISR jets. Away from the diagonal, ISR jets are still important, instead to boost the soft SUSY decay system. Subsequently, systematics due to ISR variations are observed to be largest nearest the diagonal for all analysis categories, as shown in Figure A.3 and A.9 for the charm and four-body decay models respectively. For both models uncertainties in the range of 18–22% are observed at the smallest Δm , with uncertainties dropping to 10–25% at larger Δm . Due to the overall dependence on ISR, this source of systematic uncertainty is the largest contribution to the total signal systematic for the compressed models considered here.

9.2.3 B tag scale factors

Specifically for FASTSIM signal samples, events are weighted using the recommended method for FULLSIM samples with an additional FULLSIM to FASTSIM correction factor applied. The FULLSIM correction is applied as an event weight dependent on

the generator level content of an event, and is defined as:

$$w = \frac{SF_b \epsilon \times (1 - SF_b \epsilon) \times SF_{c,light} m \times (1 - SF_{c,light} m)}{\epsilon \times (1 - \epsilon) \times m \times (1 - m)}, \quad (9.1)$$

where $\epsilon(p_T, \eta)$ and $m(p_T, \eta)$ are the b tagging efficiency and mistagging rate, respectively. These factors are functions of p_T and η , and are measured in SM MC for both the hadronic and μ +jets regions, in each H_T bin. SF_b and $SF_{c,light}$ are the prescribed scalefactors (Equation 5.1) for b quarks and u/d/c/s quarks, respectively, as prescribed centrally by the BTAG POG [74].

Applying this event weight provides ‘corrected’ MC yields, which then have further FASTSIM to FULLSIM correction factors applied, as recommended by [86]. Systematic variations equal to the errors of these corrections are applied as upwards and downwards variations, and any effects on signal efficiency times acceptance are studied.

As expected, only small changes in acceptance are found in the charm decay model when b tag scale factor variations are applied, as shown in Figure A.4. While not entirely negligible, it is worth noting that systematics are slightly larger for the $n_b = 1$ category (Figure A.4f), however still at a low level with respect to other systematic sources.

The four-body decay model exhibits a similar dependence on the b tag scale factor variations, indicating large changes in efficiency nearer the diagonal in $n_b = 1$ categories. This increase is visible in Figure A.10f at smaller values of Δm , where the final state b quark is likely out of acceptance, and therefore tags originate from mistagged lighter quarks or gluons.

9.2.4 PDF

MonteCarlo generation includes a simulation of the Parton Density Function (PDF) of the incoming partons, described by a ‘PDF set’. Signal samples are produced using the CTEQ6L1 PDF set. The acceptance sensitivity to the PDF set is investigated by comparing results using three other commonly used PDF sets, namely CT10, NNPDF2.1 and MSTW2008. Following PDF4LHC recommendations, the output is combined to determine an ‘envelope’ value combining the three alternative PDF sets and a related systematic uncertainty [87].

The effect on selection efficiency was studied for charm decay model with the central value and upwards and downwards fluctuation plots summarised in Figure A.2. The largest variations are taken as the systematic uncertainty for both signal models, given

their identical initial states.

9.2.5 $\mathcal{H}_T/\mathcal{E}_T$ cleaning cut

The efficiency of the $\mathcal{H}_T/\mathcal{E}_T$ cleaning cut is compared between data and MC with the aim of revealing any potential issues due to MC mismodelling of the variable. Efficiencies are compared in the $\mu+\text{jets}$ control region, using H_T bins ranging from $200 < H_T < 375$ GeV, in both n_{jet} categories, with no requirement on n_b . Efficiencies are summarised in Table 9.5, where efficiency comparisons between data and MC are shown to statistically agree with unity.

Table 9.5 Efficiencies of the $\mathcal{H}_T/\mathcal{E}_T$ requirement cut for the $\mu+\text{jets}$ selection in data ϵ_{data} and MC ϵ_{MC} , as well as the ratio of both. Efficiencies are shown for the two n_{jet} categories and the four lowest H_T bins, with an inclusive requirements are made of n_b .

n_{jet}	H_T (GeV)	ϵ_{MC}	ϵ_{data}	$\epsilon_{\text{MC}}/\epsilon_{\text{data}}$
2–3	200–275	0.95 ± 0.00	0.95 ± 0.01	1.00 ± 0.01
2–3	275–325	0.97 ± 0.01	0.97 ± 0.02	1.00 ± 0.02
2–3	325–375	0.97 ± 0.01	0.97 ± 0.02	1.00 ± 0.02
2–3	375–475	0.98 ± 0.01	0.98 ± 0.03	1.00 ± 0.03
≥ 4	200–275	0.90 ± 0.02	0.92 ± 0.04	0.98 ± 0.04
≥ 4	275–325	0.92 ± 0.01	0.93 ± 0.02	0.99 ± 0.02
≥ 4	325–375	0.92 ± 0.01	0.93 ± 0.04	0.99 ± 0.04
≥ 4	375–475	0.95 ± 0.02	0.95 ± 0.04	1.00 ± 0.04

While the relevant systematic for the $\mathcal{H}_T/\mathcal{E}_T$ requirement is taken from the above method, it is also interesting to study the acceptance of this cut as a function of the mass plane for each decay. Model acceptance to the $\mathcal{H}_T/\mathcal{E}_T$ cut is typically lower in the four-body decay. This is attributed to the softer jet spectrum produced due to the increased number of final state particles sharing the finite energy of the decay system.

9.2.6 Dead ECAL Filter

To assess any potential MC mismodelling issues with the dead ECAL filter, a similar analysis is made as described for the $\mathcal{H}_T/\mathcal{E}_T$ cut in Section 9.2.5. Efficiencies between data and MC are compared for the $\mu+\text{jets}$ selection, with an inclusive requirement on both n_b and H_T . As shown in Table 9.6, the ratio of efficiencies between data and MC for each n_{jet} category agree within statistical errors.

Table 9.6 Efficiencies of the dead ECAL filter for the $\mu + \text{jets}$ selection in data ϵ_{data} and MC ϵ_{MC} , as well as the ratio of both. Efficiencies are shown for the two n_{jet} categories and the four lowest H_T bins, with an inclusive requirement made of n_b .

n_{jet}	H_T (GeV)	ϵ_{MC}	ϵ_{data}	$\epsilon_{\text{MC}}/\epsilon_{\text{data}}$
2–3	> 200	0.64 ± 0.01	0.64 ± 0.01	1.00 ± 0.01
≥ 4	> 200	0.58 ± 0.01	0.59 ± 0.01	0.98 ± 0.01

Similarly to the study of the $\cancel{H}_T/\cancel{E}_T$ requirement, an inspection of the acceptance of the dead ECAL filter in each scan plane indicates similar values for both models, understood due to the similar jet content of both models. Lower acceptances are found in the $n_{\text{jet}} \geq 4$ category than in the $2 \leq n_{\text{jet}} \leq 3$ category, as the higher number of jets increases the probability for an energy deposit to be near a flagged region of the calorimeter system, thereby increasing the chance of rejection.

9.2.7 Generator Level Partons

At the MADGRAPH matrix element stage of the MC simulation production, a number of additional Feynman diagrams are simulated to account for associated parton interactions. These additional diagrams can affect event kinematics, including the modelling of processes such as Initial State Radiation (ISR) and Final State Radiation (FSR). Given the dependence on such processes in the compressed regime, an additional sub-sample of the charm decay scan has been produced with up to 3 additional partons, to compare against the up to 2 additional partons of the complete scan. This sample contains two mass points at a stop mass near the region of maximum sensitivity, with mass splittings covering both extremities of the scan ($\Delta m = 10$ GeV, 80 GeV). The relative change in efficiency times acceptance between the two scans is shown in Table 9.7. These values are interpreted as systematic uncertainties on the number of associated partons modelled for such compressed spectra models, and are applied as flat contributions across the scan plan for all models.

9.2.8 Luminosity Measurement

Flat corrections across the scan plane are made to account for the uncertainty of the luminosity measurement, as quoted by the Lumi *POG* at 2.5% [88].

Table 9.7 Relative change in efficiency times acceptance for the 2-parton and 3-parton scans in the signal region, with an inclusive selection on n_b and $H_T > 200$ GeV. The scan points are $m_{\tilde{t}} = 200$ GeV and $m_{\tilde{\chi}^0} = (120, 190)$ GeV in the charm decay model.

Category	Δm (GeV)	
	10	80
(2–3,0)	0.00	0.04
(2–3,1)	0.02	0.04
($\geq 4,0$)	0.04	0.04
($\geq 4,1$)	0.00	0.00

9.2.9 Summary

For each mass point in the scan plane, the total systematic uncertainty is the sum in quadrature of all individual contributions. Representative values are summarised in tables 9.8 and 9.9, with full results shown in figures A.7 and A.13 in the mass plane of the charm and four-body decay models respectively. The distribution of total systematic values seen in these plots has been corrected to account for statistical fluctuations through the use of a smoothing procedure that considers a weighted average for each mass point of the surrounding point values. If this average of the neighbour points is different from the value of the point under test by more than 50% then the point is replaced by the neighbour average. This output of this procedure is carefully examined to ensure no loss of total systematic trends throughout the mass plane.

Table 9.8 Representative ranges for each contribution to the total systematic uncertainty on the signal efficiency times acceptance for each relevant event category for the charm decay model interpretation.

Category	(2–3,0)		(2–3,1)		($\geq 4,0$)		($\geq 4,1$)		($\geq 2, \geq 0$)		
	Range	Min.	Max.	Min.	Max.	Min.	Max.	Min.	Max.	Min.	Max.
PDF										0.04	0.14
JES										0.02	0.10
ISR	0.11	0.21	0.08	0.21	0.16	0.22	0.14	0.23			
b tag SF	0.01	0.02	0.03	0.07	0.01	0.02	0.02	0.06			
$H_T/\langle E_T \rangle$	0.02	0.02	0.02	0.02	0.02	0.02	0.02	0.02			
Dead ECAL	0.02	0.02	0.02	0.02	0.02	0.02	0.02	0.02			
Total syst	0.15	0.21	0.09	0.22	0.16	0.22	0.15	0.24			

Table 9.9 Representative ranges for each contribution to the total systematic uncertainty on the signal efficiency times acceptance for each relevant event category for the four-body decay model interpretation.

Category	(2–3,0)		(2–3,1)		($\geq 4,0$)		($\geq 4,1$)		($\geq 2,\geq 0$)	
Range	Min.	Max.	Min.	Max.	Min.	Max.	Min.	Max.	Min.	Max.
PDF									0.04	0.14
JES									0.01	0.07
ISR	0.15	0.20	0.14	0.21	0.17	0.21	0.16	0.23		
b tag SF	0.01	0.02	0.02	0.07	0.01	0.03	0.00	0.06		
$\cancel{H}_T/\cancel{E}_T$	0.02	0.02	0.02	0.02	0.02	0.02	0.02	0.02		
Dead ECAL	0.02	0.02	0.02	0.02	0.02	0.02	0.02	0.02		
Total syst	0.15	0.20	0.15	0.22	0.17	0.22	0.16	0.24		

9.3 Limits on models of Supersymmetry

9.3.1 Overview of limit setting procedure

Signal models are tested for compatibility with observations using a modified frequentist method, namely ‘CLs’ [89]. A test statistic, used to rank experiments from least to most signal-like, is defined as:

$$q_\mu = \begin{cases} -2\log\lambda(\mu), & \text{if } \mu \geq \hat{\mu} \\ 0., & \text{otherwise} \end{cases}, \quad (9.2)$$

where:

$$\lambda(\mu) = \frac{L(\mu, \theta_\mu)}{L(\hat{\mu}, \hat{\theta}_\mu)}, \quad (9.3)$$

μ is the signal strength parameter (equivalent to the variable f defined in Section 8.1, where $\mu = 1$ represents a given signal at its nominal theoretical cross-section), θ_μ is a set of nuisance parameters for a given μ , $\hat{\mu}$ is the Maximum Likelihood (ML) value of μ , and $\hat{\theta}$ is the corresponding ML set of nuisance parameters.

A cartoon example of distributions of some arbitrary version of a test statistic, q_μ , is shown in Figure 9.4. Distributions of q_μ are populated from pseudo-experiments under signal + background and background only hypotheses. For a given observation, 1 minus the quantiles of each distribution are used to determine CL_{s+b} and CL_b , which are used to define:

$$CL_s = \frac{CL_{s+b}}{CL_b}. \quad (9.4)$$

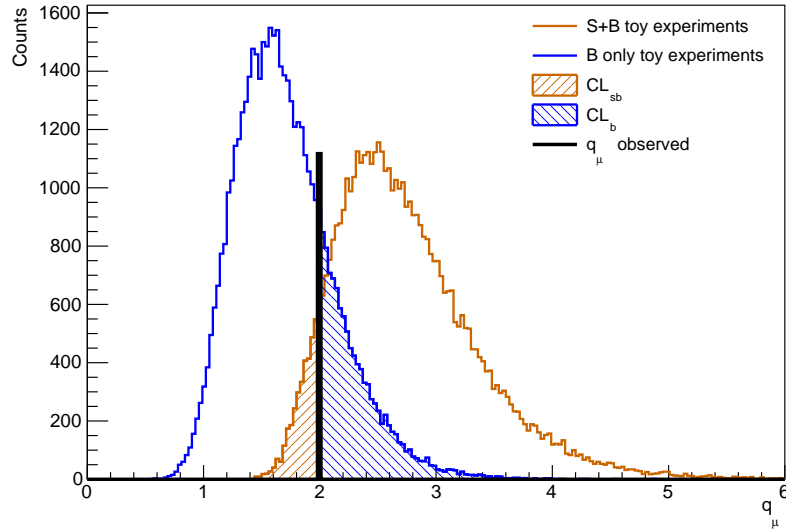


Fig. 9.4 Example distributions of the test statistic, q_μ for Signal+Background (orange) and Background-only (blue) scenarios. The observed value of q_μ is shown in black, with orange and blue quantiles representing CL_{s+b} and CL_b respectively.

A model is considered to be excluded at 95% confidence level if $CL_s \leq 0.05$.

9.3.2 Limits

Limits are calculated per model mass point using 1000 pseudo-experiments generated with the likelihood function using the maximum-likelihood values of the nuisance parameters under the background-only and signal-plus-background hypotheses. Expected limits are determined by considering a scenario where data observations are assumed to be equal to the result of the green-band fits (Section 8.2.1), and observed limits by considering the hadronic data observations. A point is considered excluded if the calculated upper limit cross section is less than the nominal theoretical cross-section (NLO+NLL).

Limits are shown in the $m_{\tilde{t}}$ vs. $m_{\tilde{\chi}^0}$ mass-plane for both the charm (Figure 9.5) and the four-body (Figure 9.6) decay models. Expected limits are drawn as dashed red lines, with $\pm 1\sigma_{\text{experimental}}$ and $\pm 2\sigma_{\text{experimental}}$ uncertainty bands as thin, red dashed lines. The observed limit is drawn as a solid, black line, with $\pm 1\sigma_{\text{theory}}$ uncertainty bands as thin black. The 95% confidence upper limit on the cross section is shown as a colour map as a function of the mass plane.

In comparison to the previous experimental interpretations shown in Figure 2.2.4, the reach in terms of $m_{\tilde{t}}$ is comparable for both models. However, the limits presented here are produced with a single analysis, while maintaining sensitivity across the Δm range relevant to both models - a result which has not yet been accomplished by any other analysis from either experiment. Similarly, previous searches have been highly optimised towards these specific models, whereas the analysis presented in this thesis remains generic to a wide range of potential hadronic SUSY signatures, yet still remains very competitive with these targeted searches.

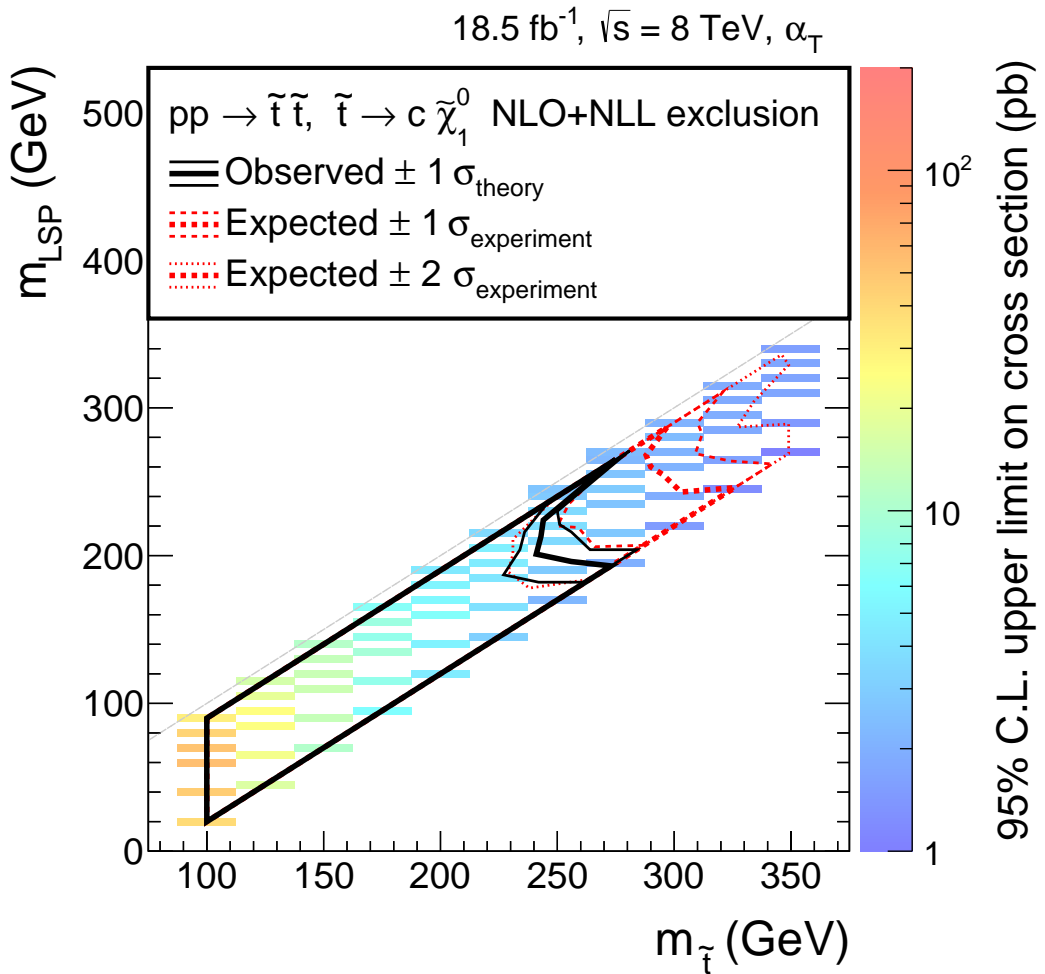


Fig. 9.5 The expected limit (red dashed line) with central band (thick red) and $\pm 1\sigma$ and $\pm 2\sigma$ uncertainty bands (thin red), and the observed limit (thick black) for the charm decay model. The limit is calculated with an inclusive $H_T > 200$ GeV selection, and the analysis categories ($n_b = 0, 2 \leq n_{\text{jet}} \leq 3$), ($n_b = 1, 2 \leq n_{\text{jet}} \leq 3$), ($n_b = 0, n_{\text{jet}} \geq 4$), ($n_b = 1, n_{\text{jet}} \geq 4$).

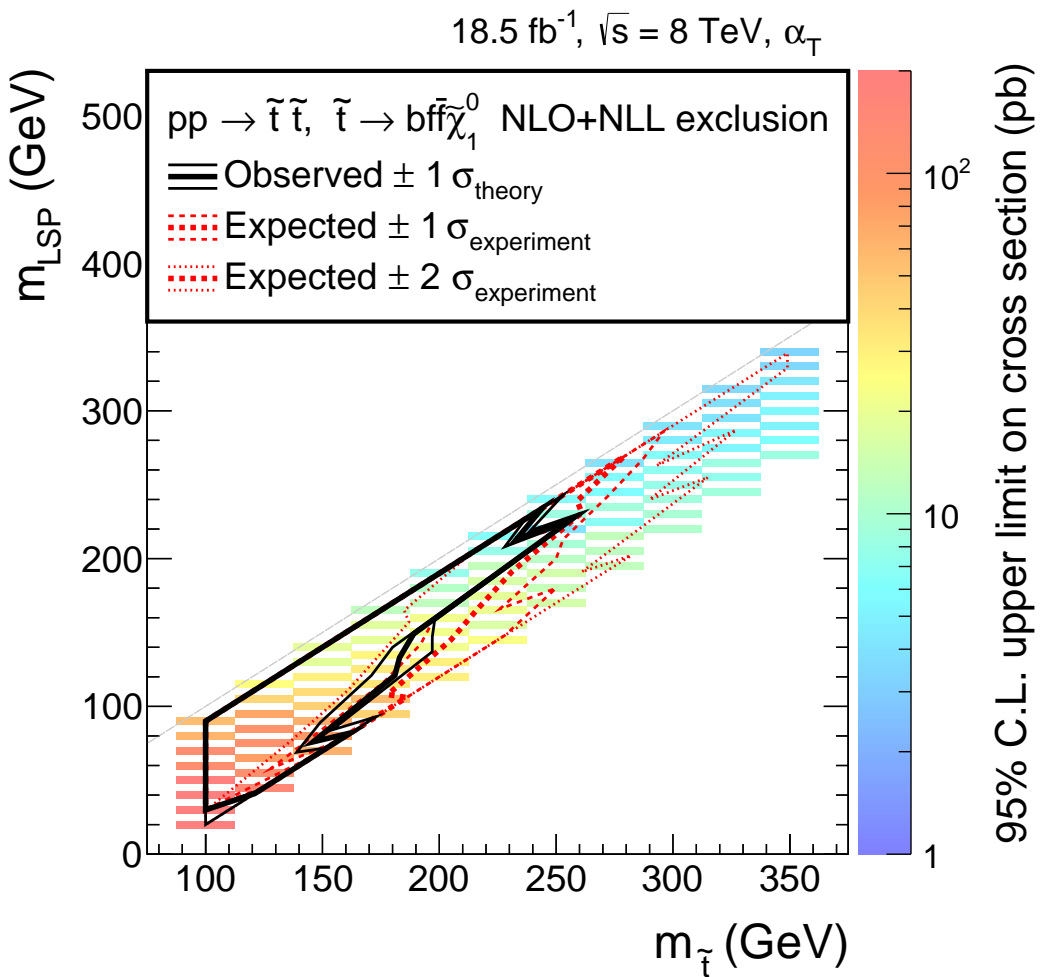


Fig. 9.6 The expected limit (red dashed line) with central band (thick red) and $\pm 1\sigma$ and $\pm 2\sigma$ uncertainty bands (thin red), and the observed limit (thick black) for the four-body decay model. The limit is calculated with an inclusive $H_T > 200$ GeV selection, and the analysis categories ($n_b = 0, 2 \leq n_{jet} \leq 3$), ($n_b = 1, 2 \leq n_{jet} \leq 3$), ($n_b = 0, n_{jet} \geq 4$), ($n_b = 1, n_{jet} \geq 4$).

CHAPTER 10

CONCLUSION

A search for Supersymmetry has been presented based on the full 18.5 fb^{-1} , $\sqrt{s} = 8 \text{ TeV}$ ‘Parked’ dataset from the CMS detector at the LHC. This dataset was collected using experimental, low-threshold triggers to increase sensitivity to soft decays of new physics. The analysis searches for pair-produced gluinos or squarks decaying hadronically to jets and missing transverse energy due to the presence of the weakly-interacting lightest supersymmetric particle (LSP). The search is performed in dimensions of the total transverse hadronic energy, and the multiplicity of jets and b-tagged jets.

Dominant hadronic backgrounds from mismeasured QCD events are reduced by several orders of magnitude to a negligible level using the dimensionless kinematic variable α_T . Following the full signal selection criteria, remaining backgrounds consist of electroweak decays of heavy bosons or top quarks and are predicted using an extrapolation technique from dedicated control regions, orthogonal to the signal region. A total background estimation is determined from a likelihood model fit simultaneously considering both the signal and control regions. Systematic errors on the background prediction are determined using a suite of statistically powerful closure tests designed to probe the many different aspects of the analysis.

Observations in data statistically agree with the results of the background prediction, and as such interpretations have been made with respect to two simplified spectra SUSY models. Given the increased sensitivity of the triggers used, this thesis focuses on compressed models, where the pair-produced sparticles are near-degenerate in mass with the LSP. In this region of phase space two decays of the stop sparticle become dominant: a decay via a charm quark and the LSP, and an off-shell W, bottom quark and the LSP. Limits on the mass of the stop squark with a charm quark decay have been set of up to 275 GeV, with the limit remaining strong across the entire mass-

splitting range - a feature currently unmatched by any other single analysis. Similarly for the four-body decay, stop squark mass limits are set of up to 250 GeV, found to be strongest when the neutralino is near-degenerate in mass with the stop.

While many turned to Run I of the LHC hoping for signs of SUSY, Nature has yet to deliver. Instead the phase space in which SUSY may reside has been greatly reduced. While answering many questions about the possible nature of what lies Beyond the Standard Model, the 8 TeV run also left many open. With the large increase of centre of mass energy to 13 TeV, and a similarly large rise in luminosity, Run II of the LHC will aim to address many of these outstanding questions. Thanks to the Large Hadron Collider we find ourselves in a historically familiar position - we are again standing at the edge of the energy frontier, peering into the unknown. Whatever we see, it's going to be exciting.

APPENDIX A

SIGNAL MODEL SYSTEMATICS PLOTS

Charm decay model

Jet Energy Scale

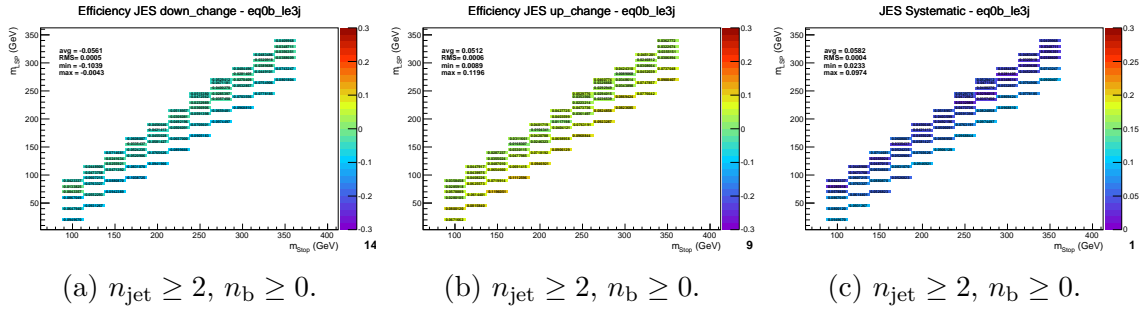


Fig. A.1 The relative change in acceptance times signal efficiency for the charm decay model for downwards (left) and upwards (middle) fluctuations of all jet energies by the uncertainty of the jet energy scale, and the derived systematic values (right). The plots represent a fully inclusive selection - $n_{\text{jet}} \geq 2, n_b \geq 0$ and $H_T > 200 \text{ GeV}.$

PDF

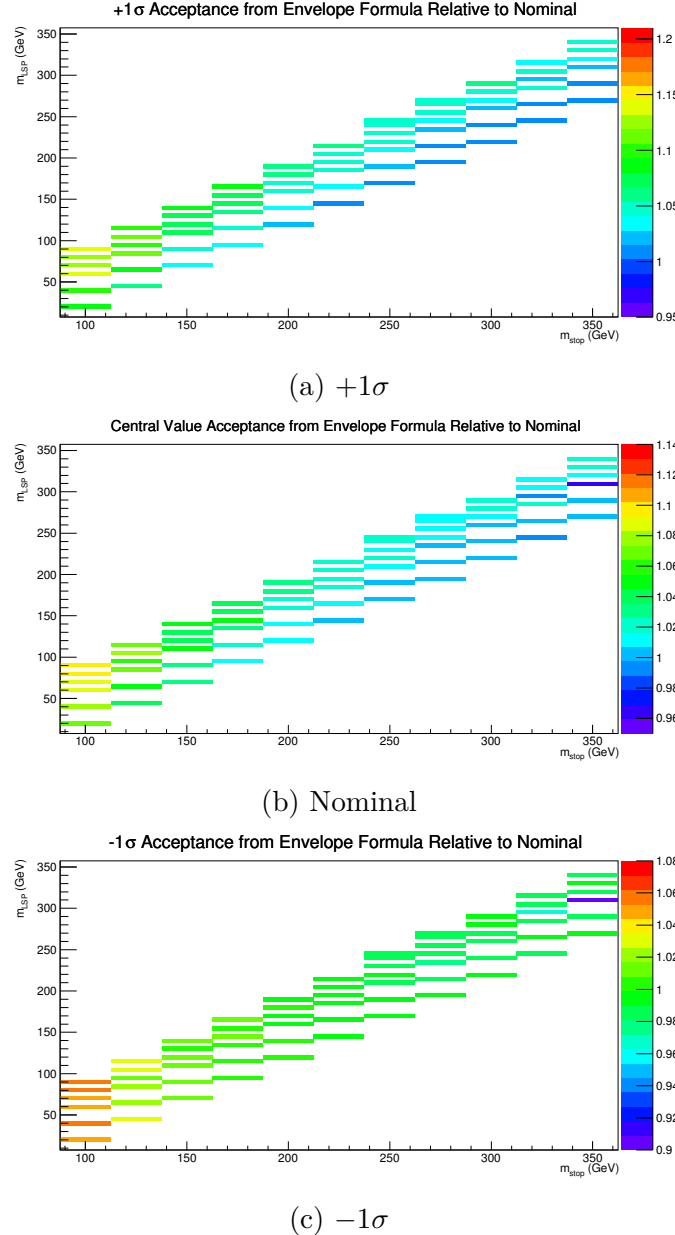


Fig. A.2 PDF uncertainties as a function of the charm decay model scan plane, calculated using a PDF4LHC ‘envelope’ calculation to determine a central band (A.2b), and $\pm 1\sigma$ variations (A.2a and A.2c). Plots are a for a fully inclusive selection on H_T , n_{jet} and n_b .

Initial State Radiation

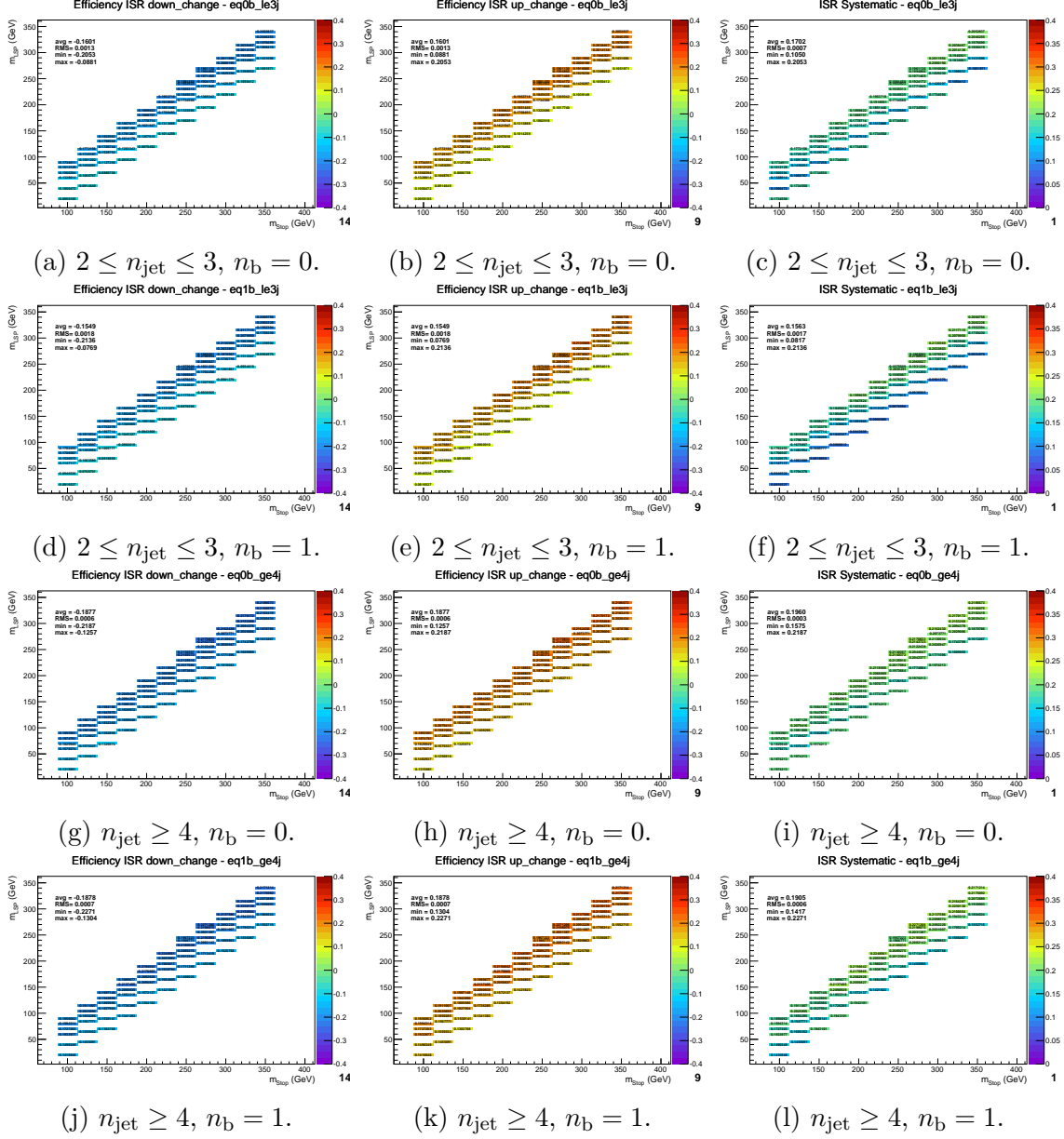


Fig. A.3 The relative change in acceptance times signal efficiency for the charm decay model for downwards (left) and upwards (middle) fluctuations of the global event weight equal to the magnitude of the ISR corrections, and the derived systematic values (right). Each set of plots corresponds to one of the four most sensitive analysis categories (n_b, n_{jet}), with the inclusive requirement $H_T > 200$ GeV.

B-tag Scale Factor

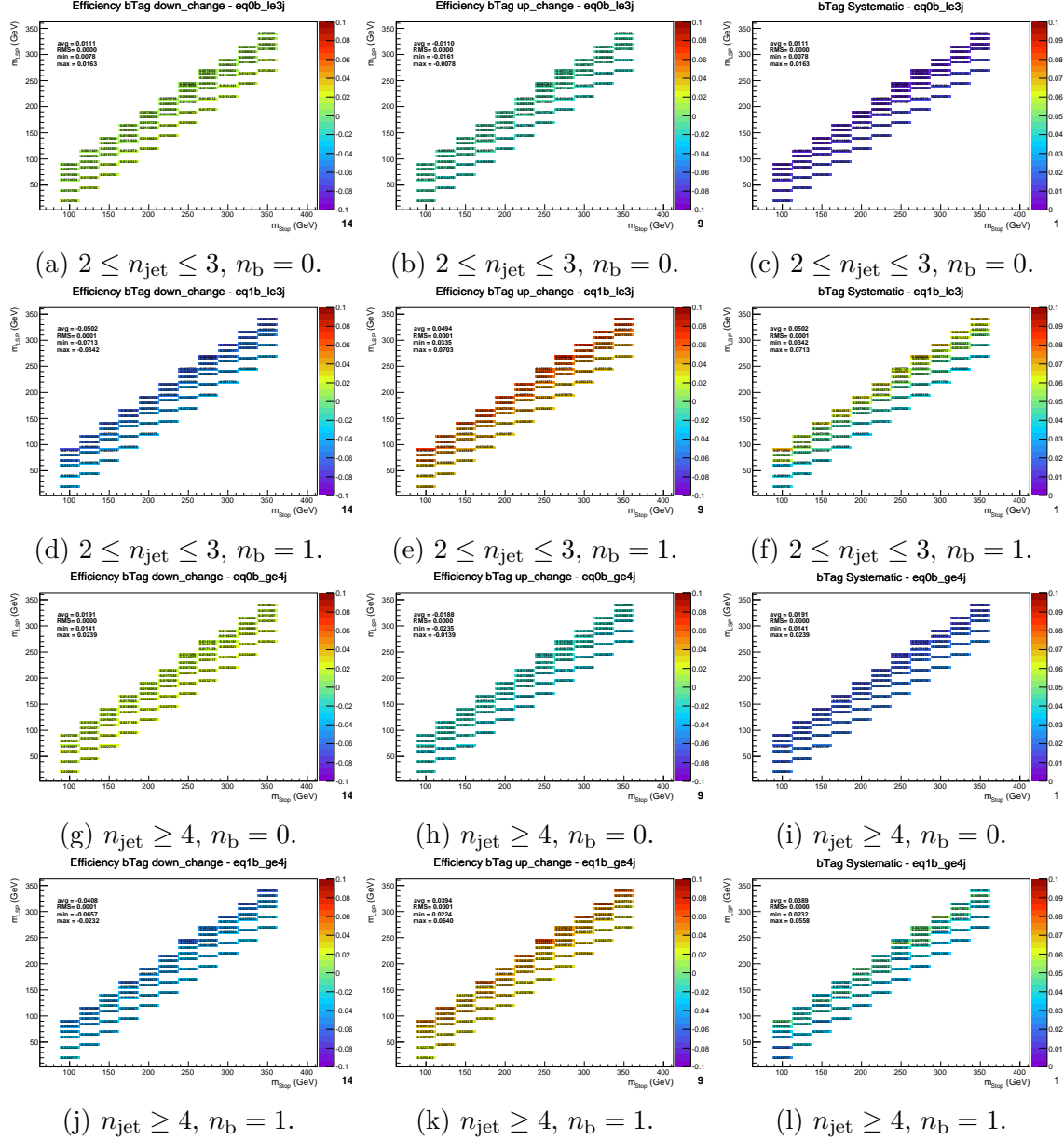


Fig. A.4 The relative change in acceptance times signal efficiency for the charm decay model for downwards (left) and upwards (middle) fluctuations of global event weight according to the uncertainties of the Btag scale factors, and the derived systematic values (right). Each set of plots corresponds to one of the four most sensitive analysis categories (n_b, n_{jet}), with the inclusive requirement $H_T > 200$ GeV.

H_T/\cancel{E}_T cut

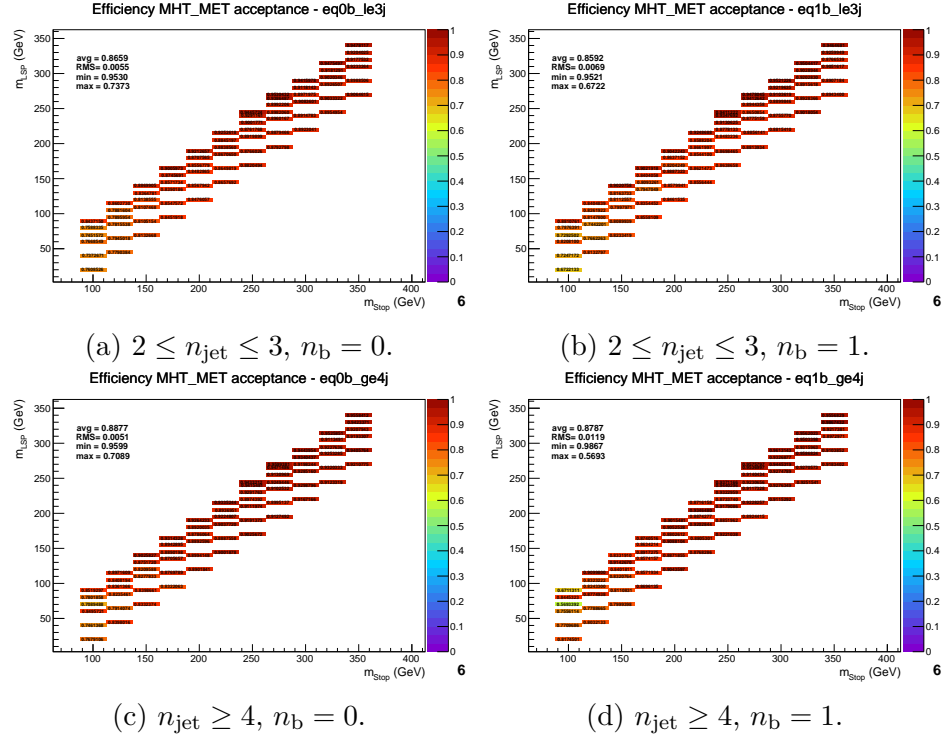


Fig. A.5 The acceptance of the H_T/\cancel{E}_T cut as a function of the charm decay model mass plane. Each plot represents one of the four most sensitive analysis categories (n_b, n_{jet}), with the inclusive requirement $H_T > 200$ GeV.

Dead ECAL cut

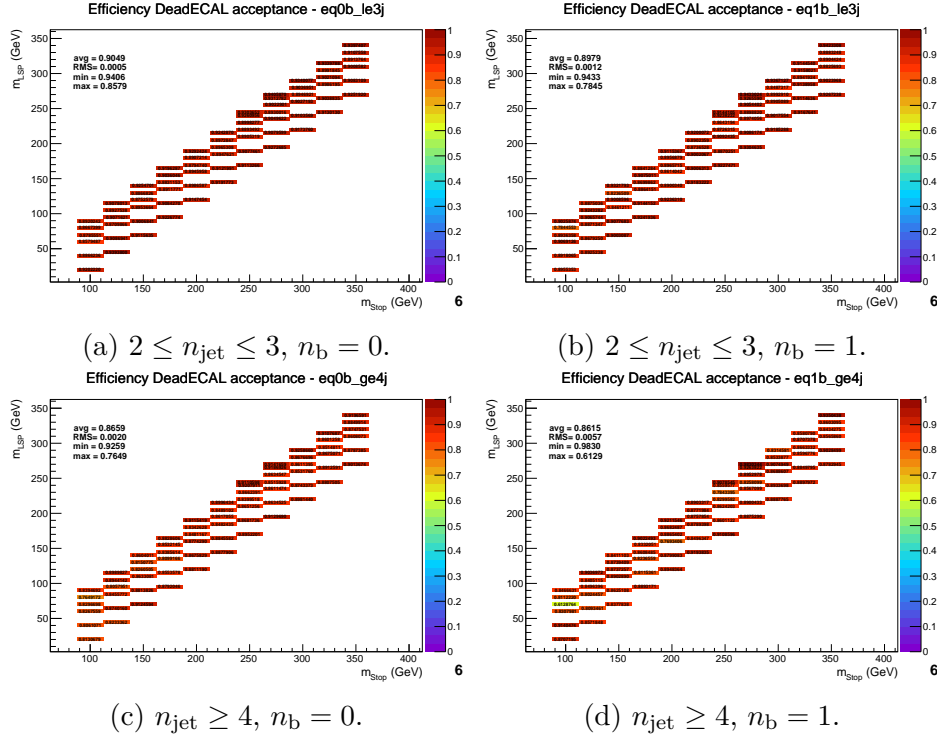


Fig. A.6 The acceptance of the DeadECAL cut as a function of the charm decay model mass plane. Each plot represents one of the four most sensitive analysis categories (n_b , n_{jet}), with the inclusive requirement $H_T > 200$ GeV.

Total systematic error

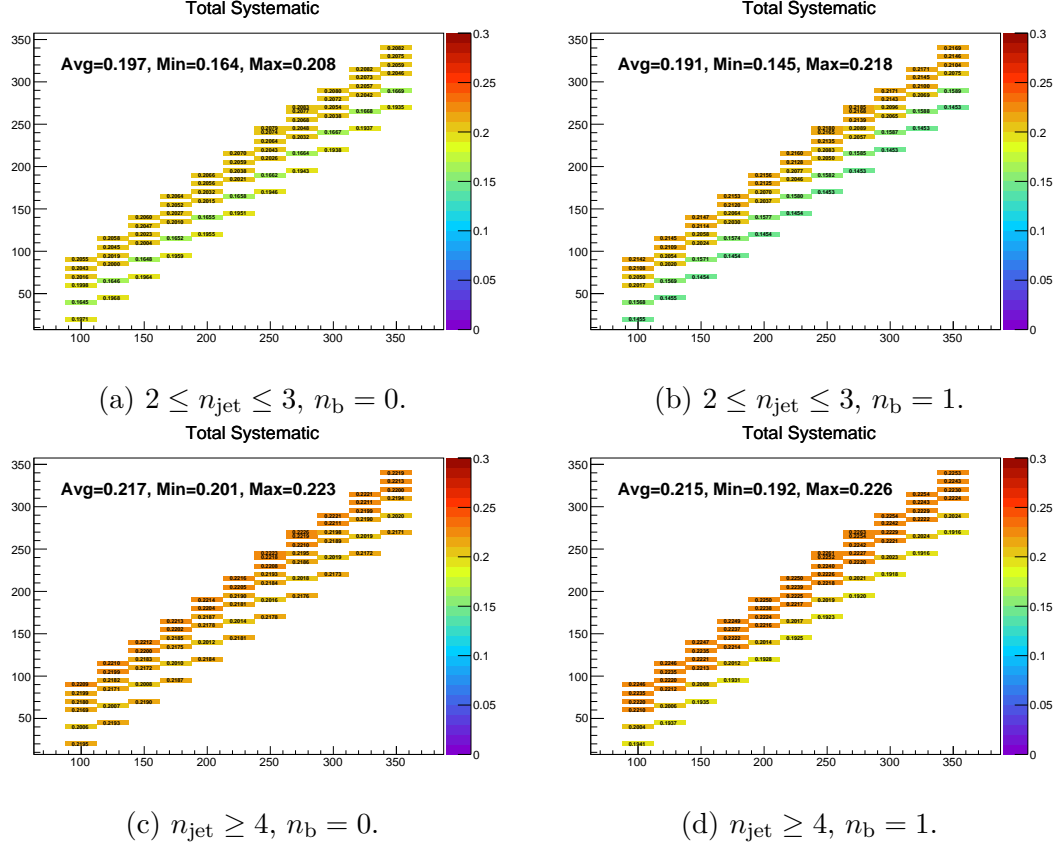


Fig. A.7 The total systematic uncertainty as a function of the charm decay model plane, where all individual systematic contributions are summed in quadrature. Each plot represents one of the four most sensitive analysis categories (n_b, n_{jet}), with the inclusive requirement $H_T > 200$ GeV.

Four-body decay

Jet Energy Scale

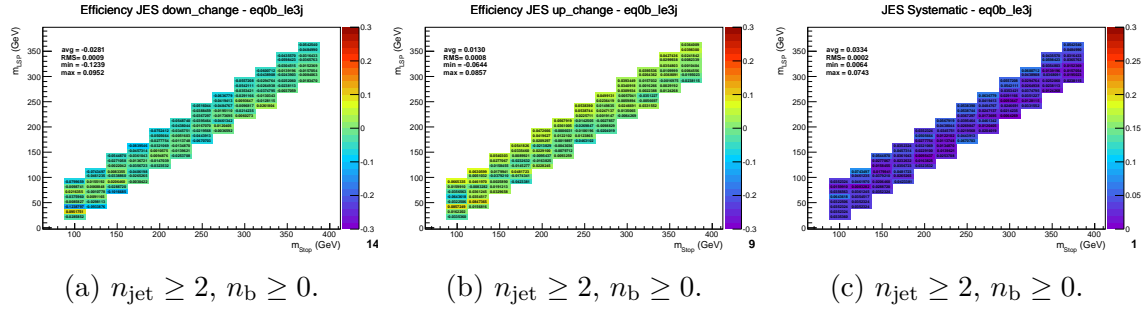
(a) $n_{\text{jet}} \geq 2, n_b \geq 0$.(b) $n_{\text{jet}} \geq 2, n_b \geq 0$.(c) $n_{\text{jet}} \geq 2, n_b \geq 0$.

Fig. A.8 The relative change in acceptance times signal efficiency for the four-body decay model for downwards (left) and upwards (middle) fluctuations of all jet energies by the uncertainty of the jet energy scale, and the derived systematic values (right). The plots represent a fully inclusive selection - $n_{\text{jet}} \geq 2, n_b \geq 0$ and $H_T > 200$ GeV.

Initial State Radiation

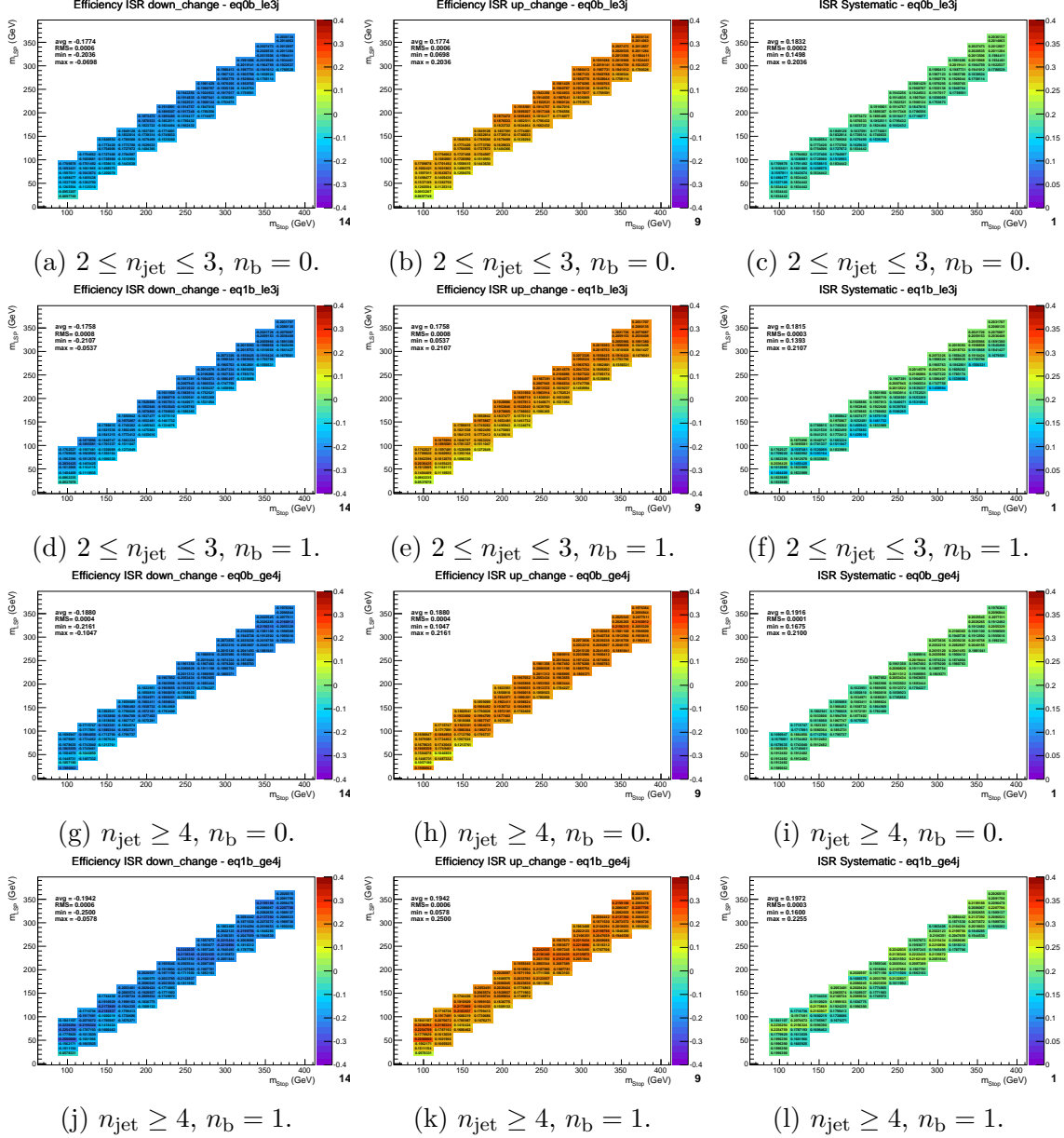


Fig. A.9 The relative change in acceptance times signal efficiency for the four-body decay model for downwards (left) and upwards (middle) fluctuations of the global event weight equal to the magnitude of the ISR corrections, and the derived systematic values (right). Each set of plots corresponds to one of the four most sensitive analysis categories (n_b, n_{jet}), with the inclusive requirement $H_T > 200$ GeV.

B-tag Scale Factor

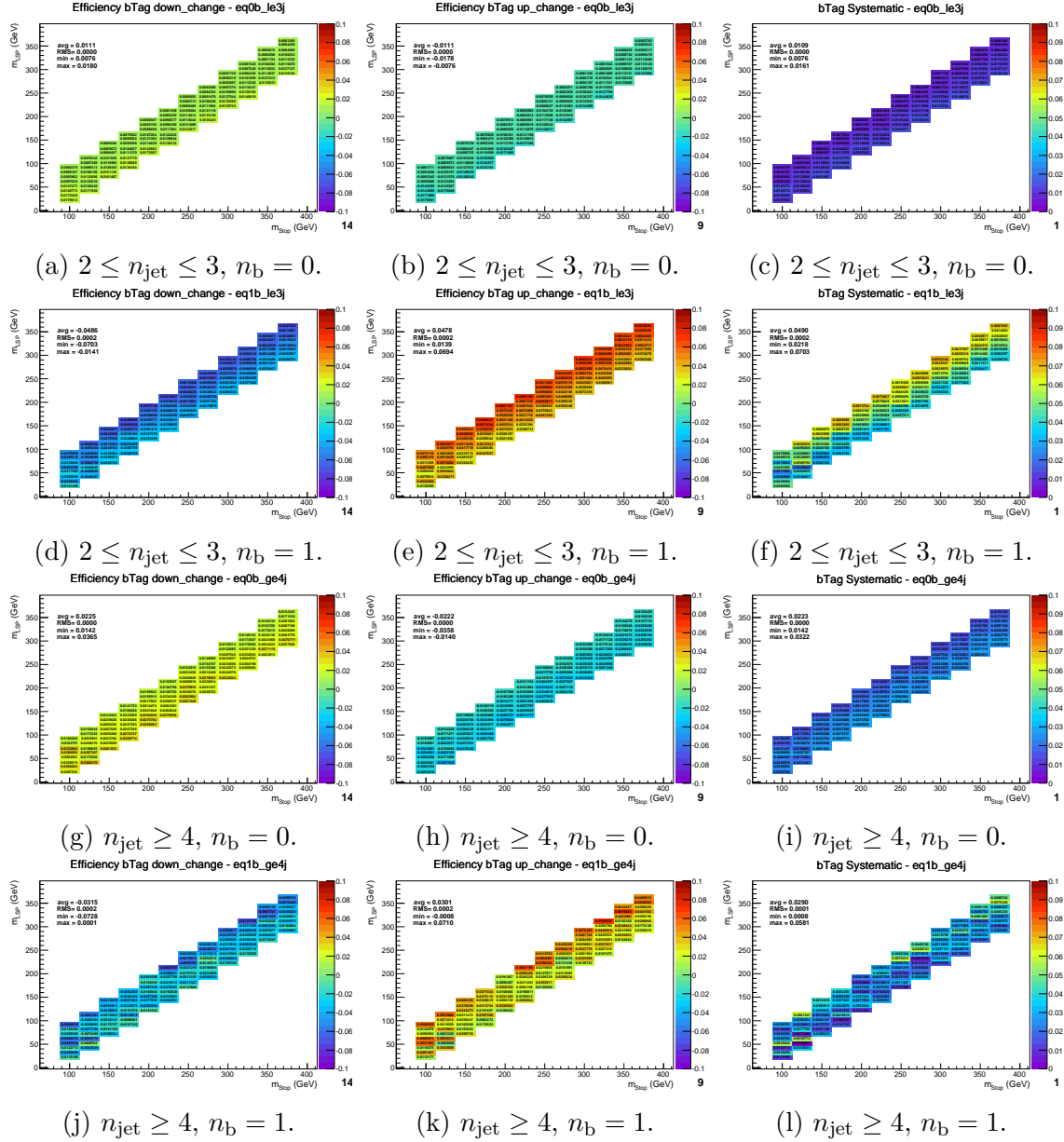


Fig. A.10 The relative change in acceptance times signal efficiency for the four-body decay model for downwards (left) and upwards (middle) fluctuations of global event weight according to the uncertainties of the Btag scale factors, and the derived systematic values (right). Each set of plots corresponds to one of the four most sensitive analysis categories (n_b , n_{jet}), with the inclusive requirement $H_T > 200$ GeV.

H_T/\cancel{E}_T cut

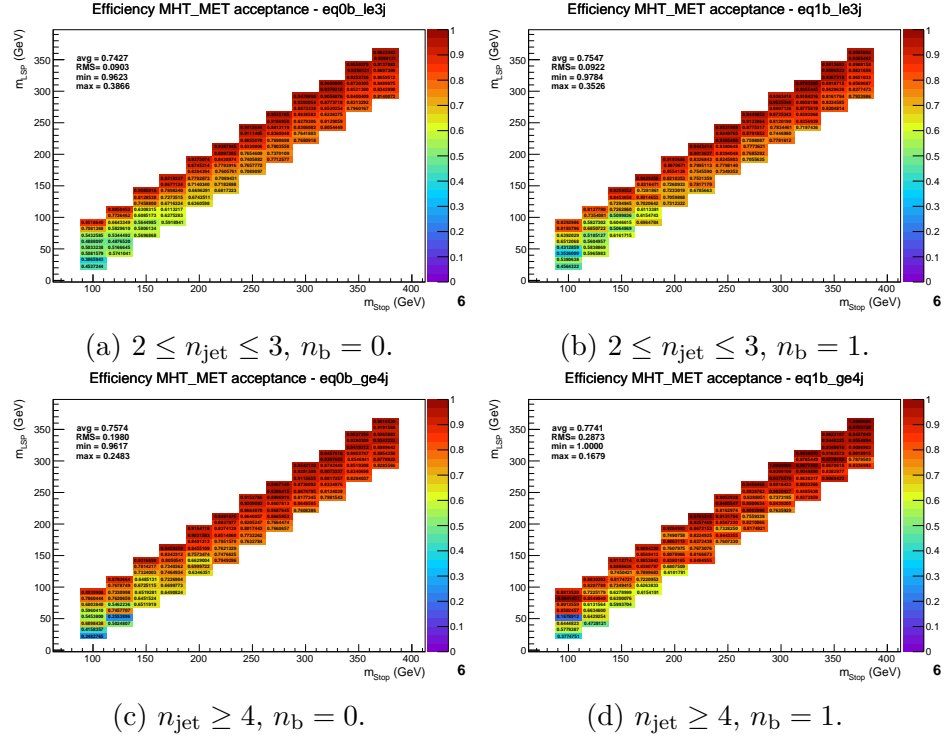


Fig. A.11 The acceptance of the H_T/\cancel{E}_T cut as a function of the four-body decay model mass plane. Each plot represents one of the four most sensitive analysis categories (n_b, n_{jet}), with the inclusive requirement $H_T > 200$ GeV.

Dead ECAL cut

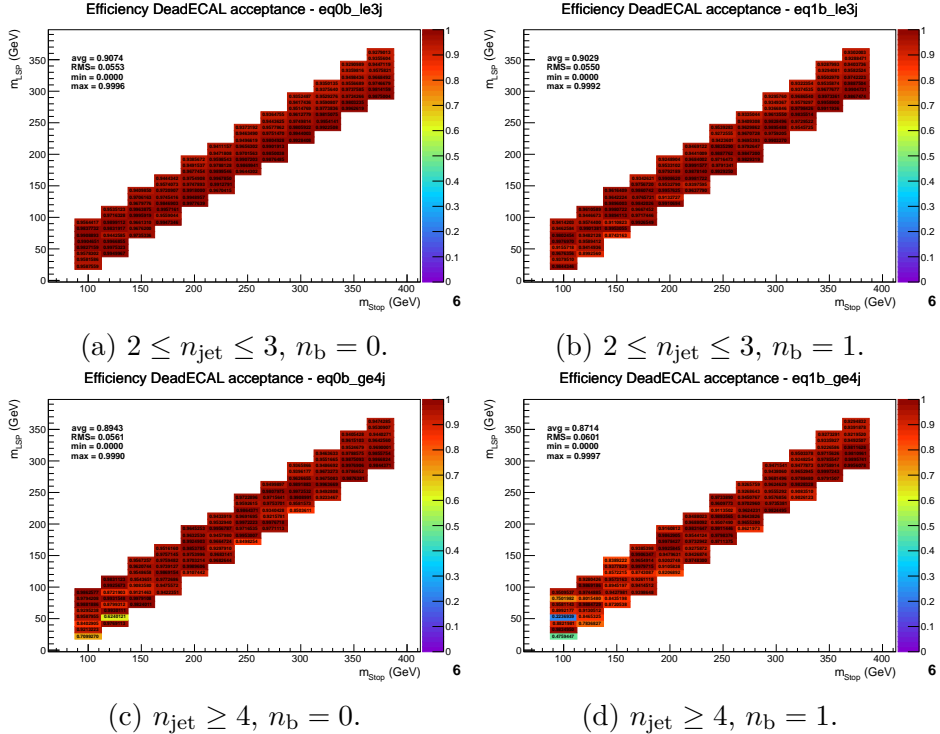


Fig. A.12 The acceptance of the DeadECAL cut as a function of the four-body decay model mass plane. Each plot represents one of the four most sensitive analysis categories (n_b, n_{jet}), with the inclusive requirement $H_T > 200$ GeV.

Total systematic error

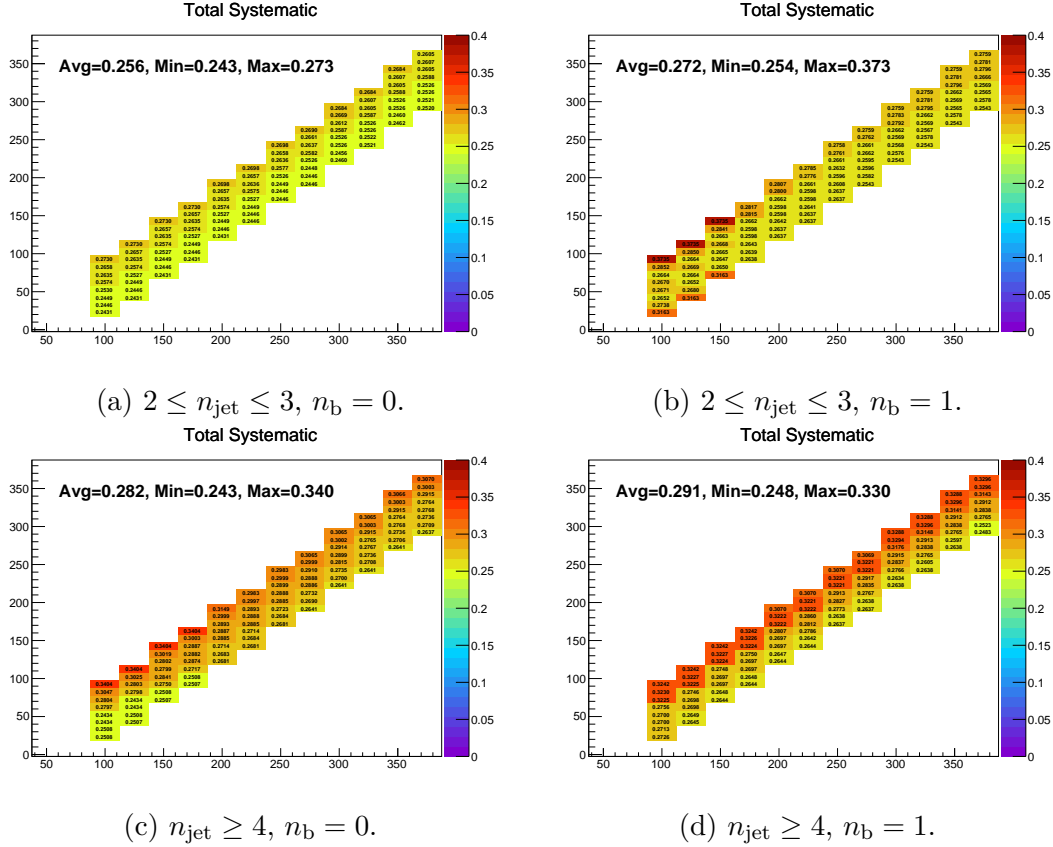


Fig. A.13 The total systematic uncertainty as a function of the four-body decay model mass plane, where all individual systematic contributions are summed in quadrature. Each plot represents one of the four most sensitive analysis categories (n_b, n_{jet}), with the inclusive requirement $H_T > 200$ GeV.

BIBLIOGRAPHY

- [1] ALEPH, CDF, D0, DELPHI, L3, OPAL, SLD, LEP Electroweak Working Group, Tevatron Electroweak Working Group, SLD Electroweak and Heavy Flavour Groups Collaboration, “Precision Electroweak Measurements and Constraints on the Standard Model”, [arXiv:1012.2367](https://arxiv.org/abs/1012.2367).
- [2] S. L. Glashow, “Partial-Symmetries of Weak Interactions”, *Nuclear Physics* **22** (1961), no. 4, 579 – 588,
[doi:`http://dx.doi.org/10.1016/0029-5582\(61\)90469-2`](https://doi.org/10.1016/0029-5582(61)90469-2).
- [3] S. Weinberg, “A Model of Leptons”, *Phys. Rev. Lett.* **19** (Nov, 1967) 1264–1266, [doi:10.1103/PhysRevLett.19.1264](https://doi.org/10.1103/PhysRevLett.19.1264).
- [4] A. Salam, “Weak and Electromagnetic Interactions”, *Conf.Proc. C680519* (1968) 367–377.
- [5] H. D. Politzer, “Reliable Perturbative Results for Strong Interactions?”, *Phys. Rev. Lett.* **30** (Jun, 1973) 1346–1349, [doi:10.1103/PhysRevLett.30.1346](https://doi.org/10.1103/PhysRevLett.30.1346).
- [6] D. J. Gross and F. Wilczek, “Ultraviolet Behavior of Non-Abelian Gauge Theories”, *Phys. Rev. Lett.* **30** (Jun, 1973) 1343–1346,
[doi:10.1103/PhysRevLett.30.1343](https://doi.org/10.1103/PhysRevLett.30.1343).
- [7] B. Martin and G. Shaw, “Particle Physics”. John Wiley and Sons, Ltd., third edition, 2009.
- [8] Particle Data Group Collaboration, “Review of Particle Physics”, *Chin.Phys. C38* (2014) 090001, [doi:10.1088/1674-1137/38/9/090001](https://doi.org/10.1088/1674-1137/38/9/090001).
- [9] F. Englert and R. Brout, “Broken Symmetry and the Mass of Gauge Vector Mesons”, *Phys. Rev. Lett.* **13** (Aug, 1964) 321–323,
[doi:10.1103/PhysRevLett.13.321](https://doi.org/10.1103/PhysRevLett.13.321).

- [10] P. W. Higgs, “Broken Symmetries and the Masses of Gauge Bosons”, *Phys. Rev. Lett.* **13** (Oct, 1964) 508–509, doi:10.1103/PhysRevLett.13.508.
- [11] G. S. Guralnik, C. R. Hagen, and T. W. B. Kibble, “Global Conservation Laws and Massless Particles”, *Phys. Rev. Lett.* **13** (Nov, 1964) 585–587, doi:10.1103/PhysRevLett.13.585.
- [12] Gfitter Group Collaboration, “The global electroweak fit at NNLO and prospects for the LHC and ILC”, *Eur.Phys.J.* **C74** (2014) 3046, doi:10.1140/epjc/s10052-014-3046-5, arXiv:1407.3792.
- [13] A. Riotto and M. Trodden, “Recent progress in baryogenesis”, *Ann.Rev.Nucl.Part.Sci.* **49** (1999) 35–75, doi:10.1146/annurev.nucl.49.1.35, arXiv:hep-ph/9901362.
- [14] W.-S. Hou, “Source of CP Violation for the Baryon Asymmetry of the Universe”, *Chin.J.Phys.* **47** (2009) 134, arXiv:0803.1234.
- [15] Y. Fukuda et al., “Evidence for Oscillation of Atmospheric Neutrinos”, *Phys. Rev. Lett.* **81** (Aug, 1998) 1562–1567, doi:10.1103/PhysRevLett.81.1562, arXiv:hep-ex/9807003.
- [16] Q. R. Ahmad et al., “Measurement of Day and Night Neutrino Energy Spectra at SNO and Constraints on Neutrino Mixing Parameters”, *Phys. Rev. Lett.* **89** (Jun, 2002) 011302, doi:10.1103/PhysRevLett.89.011302, arXiv:nucl-ex/0204009.
- [17] G. Altarelli and F. Feruglio, “Theoretical models of neutrino masses and mixings”, *Springer Tracts Mod.Phys.* **190** (2003) 169–207, doi:10.1007/978-3-540-44901-0_6, arXiv:hep-ph/0206077.
- [18] ATLAS Collaboration and CMS Collaboration Collaboration, “Combined Measurement of the Higgs Boson Mass in pp Collisions at $\sqrt{s} = 7$ and 8 TeV with the ATLAS and CMS Experiments”, *Phys. Rev. Lett.* **114** (May, 2015) 191803, doi:10.1103/PhysRevLett.114.191803, arXiv:1503.07589.
- [19] G. Bertone, D. Hooper, and J. Silk, “Particle dark matter: Evidence, candidates and constraints”, *Phys.Rept.* **405** (2005) 279–390, doi:10.1016/j.physrep.2004.08.031, arXiv:hep-ph/0404175.

- [20] D. Clowe et al., “A direct empirical proof of the existence of dark matter”, *Astrophys.J.* **648** (2006) L109–L113, doi:10.1086/508162, arXiv:astro-ph/0608407.
- [21] Y. A. Gol’fand and E. P. Likhtman, “Extension of the Algebra of Poincaré Group Generators and Violation of p Invariance”, *JETP Lett.* **13** (1971) 323.
- [22] J. Wess and B. Zumino, “Supergauge transformations in four dimensions”, *Nucl. Phys. B* **70** (1974) 39, doi:10.1016/0550-3213(74)90355-1.
- [23] H. P. Nilles, “Supersymmetry, Supergravity and Particle Physics”, *Phys. Reports* **110** (1984) 1, doi:10.1016/0370-1573(84)90008-5.
- [24] H. Haber and G. Kane, “The Search for Supersymmetry: Probing Physics Beyond the Standard Model”, *Phys. Reports* **117** (1987) 75, doi:10.1016/0370-1573(85)90051-1.
- [25] R. Barbieri, S. Ferrara, and C. A. Savoy, “Gauge Models with Spontaneously Broken Local Supersymmetry”, *Phys. Lett. B* **119** (1982) 343, doi:10.1016/0370-2693(82)90685-2.
- [26] S. Dawson, E. Eichten, and C. Quigg, “Search for Supersymmetric Particles in Hadron - Hadron Collisions”, *Phys. Rev. D* **31** (1985) 1581, doi:10.1103/PhysRevD.31.1581.
- [27] S. P. Martin, “A Supersymmetry primer”, *Adv.Ser.Direct.High Energy Phys.* **21** (2010) 1–153, doi:10.1142/9789814307505_0001, arXiv:hep-ph/9709356.
- [28] S. Dimopoulos and D. W. Sutter, “The Supersymmetric flavor problem”, *Nucl.Phys.* **B452** (1995) 496–512, doi:10.1016/0550-3213(95)00421-N, arXiv:hep-ph/9504415.
- [29] E. Witten, “Dynamical Breaking of Supersymmetry”, *Nucl. Phys. B* **188** (1981) 513, doi:10.1016/0550-3213(81)90006-7.
- [30] S. Dimopoulos and H. Georgi, “Softly Broken Supersymmetry and SU(5)”, *Nucl. Phys. B* **193** (1981) 150, doi:10.1016/0550-3213(81)90522-8.
- [31] G. R. Farrar and P. Fayet, “Phenomenology of the production, decay, and detection of new hadronic states associated with supersymmetry”, *Physics*

- Letters B* **76** (1978), no. 5, 575 – 579,
`doi:http://dx.doi.org/10.1016/0370-2693\(78\)90858-4`.
- [32] G. Jungman, M. Kamionkowski, and K. Griest, “Supersymmetric dark matter”, *Phys.Rept.* **267** (1996) 195–373, `doi:10.1016/0370-1573\(95\)00058-5`, [arXiv:hep-ph/9506380](https://arxiv.org/abs/hep-ph/9506380).
- [33] R. Barbieri and D. Pappadopulo, “S-particles at their naturalness limits”, *JHEP* **10** (2009) 061, `doi:10.1088/1126-6708/2009/10/061`, [arXiv:0906.4546](https://arxiv.org/abs/0906.4546).
- [34] M. Carena, G. Nardini, M. Quiros, and C. E. Wagner, “The Effective Theory of the Light Stop Scenario”, *JHEP* **0810** (2008) 062, `doi:10.1088/1126-6708/2008/10/062`, [arXiv:0806.4297](https://arxiv.org/abs/0806.4297).
- [35] M. Papucci, J. T. Ruderman, and A. Weiler, “Natural SUSY Endures”, *JHEP* **1209** (2012) 035, `doi:10.1007/JHEP09\(2012\)035`, [arXiv:1110.6926](https://arxiv.org/abs/1110.6926).
- [36] G. L. Kane, C. F. Kolda, L. Roszkowski, and J. D. Wells, “Study of constrained minimal supersymmetry”, *Phys.Rev.* **D49** (1994) 6173–6210, `doi:10.1103/PhysRevD.49.6173`, [arXiv:hep-ph/9312272](https://arxiv.org/abs/hep-ph/9312272).
- [37] J. R. Ellis, K. A. Olive, and Y. Santoso, “Constraining supersymmetry”, *New J.Phys.* **4** (2002) 32, `doi:10.1088/1367-2630/4/1/332`, [arXiv:hep-ph/0202110](https://arxiv.org/abs/hep-ph/0202110).
- [38] J. Alwall, P. C. Schuster, and N. Toro, “Simplified models for a first characterization of new physics at the LHC”, *Phys. Rev. D* **79** (Apr, 2009) 075020, `doi:10.1103/PhysRevD.79.075020`, [arXiv:0810.3921](https://arxiv.org/abs/0810.3921).
- [39] LHC New Physics Working Group Collaboration, “Simplified Models for LHC New Physics Searches”, *J.Phys.* **G39** (2012) 105005, `doi:10.1088/0954-3899/39/10/105005`, [arXiv:1105.2838](https://arxiv.org/abs/1105.2838).
- [40] CMS Collaboration, “Interpretation of searches for supersymmetry with simplified models”, *Phys. Rev. D* **88** (Sep, 2013) 052017, `doi:10.1103/PhysRevD.88.052017`.
- [41] C. Boehm, A. Djouadi, and Y. Mambrini, “Decays of the lightest top squark”, *Phys.Rev.* **D61** (2000) 095006, `doi:10.1103/PhysRevD.61.095006`, [arXiv:hep-ph/9907428](https://arxiv.org/abs/hep-ph/9907428).

- [42] WMAP Collaboration, “First year Wilkinson Microwave Anisotropy Probe (WMAP) observations: Determination of cosmological parameters”, *Astrophys.J.Suppl.* **148** (2003) 175–194, doi:10.1086/377226, arXiv:astro-ph/0302209.
- [43] C. Balazs, M. Carena, and C. Wagner, “Dark matter, light stops and electroweak baryogenesis”, *Phys.Rev.* **D70** (2004) 015007, doi:10.1103/PhysRevD.70.015007, arXiv:hep-ph/0403224.
- [44] S. P. Martin, “Compressed supersymmetry and natural neutralino dark matter from top squark-mediated annihilation to top quarks”, *Phys.Rev.* **D75** (2007) 115005, doi:10.1103/PhysRevD.75.115005, arXiv:hep-ph/0703097.
- [45] <https://twiki.cern.ch/twiki/bin/view/CMSPublic/PhysicsResultsSUS>.
- [46]
<https://twiki.cern.ch/twiki/bin/view/AtlasPublic/SupersymmetryPublicResults>.
- [47] L. Evans and P. Bryant, “LHC Machine”, *JINST* **3** (2008) S08001, doi:10.1088/1748-0221/3/08/S08001.
- [48] CERN. <http://te-epc-lpc.web.cern.ch/te-epc-lpc/machines/lhc/general.stm>. Accessed: 2015-06-10.
- [49] V. Frigo, “LHC structure”, (Jan, 1997). AC Collection. Legacy of AC. Pictures from 1992 to 2002.
- [50] CMS Collaboration, “CMS Luminosity - Public Results”.
<https://twiki.cern.ch/twiki/bin/view/CMSPublic/LumiPublicResults>. Accessed: 2015-06-10.
- [51] CMS Collaboration, “The CMS experiment at the CERN LHC”, *JINST* **3** (2008) S08004, doi:10.1088/1748-0221/3/08/S08004.
- [52] T. Sakuma and T. McCauley, “Detector and Event Visualization with SketchUp at the CMS Experiment”, *J.Phys.Conf.Ser.* **513** (2014) 022032, doi:10.1088/1742-6596/513/2/022032, arXiv:1311.4942.
- [53] CMS Collaboration Collaboration, G. L. Bayatian et al., “CMS Physics: Technical Design Report Volume 1: Detector Performance and Software”. Technical Design Report CMS. CERN, Geneva, 2006.

- [54] CMS Collaboration Collaboration, G. L. Bayatyan et al., “CMS TriDAS project: Technical Design Report, Volume 1: The Trigger Systems”. Technical Design Report CMS. 2002.
- [55] C. Eck et al., “LHC computing Grid: Technical Design Report. Version 1.06 (20 Jun 2005)”. Technical Design Report LCG. CERN, Geneva, 2005.
- [56] M. Cacciari, G. P. Salam, and G. Soyez, “The anti- k_T jet clustering algorithm”, *JHEP* **04** (2008) 063, doi:10.1088/1126-6708/2008/04/063, arXiv:0802.1189.
- [57] CMS Collaboration, “Jet ID”.
<https://twiki.cern.ch/twiki/bin/viewauth/CMS/JetID>. Accessed: 2015-06-01.
- [58] CMS Collaboration, “Jet Energy Scale”.
<https://twiki.cern.ch/twiki/bin/view/CMS/JetEnergyScale>. Accessed: 2015-06-08.
- [59] CMS Collaboration, “Determination of jet energy calibration and transverse momentum resolution in CMS”, *Journal of Instrumentation* **6** (November, 2011) 11002, doi:10.1088/1748-0221/6/11/P11002, arXiv:1107.4277.
- [60] M. Cacciari and G. P. Salam, “Pileup subtraction using jet areas”, *Physics Letters B* **659** (2008) 119 – 126, doi:10.1016/j.physletb.2007.09.077, arXiv:0707.1378.
- [61] M. Cacciari, G. P. Salam, and G. Soyez, “The catchment area of jets”, *Journal of High Energy Physics* **2008** (2008), no. 04, 005, arXiv:0802.1188.
- [62] CMS Collaboration, “Determination of Jet Energy Calibration and Transverse Momentum Resolution in CMS”, *JINST* **6** (2011) P11002, doi:10.1088/1748-0221/6/11/P11002, arXiv:1107.4277.
- [63] CMS Collaboration, “Identification of b-quark jets with the CMS experiment”, *JINST* **8** (2013) P04013, doi:10.1088/1748-0221/8/04/P04013, arXiv:1211.4462.
- [64] CMS Collaboration Collaboration, “Performance of b tagging at $\sqrt{s}=8$ TeV in multijet, ttbar and boosted topology events”, CMS-PAS-BTV-13-001, CERN, Geneva, (2013).

- [65] CMS Collaboration, “Baseline Muon ID”.
<https://twiki.cern.ch/twiki/bin/view/CMSPublic/SWGuideMuonId>. Accessed: 2015-05-17.
- [66] CMS Collaboration, “Photon ID”.
<https://twiki.cern.ch/twiki/bin/view/CMS/PhotonIDAnalysis>. Accessed: 2015-05-17.
- [67] CMS Collaboration, “Electron ID”. <https://twiki.cern.ch/twiki/bin/view/CMSPublic/SWGuideCutBasedElectronID>. Accessed: 2015-05-18.
- [68] “Search for Direct Top Squark Pair Production in the Single Lepton Channel with Transverse Mass at 8 TeV”, (2012). CMS AN-2013/089.
- [69] J. Pumplin et al., “New generation of parton distributions with uncertainties from global QCD analysis”, *JHEP* **07** (2002) 012,
[doi:10.1088/1126-6708/2002/07/012](https://doi.org/10.1088/1126-6708/2002/07/012), [arXiv:hep-ph/0201195](https://arxiv.org/abs/hep-ph/0201195).
- [70] J. Alwall et al., “MadGraph/MadEvent v4: The New Web Generation”, *JHEP* **09** (2007) 028, [doi:10.1088/1126-6708/2007/09/028](https://doi.org/10.1088/1126-6708/2007/09/028), [arXiv:0706.2334](https://arxiv.org/abs/0706.2334).
- [71] S. Alioli, P. Nason, C. Oleari, and E. Re, “A general framework for implementing NLO calculations in shower Monte Carlo programs: the POWHEG BOX”, *JHEP* **06** (2010) 043, [doi:10.1007/JHEP06\(2010\)043](https://doi.org/10.1007/JHEP06(2010)043), [arXiv:1002.2581](https://arxiv.org/abs/1002.2581).
- [72] T. Sjostrand et al., “High-energy physics event generation with PYTHIA 6.1”, *Comput. Phys. Commun.* **135** (2001) 238–259,
[doi:10.1016/S0010-4655\(00\)00236-8](https://doi.org/10.1016/S0010-4655(00)00236-8), [arXiv:hep-ph/0010017](https://arxiv.org/abs/hep-ph/0010017).
- [73] S. Agostinelli et al., “Geant4—a simulation toolkit”, *Nuclear Instruments and Methods in Physics Research Section A: Accelerators, Spectrometers, Detectors and Associated Equipment* **506** (2003), no. 3, 250 – 303,
[doi:\[http://dx.doi.org/10.1016/S0168-9002\\(03\\)01368-8\]\(http://dx.doi.org/10.1016/S0168-9002\(03\)01368-8\)](http://dx.doi.org/10.1016/S0168-9002(03)01368-8).
- [74]
<https://twiki.cern.ch/twiki/bin/viewauth/CMS/BtagRecommendation53XReReco>.
- [75] A. Giammanco, “The Fast Simulation of the CMS Experiment”, *Journal of Physics: Conference Series* **513** (2014), no. 2, 022012.

- [76] R. Bainbridge, S. A. Koay, “DY+jets at 8TeV: comparison of HT and Njet binned samples”. <https://indico.cern.ch/event/271369/>.
- [77] A. Agapitos et al., “Search for supersymmetry in final states with missing transverse energy and 0, 1, 2, 3, or ≥ 4 b-quark jets in 8 TeV pp collisions using the variable α_T ”, (2012). CMS AN-2012/356.
- [78] L. Randall and D. Tucker-Smith, “Dijet Searches for Supersymmetry at the LHC”, *Phys.Rev.Lett.* **101** (2008) 221803, [doi:10.1103/PhysRevLett.101.221803](https://doi.org/10.1103/PhysRevLett.101.221803), [arXiv:0806.1049](https://arxiv.org/abs/0806.1049).
- [79] CMS Collaboration Collaboration, “SUSY searches with dijet events”, CMS-PAS-SUS-08-005, CERN, 2008. Geneva, (Oct, 2008).
- [80] CMS Collaboration, “Search strategy for exclusive multi-jet events from supersymmetry at CMS”, CMS-PAS-SUS-09-001, CERN, 2009. Geneva, (Jul, 2009).
- [81] R. Cousins, “Probability Density Functions for Positive Nuisance Parameters”. http://www.physics.ucla.edu/~cousins/stats/cousins_lognormal_prior.pdf. Accessed: 2015-02-01.
- [82] W. Verkerke and D. Kirkby, “RooFit”. <http://root.cern.ch/drupal/content/roofit>. Accessed: 2015-02-20.
- [83] F. James and M. Roos, “Minuit: A System for Function Minimization and Analysis of the Parameter Errors and Correlations”, *Comput.Phys.Commun.* **10** (1975) 343–367, [doi:10.1016/0010-4655\(75\)90039-9](https://doi.org/10.1016/0010-4655(75)90039-9).
- [84] G. D. Cowan, “Statistical data analysis”. Oxford University Press, Oxford, 1998.
- [85] D. Olivito, F. Wurthwein et al., “Hadronic Recoil Studies of Heavy Boosted Systems”, (2012). CMS AN-2013/059.
- [86] <https://twiki.cern.ch/twiki/bin/viewauth/CMS/BtagPOG>.
- [87] M. Botje, J. Butterworth, A. Cooper-Sarkar et al., “The PDF4LHC Working Group Interim Recommendations”, (2011). [arXiv:1101.0538](https://arxiv.org/abs/1101.0538).
- [88] CMS Collaboration, “CMS Luminosity Based on Pixel Cluster Counting - Summer 2013 Update”,.

- [89] A. L. Read, “Presentation of search results: the CL s technique”, *Journal of Physics G: Nuclear and Particle Physics* **28** (2002), no. 10, 2693.

